CONTINUOUS GPS MONITORING OF CRUSTAL DEFORMATION WITH THE WESTERN CANADA DEFORMATION ARRAY: 1992-1995

XIN CHEN

April 1998



TECHNICAL REPORT
NO. 195

PREFACE

In order to make our extensive series of technical reports more readily available, we have scanned the old master copies and produced electronic versions in Portable Document Format. The quality of the images varies depending on the quality of the originals. The images have not been converted to searchable text.

CONTINUOUS GPS MONITORING OF CRUSTAL DEFORMATION WITH THE WESTERN CANADA DEFORMATION ARRAY: 1992-1995

Xin Chen

Department of Geodesy and Geomatics Engineering
University of New Brunswick
P.O. Box 4400
Fredericton, N.B.
Canada
E3B 5A3

April 1998

© Xin Chen, 1997

PREFACE

This technical report is a reproduction of a thesis submitted in partial fulfillment of the requirements for the degree of Master of Science in Engineering in the Department of Geodesy and Geomatics Engineering, December 1997. The research was supervised by Dr. Richard B. Langley, and it was supported by the Geological Survey of Canada, by the Natural Sciences and Engineering Research Council of Canada, and by the University of New Brunswick.

As with any copyrighted material, permission to reprint or quote extensively from this report must be received from the author. The citation to this work should appear as follows:

Chen, Xin (1998). *Continuous GPS Monitoring of Crustal Deformation with the Western Canada Deformation Array: 1992-1995*. M.Sc.E. thesis, Department of Geodesy and Geomatics Engineering Technical Report No. 195, University of New Brunswick, Fredericton, New Brunswick, Canada, 158 pp.

Abstract

The objective of this thesis is to conduct research on high-precision, continuous GPS monitoring of the crustal deformation in the northern Cascadia subduction zone, which is located in southwestern British Columbia and known to be one of the most seismically active regions in North America.

Although conventional geodetic measurements were made in the past showing a consistent deformation pattern in the region, these measurements have relatively large uncertainties. In contrast, GPS, as a modern geodetic technique, provides the best means for deformation monitoring: higher accuracy, lower cost, more efficient, and near-real time. The Western Canada Deformation Array (WCDA) is a GPS network designed to monitor the crustal deformation with high precision. It has been in operation since its establishment in the summer of 1992 and is still under development.

The daily data collected from the WCDA stations have been reduced using the CGPS22 software package and the precise orbits generated by Natural Resources Canada (NRCan) or the International GPS Service for Geodynamics (IGS). A specific estimation strategy has been designed and different measurement models have been tested in order to achieve high accuracies. Based on the estimation strategy, 811 days of daily solutions spanning from September 1992 to April 1995 have been obtained and analyzed in particular.

Problems associated with hardware and errors due to scattering effects have been

detected and identified from the results. The scattering effects at stations DRAO, ALBH and WILL caused offsets in the vertical component and the east component of the baselines (latter for ALBH-DRAO only) in the solutions. Meanwhile, the east component of the baseline ALBH-DRAO also suffered an apparent annual variation due possibly to the same scattering effects. All these offsets and variation display a systematic dependence on the choice of elevation cutoff angle.

Small annual variations were found in the north component of most, if not all, of the WCDA baselines and these variations were analyzed with great emphasis. Five tests were carried out in order to identify the source of these annual variations. From the results of these tests, some factors, such as tidal effects and tropospheric mismodelling, can probably be discounted. A test on the GPS satellite antenna offsets reveals a similarity in features between the annual variations and an error caused by an uncalibrated GPS satellite antenna offset along the satellite local x-axis. This leads to a suspicion that a systematic error at a few cm level in the precise orbit/EOP data is the cause of the annual variations, though further efforts are required to verify this claim.

The precision assessment for the WCDA solutions shows long-term repeatabilities of 2 to 5 mm in horizontal components and 6 to 9 mm in vertical components for baseline lengths ranging from 302 to 627 km. Linear rates in each of the baseline components have been estimated by the Least Squares Spectral Analysis algorithm, along with offsets and periodic constituents. In general, these linear rates show a deformation pattern consistent with that obtained from previous conventional measurements. However, a higher resolution on the crustal deformation signals and a better separation of GPS measurement errors from the deformation signals would require a longer set of solutions and more effort on error handling.

Contents

Abstract ii

List of Tables ix

List of Figures xi

Acknowledgements xvi

List of Abbreviations xviii

1 Introduction 1

1.1 Global Positioning System 2

1.2 Role of GPS in Crustal Deformation Study 7

1.3 Contributions of This Thesis 12

1.4 Outline of the Thesis 13

2 Crustal Deformation in the Northern Cascadia Subduction Zone 15

2.1 Tectonic Setting and Earthquake Hazard 16

2.2 Previous Geodetic Measurements and Results 18

2.3 Elastic Dislocation Models of Interseismic Crustal Deformation 21

2.4 Chapter Summary 23

3 Western Canada Deformation Array (WCDA) 25

3.1 Network Configuration 27

3.2 Data Acquisition 32

3.3 The NRCan and IGS Precise Orbits 33

3.4 The WCDA in Summary 36

4 GPS Data Analysis Software Package CGPS22 37

4.1 History of the Software Development 39

4.2 Pre-processing of GPS Data 42

4.2.1 Single Station Pre-processing by A4MAN2 42

4.2.2 Combined Pre-processing by MERGN 43

4.2.3 Cycle Slip Editing 45

4.3 Measurement Models and Algorithms in the CGPS22 Main Processor 47

4.3.1 Carrier Phase Observations 47

4.3.2 Antenna Phase Centre Corrections 50

4.3.3 Relativistic Effect 51

4.3.4 Solid Earth Tides Displacement 51

4.3.5 Ocean Tide Loading Displacement 55

4.3.6 Pole Tide Displacement 56

4.3.7 Tropospheric Delay 59

4.3.8 Stochastic Modelling of Tropospheric Parameters 62

4.3.9 Batch Sequential Least Squares Adjustment 69

4.3.10 Measurement Weighting Scheme 72

4.4 Main-processing of GPS Data 73

4.5 Control and Auxiliary Software 75

4.6 Chapter Summary 76

5 Estimation Strategy and Error Budget for WCDA Data Analysis 78

5.1 Estimation Strategy 78

5.2 Error Budget 82

5.2.1 Orbital Errors 82

5.2.2 Tropospheric Modelling Error 85

5.2.3 Multipath/Scattering Effects 86

5.2.4 GPS Monument Motions 90

5.2.5 Error in the Reference Station Coordinates 92

5.2.6 Other Error Sources 92

5.3 Chapter Summary 94

6 The WCDA Solutions and Analysis 95

6.1 The WCDA Solutions 96

6.2 Analysis of the WCDA Solutions 108

6.2.1 Spectral Analysis 109

6.2.2 Elevation Cutoff Angle Tests 111

6.2.3 Analysis of the Small Variations in the North Components . . 120

6.3 Precision Assessment 135

6.4 Crustal Deformation Signals Inferred from the WCDA Solutions . . . 141

6.5 General Remarks 144

7 Conclusions and Recommendations **145**

7.1 Conclusions 146

7.2 Recommendations 149

References **152**

Vita

List of Tables

3.1 Particulars of GPS tracking stations of the WCDA network. 30

3.2 Antenna setup during 1992-1995 at WCDA tracking stations. 31

4.1 Repeatabilities with and without carrier phase weighting. 73

6.1 The correlation peak values and corresponding time advances in double-differenced daily phase residuals between different days (January 3, 4, 5, and 9, 1994). 99

6.2 The estimated solution offsets. 108

6.3 LSSA results of the WCDA solutions. 110

6.4 LSSA results of the ALBH-DRAO solutions with 30° cutoff angle. . . 114

6.5 The standard deviations for solutions with different tidal models (mm). 127

6.6 Precisions in the north, east, and upward components for the original solutions and the recomputed solutions with correct calibration of the x-axis satellite antenna offset. 128

6.7 Precisions in the north, east, and upward components for solutions using the IGS precise orbits. 129

6.8 The estimated amplitudes and phases of the annual constituent present in the north component of the differenced time series for the WCDA baselines. 132

6.9 The estimated amplitudes and phases of the annual constituent present in the north component of the recomputed WCDA solutions of the year 1994. 132

6.10 Averaged short-term daily repeatabilities (mm). 140

6.11 Averaged long-term daily repeatabilities (mm). 140

6.12 Estimated linear rates from LSSA (mm/yr). 141

6.13 Estimated correlation coefficients R. 142

List of Figures

2.1 Current understanding of the plate tectonic regime of the Cascadia subduction zone. 17

2.2 Patterns of the interseismic and coseismic deformation. 23

3.1 Western Canada Deformation Array up to May 1995. 28

4.1 Flow chart of CGPS22. 38

4.2 Daily solid Earth tide effects at each of the WCDA sites. 52

4.3 Long-term solid Earth tide effects at each of the WCDA sites. 53

4.4 Daily ocean tide loading effects at each of the WCDA sites. 57

4.5 Long-term ocean tide loading effects at each of the WCDA sites. . . . 58

4.6 Long-term pole tide effects at each of the WCDA sites. 60

4.7 Structure functions of random walk, white noise, and colored noise. . 64

4.8 Different simulated stochastic processes (sample interval = 15 minutes). 65

6.1 An example of multipath/scattering effects in the *a posteriori* double-differenced phase residuals. 98

6.2 North component of the baseline ALBH-DRAO. 100

6.3 East component of the baseline ALBH-DRAO. 101

6.4 East component of the baseline ALBH-DRAO (offsets at days 835 and 1107 corrected). 101

6.5 Upward component of the baseline ALBH-DRAO. 101

6.6 Length of the baseline ALBH-DRAO. 102

6.7 Length of the baseline ALBH-DRAO (offsets at days 835 and 1107 corrected). 102

6.8 North component of the baseline HOLB-DRAO. 102

6.9 East component of the baseline HOLB-DRAO. 103

6.10 Upward component of the baseline HOLB-DRAO. 103

6.11 Length of the baseline HOLB-DRAO. 103

6.12 North component of the baseline WILL-DRAO. 104

6.13 East component of the baseline WILL-DRAO. 104

6.14 Upward component of the baseline WILL-DRAO. 104

6.15 Upward component of the baseline WILL-DRAO (offset at day 835 corrected). 105

6.16 Length of the baseline WILL-DRAO. 105

6.17 North component of the baseline UCLU-DRAO. 105

6.18 East component of the baseline UCLU-DRAO. 106

6.19 Upward component of the baseline UCLU-DRAO. 106

6.20 Length of the baseline UCLU-DRAO. 106

6.21 North component of the baseline ALBH-DRAO with 30° cutoff angle. 113

6.22 East component of the baseline ALBH-DRAO with 30° cutoff angle (offsets corrected). 113

6.23 Upward component of the baseline ALBH-DRAO with 30° cutoff angle. 113

6.24 Length component of the baseline ALBH-DRAO with 30° cutoff angle (offsets corrected). 114

6.25 Upward component of the baseline ALBH-DRAO with different cutoff angles. 115

6.26 Upward component of the baseline HOLB-DRAO with different cutoff angles. 116

6.27 Upward component of the baseline WILL-DRAO with different cutoff angles. 117

6.28 North components of the baselines WILL-DRAO, HOLB-DRAO, and UCLU-DRAO. 121

6.29 North component of the baseline WILL-DRAO with a 30-degree cutoff angle. 122

6.30 The errors induced by the uncalibrated x-axis satellite antenna offset for baseline ALBH-DRAO. 130

6.31 The LSSA spectra of the errors in Figure 6.30. 130

6.32 The errors induced by the uncalibrated x-axis satellite antenna offset for baseline WILL-DRAO. 131

6.33 The LSSA spectra of the errors in Figure 6.32. 131

6.34 North component of the error time series caused by the incorrect x-axis satellite antenna offset in the WCDA solutions. 133

6.35 North component of the WCDA baselines after the correct calibration of the x-axis satellite antenna offset. 133

6.36 Short-term daily repeatability of baseline ALBH-DRAO. 136

6.37 Short-term daily repeatability of baseline HOLB-DRAO. 137

6.38 Short-term daily repeatability of baseline WILL-DRAO. 138

6.39 Short-term daily repeatability of baseline UCLU-DRAO. 139

Acknowledgements

My graduate study and research was jointly funded by the Pacific Geoscience Centre (PGC) of the Geological Survey of Canada and the Natural Sciences and Engineering Research Council of Canada (NSERC). Financial assistance to the author has been also provided by the Department of Geodesy and Geomatics Engineering through graduate teaching and research assistantships.

My thanks first go to my supervisor, Professor Richard Langley, for his persistent guidance and support during my graduate study. The first time I "met" Richard was in 1984 when he was giving a lecture on GPS at Wuhan Technical University of Surveying and Mapping and I was then a undergraduate student. Although I did not have a chance to really meet him, his enthusiasm, energy, and knowledge impressed me so much that since then he's been always my first choice for the superviser of my graduate study. Now having worked with him for four years, I sincerely appreciate his advice, patience, trust, and interest in my work. I also feel extremely grateful for his allowing me to twice leave my graduate study for employment without finishing it first.

Second, I would like to thank Dr. Herb Dragert of the Pacific Geoscience Centre. His long-time support ever since May 1992 has given me the great opportunity and

pleasure in working with the WCDA data in the most beautiful working environment in North America, if not the entire world. I love the sunshine and ocean breeze in Victoria, and I truely appreciate Herb's help and trust.

Third, I wish to thank Dr. Jan Kouba of the Geodetic Survey Division, Natural Resources Canada. Jan gave me so much valuable help both personally and professionally during the time I worked with him in Ottawa in 1991 and thereafter. His working spirit and wealth of knowledge have inspired me to persue higher achievements in my career and his kindness deeply touched my heart.

There are many others whom I feel indebted to for all kinds of help. I will just name a few: Yuan Lu for her great assistance in providing her programs to facilitate my daily analysis; Dr. Kelin Wang for his help to make me better understand the crustal deformation of the Cascadia subduction zone through his geophysics perspective; and Mike Schmidt and Gail Jewsbury for their assistance in handling the WCDA data.

Last, but not the least, I wish to thank my parents for their support, encouragement, love, and caring. Without these, my graduate life would have been very different.

List of Abbreviations

AS	Anti-Spoofing
ACP	Active Control Point
ACS	Active Control System
ALBH	Albert Head, Victoria, B.C., Canada
BSLSA	Batch Sequential Least Squares Adjustment
CACS	Canadian Active Control System
DoD	Department of Defense
DRAO	Dominion Radio Astrophysical Observatory, Penticton, B.C., Canada
EMR	Department of Energy, Mines and Resources, Canada
EOP	Earth Orientation Parameters
FLIN	Flin Flon, Manitoba, Canada
GD/GSC	Geophysics Division/GSC
GPS	Global Positioning System
GSC	Geological Survey of Canada
GSD	Geodetic Survey Division, Geomatics Canada, NRCan
IERS	International Earth Rotation Service
IGS	International GPS Service for Geodynamics
ITRF	International Terrestrial Reference Frame

JPL	Jet Propulsion Laboratory
LSSA	Least Squares Spectral Analysis
MACS	Master Active Control Station
NEAH	Neah Bay, Washington, U.S.A.
NANO	Nanoose Harbour, B.C., Canada
NGS	National Geodetic Survey
NRCan	Natural Resources Canada, formerly EMR
O/S	Operating System
PGC	Pacific Geoscience Centre, now GSC Pacific Division, Sidney Subdivision
PPS	Precise Positioning Service
PRN	Pseudo-random Noise
SA	Selective Availability
SPS	Standard Positioning Service
UCLU	Ucluelet, B.C., Canada
UT	Universal Time
UTC	Coordinated Universal Time
VLBI	Very Long Baseline Interferometry
WCDA	Western Canada Deformation Array
WHIT	Whitehorse, Yukon, Canada
WILL	Williams Lake, B.C., Canada

Chapter 1

Introduction

The Global Positioning System (GPS) has become a powerful means for high-precision geodynamic studies since early 1990s when the GPS satellite coverage and a variety of key techniques had been enhanced significantly. Of the key enhancements, the routine production of high-precision orbits by the International GPS Service for Geodynamics (**IGS**) analysis centers, more advanced software algorithms, and more refined error modellings have made the most significant contributions.

Based on these advances, extensive efforts have been made in conjunction with the GPS monitoring of crustal deformation. Many have reported a baseline relative precision of 10^{-8} to 10^{-9} in the literature [e.g., Blewitt, 1993; Lindqwister et al., 1991; Larson and Agnew, 1991; Darby and Meertens, 1995; Savage et al., 1994]. However, these achievements are mostly based on experimental-like data sets, i.e., the data span either a short period such as few weeks or a long period but with sparse samples. There have been few reports, so far as the author knows, of continuous daily GPS monitoring of the crustal deformation on a regional size and at a time scale of a few years.

The Western Canada Deformation Array (WCDA), a network of continuous GPS trackers, has provided an opportunity to conduct such an investigation. The WCDA was established in the northern Cascadia subduction zone and has been operating continuously since September, 1992, in order to study and assess earthquake hazards and tectonic motion associated with the zone.

The objective of this thesis was to carry out a continuous day to day assessment monitoring of the crustal deformation over the period from September 1992 to April 1995 (31 months) on the WCDA with high precision. It is expected that the GPS solutions will benefit the current understandings of the crustal deformation at the northern Cascadia margin and verify the previous geodetic measurements in the region. The process for daily GPS data reduction should be reliable and as automatic as possible. Moreover, the study should also help to detect and identify any potential problems involved with high-precision GPS applications, especially some long-term GPS errors which may only be manifested in a time series sufficiently long and sufficiently dense.

In this chapter, a brief introduction to GPS is presented in section 1.1. Then some characteristics of crustal deformation in a seismic region and the role of GPS in monitoring the crustal deformation are described in section 1.2. The contributions of this thesis and an outline of the thesis are given in section 1.3 and 1.4 respectively.

1.1 Global Positioning System

The Navstar Global Positioning System (**GPS**) is a satellite-based radio navigation system developed by the U.S. Department of Defense (DoD) starting in 1973. It

was initially designed to provide all-weather, worldwide, precise, real-time, three-dimentional positioning, navigation, and timing capability to users, primarily U.S. military personnel. Civilian users unauthorized by DoD are subject to system degradation under the current policy. Since the early 1980s, however, the geodetic community has continuously explored the potential of GPS in geodetic applications and found great use of GPS by developing special techniques.

GPS full operation capability was declared by DoD on July 17, 1995, after the 24 operational satellites (Block II/IIA) had been sent into their assigned orbits and the constellation had been successfully evaluated for operational military functionality. For national security interests of the U.S., there are two modes of intentional limitation to unauthorized GPS users. These are Anti-spoofing (**AS**) and Selective Availability (**SA**). Anti-spoofing guards against fake transmissions of satellite data by encrypting the precision ranging code (P-code) to form the Y-code. Only DoD-authorized users can have the access to the Y-code while the AS is switched on. Selective Availability denies the full system accuracy to unauthorized users by manipulating the broadcast orbit data in navigation message (ϵ technique) and/or by dithering the satellite clock (δ technique). Correspondingly, there are two levels of service: the Standard Positioning Service (**SPS**) and the Precise Positioning Service (**PPS**). SPS is a positioning and timing service which is available to all GPS users on a continuous, worldwide basis. It is designed to provide the capability to obtain horizontal positioning accuracy within 100 m (95% probability), vertical positioning accuracy within 156 m (95% probability), and timing accuracy within 340 nanoseconds (95% probability). PPS provides the full system positioning accuracy of 22 m (95% probability) horizontally and 27.7 m (95% probability) vertically and timing accuracy to UTC within 200 nanoseconds (95 % probability) [Federal Navigation Plan, 1994]. PPS is primarily for U.S. military use and will be denied to unauthorized users

by the use of cryptography. The SA was already activated on July 4, 1991 at the SPS level on Block II satellites (not on Block I satellites). However, the new GPS policy approved on March 29, 1996 by the U.S. president, announced the U.S. Government's intention to terminate SA within the next decade. AS was exercised intermittently through 1993 and implemented permanently on January 31, 1994.

The GPS system consists of three major segments: space segment, control segment and user segment. A brief introduction to each of the segments is given in the following paragraphs.

Space Segment

The fully operational space segment is composed of 21 primary satellites plus 3 active spares with four satellites in each of the six 55 degrees inclined equally-spaced orbit planes at an altitude of about 20,200 km. The orbits are almost circular and have a period of almost exactly 12 sidereal hours, thereby providing a repeated satellite configuration every day about four minutes earlier with respect to the Universal Time (**UT**).

The GPS satellites are often identified by their pseudo-random noise (**PRN**) identifiers, or PRN numbers, and occasionally by the space vehicle numbers, or SV numbers. The PRN number ranges from 1 to 32 and is unique in the GPS constellation at any time. Nonetheless, unlike the SV number, the PRN number is not unique in the history of the GPS constellation. A satellite may use a PRN number previously assigned to an old obsolete satellite.

There are three types of satellites which were or have been in the GPS constellation:

- Block I: development satellites, all out of service now.
- Block II: production satellites, PRN 02, 14, 15, 16, 17, 18, 19, 21 in operation as to October 1, 1997;
- Block IIA: replenishment satellites, PRN 01, 03, 04, 05, 06, 07, 09, 10, 22, 23, 24, 25, 26, 27, 29, 30, 31 in operation as to October 1, 1997.

Each satellite carries highly stable atomic frequency standards on board for maintenance of a precise time base. For instance, all Block II/IIA satellites are equipped with two cesium and two rubidium atomic frequency standards.

The satellites transmit signals on two L-band frequencies: $L_1 = 154 \times 10.23$ MHz $= 1575.42$ MHz and $L_2 = 120 \times 10.23$ MHz $= 1227.60$ MHz. There are three types of PRN ranging codes modulated on the carrier frequencies: the coarse/acquisition (C/A) code, the precision (P) code and the Y-code. The C/A code in addition to its use for the SPS is used primarily to acquire the P-code, while the Y-code is used in place of the P-code whenever the anti-spoofing (AS) mode of operation is activated. The C/A code is available on the L_1 frequency only whereas the P-code is available on both L_1 and L_2. Each satellite transmits a navigation message containing its orbital elements, clock behavior, system time and status messages. In addition, an almanac is also provided which gives the approximate orbit and clock data for each of the active satellites in the constellation. This allows the user set to find all visible satellites quickly once the first has been acquired.

Control Segment

The control segments consists of five monitor stations, five ground antennas, and one Master Control Station (MCS). The monitor stations passively track all satellites

in view and transmit the range data along with the local meterological data via data link to the MCS. By processing these data, the MCS determines satellite orbits and updates each satellite's navigation message. The updated information is transmitted to the ground antennas and uplinked via S-band to the satellites in view.

User Segment

The user segment consists of the users, both military and civilian. The major user equipment is a GPS receiver that contains two components: one antenna and one receiver-processor. Since the late 1970's, the receiver technology has gone through several generations. There are now many types and brands of GPS receivers available in the market. One of the most used receivers by the geodetic community is the Allen Osborne Associates Rogue family, which have been used on all the WCDA tracking sites. Without loss of generality, some of the terminologies and technologies specific to Rogue-type receivers are used in the following descriptions regarding GPS hardware.

The most common observables that a GPS receiver can produce are pseudoranges and carrier phases. Depending on the tracking mode, these observables can be further categorized into: L_1 and L_2 pseudoranges using P-code, L_1 pseudorange using C/A code, $L_1 - L_2$ cross-correlated pseudorange, L_1 and L_2 carrier phases using P-code, L_1 carrier phase using C/A code, and $L_1 - L_2$ cross-correlated carrier phase. In addition, when AS is on, a synthetic L_2 pseudorange which looks like a noiser L_2 P-code pseudorange can be generated by combining the L_1 pseudorange using the C/A code and the $L_1 - L_2$ cross-correlated pseudorange. In a similar manner, a synthetic L_2 carrier phase can be generated.

The pseudoranges are produced indirectly by measuring the satellite PRN code propagation time through space between the satellite and the receiver. The GPS

receiver produces replicas of the C/A and, for dual-frequency receivers, P-code sequences and it measures the phase shift between the received code sequence and its receiver-generated replica at the maximum cross-correlation. This phase shift, given the length and the chipping rate of the code sequence, can be converted to the code propagation time. The C/A code has a wavelength of about 300 m (corresponding to the 1.023 MHz chipping rate), and the P-code 30 m (10.23 MHz chipping rate). The receiver pseudorange resolution varies depending on the type of receiver. The Turbo Rogue receiver, for example, has a pseudorange resolution of 3 to 5 cm for P-code, or about 0.1% of the code wavelength [Chen and Dragert, 1992].

The carrier phases are produced directly by measuring the relative phase between the received carrier signal and the internal reference carrier signal derived from the receiver local oscillator. The wavelengths for the L_1 and L_2 carrier signals are 19.03 cm and 24.42 cm respectively. The resolution for carrier phases are better than the resolution for P-code pseudoranges by 2 orders of magnitude. The Mini Rogue receiver, for example, has shown a resolution of 0.1 to 0.2 mm for carrier phases [Kouba and Chen, 1992]. On the other hand, unlike the pseudoranges, the carrier phases have an initial cycle ambiguity problem because one turn of phase is indistinguishable from another. As a result, these initial cycle ambiguities have to be solved for during the post-processing of the data in order to take full advantages of the carrier phases.

1.2 Role of GPS in Crustal Deformation Study

In a seismic plate boundary region, the crustal deformation is characterised with a cyclic pattern by the development and release of elastic strain due to the relative plate motions. The release of the elastic strain accumulated since last earthquake

triggers the occurrence of a new earthquake and causes abrupt large displacements near the tectonic fault. This period is called the **coseismic** phase of an earthquake cycle. In the second phase of the cycle, or the **interseismic** phase, the strain begins to accumulate again until the next earthquake. Typically the interseismic phase endures for more than 90% of the total earthquake cycle and the ground near the fault moves slowly and very little during the period. According to the elastic rebound model of the earthquake cycle, the ground away from the fault moves at a steady rate and is nearly unaffected during an earthquake [Bock, 1991]. In addition, for some earthquakes, two additional distinct phases may be distinguished. Near the end of the interseismic period, a period of abnormally slow or fast deformation may occur. This is referred to as the **preseismic** phase. The other period is termed as the **postseismic** phase, which immediately follows the coseismic phase and precedes the interseismic phase. During this period, inelastic and viscous effects in regions surrounding the main shock result in postseismic slip on faults in the epicentral region. Because of these different characteristics of the crustal deformation in different phases, the temporal and spatial distribution of the crustal deformation, if precisely monitored, can provide important information for earthquake and tectonic studies.

Conventionally, crustal deformation was monitored by terrestrial geodetic techniques, including tide gauges, levelling, trilateration, and triangulation. Other techniques, such as the tilt meter and strain gauge, were also used, but because of the difficulty in the separation of the true tectonic strain and the local environmental effects, these techniques were not as reliable and not as frequenly used as the geodetic techniques [Lambeck, 1988].

The terrestrial geodetic techniques in all had a very long history in crustal deformation monitoring. Although they have many disadvantages compared to the

modern techniques like GPS, they provided very important measurements and have greatly contributed to the current geodynamic studies. However, with the emergence of high-accuracy extraterrestrial geodetic techniques such as GPS, Very Long Baseline Interferometry (**VLBI**), and Satellite Laser Ranging (**SLR**) in the 1970s, the terrestrial geodetic techniques have become less and less important in crustal deformation monitoring. VLBI and SLR, although extremely expensive and sparsely distributed, have provided the most accurate global reference frame and measurements for tectonic motions. Especially GPS, due to its accuracy, portability, low cost, and tolerance for adverse weather conditions, has been extensively applied for geodynamical studies and has essentially replaced the conventional techniques. GPS data yield higher quality and larger quantity of information than any of the conventional techniques. Three dimensional position vector can be obtained from GPS data, whereas none of the conventional techniques alone is able to provide this information. The conventional techniques may be combined to obtain three dimensional information, but the combination is rarely available and it is still subject to certain limitations.

Depending on a number of factors such as the type of the fault (thrust or strike-slip) and the accessability of the fault, the method and scale of GPS crustal deformation monitoring may vary. In general, the monitoring of crustal deformation by GPS can be implemented on three different scales: local ($\leq$ 100 km), regional ($\leq$ 1000 km) and global ($>$ 1000 km). When a tectonic fault is well accessable on land, the deformation cross the fault can be measured with the best accuracy on both local and regional scales. A combination of all the three scales of monitoring can provide the fullest spatial spectrum of the deformation signal. When a tectonic fault is not easily accessed, as in many cases involved with oceanic plates, the deformation at the fault cannot be measured directly on a local scale. Thus, the deformation in the closest possible vicinity of the fault must be measured relative to a usually remote reference

point or frame that is deemed to be free from the deformation being monitored. Due to the long distances from the monitor stations to the fault, the magnitude of the deformation to be measured on a regional scale is usually small. As a result, a longer period is required to resolve the strain rate with the same precision as compared to that on local scale monitoring and some assumptions must be made to deduce what is really happening in the immediate vicinity of the fault. The global scale monitoring is used to study global plate tectonics. It is realized through international cooperation by, e.g., the IGS analysis centres.

The local and regional scales of GPS monitoring can be carried out in either or both of two ways: repeated GPS campaigns and deployment of a permanent GPS deformation array. The permanent GPS deformation array performs as a control network and produces continuous measurements which are very important in the determination of the instantaneous coseismic displacement and long-term maintenance of a consistent fiducial framework. The repeated GPS campaigns, usually employed for local scale monitoring, are a densification or supplement to the permanent array if one has been deployed. A combination of the two methods can provide the best efficiency and reliability.

Several permanent GPS deformation arrays of different size have been established in seismically or volcanically active regions. The large ones include the Southern California Integrated GPS Network (SCIGN) [Bock et al., 1993], the San Francisco Bay Area Regional Deformation (BARD) network [King et al., 1995], and the Japanese nationwide GPS Regional Array for Precise Surveying (GRAPES) [Miyazaki et al., 1996]. There are also some medium or small sized permanent GPS deformation arrays, such as the Western Canada Deformation Array (WCDA) [Chen, 1994] and the GPS network on the Big Island, Hawaii [Lisowski et al., 1996].

Crustal deformations in interseismic, coseismic, and postseismic phases have been successfully detected using the GPS technique, as reported in the literature. For example, coseismic displacements have been precisely observed using the GPS technique during several recent earthquakes: 1992 Landers earthquake (M7.3) [Blewitt et al., 1993], 1994 Northridge earthquake (M6.7) [Hudnut et al., 1996], 1994 Hokkaido Touhou-oki (Kuril) earthquake (M8.1), 1994 Sanriku Haruka-oki earthquake (M7.5), and 1995 Hyougo-ken Nanbu (Kobe) earthquake (M7.2) [http://www.goin.nasda.go.jp /GOIN/GSI/eng/Crustal_deformaion.html]. Postseismic deformation following the 1992 Landers earthquake, ranging from 55 mm near the epicenter to a few mm far from the fault, was observed and reported by Shen et al. [1994]. The interseismic displacement have been detected from several permanent GPS deformation arrays. For example, Bock et al. [1997] reported the crustal deformation measurements from the southern California Permanent GPS Geodetic Array (PGGA), and Chen [1994] and Dragert and Hyndman [1995] reported the estimated velocities and strain-rates from the WCDA. These measurements have greatly contributed to the refinement of the crustal deformation models in those regions. Were it not for GPS, these kinds of measurements would never be obtained so accurately and efficiently.

In summary, GPS has become a major tool for crustal deformation monitoring. Its applications have already borne fruit and it will more significantly benefit crustal deformation studies in the near future as more precise strain rates resolved from the high precision GPS measurements become available.

1.3 Contributions of This Thesis

In accordance with the goal of the Western Canada Deformation Array for the crustal deformation studies in the northern Cascadia subduction zone, a particular estimation strategy was designed and has yielded a very good outcome. Thirty one months worth of data have been reduced successfully based on an estimation strategy using a newly developed version of the CGPS22 software package. The results in general satisfy the precision requirements expected for crustal deformation study, with several millimetres of horizontal and vertical precisions on baselines ranging in length from 302 to 627 km. Studies have been carried out on the WCDA solutions by using a spectral analysis technique and testing on various factors in order to detect and identify errors that may be present in the solutions. The tested factors included satellite elevation cutoff angle, multipath removal, measurement weighting scheme, tropospheric modelling, tidal effects, satellite antenna offsets, and precise orbits and their representation in polynomial forms. As a result of the analyses, multipath effects have been successfully detected and identified, and small variations have been found in the north component of the WCDA baselines. Although the source of the small variations has not yet been precisely identified through the tests, evidence was found to indicate that the orbital errors in the precise orbits may be responsible for the variations. In addition, software development has been undertaken in two aspects. One is with regard to the forementioned analyses and tests. The other is focused on the automation of the daily WCDA data reduction and the robustness of the algorithms.

Since the research covers a wide range of subjects, it is very difficult and unnecessary to include every detail in this thesis. For the reason, a certain amount of detail

have been purposedly omitted to keep the thesis well organized.

1.4 Outline of the Thesis

Chapter 1 outlines the Global Positioning System and its role in crustal deformation studies and then comments on the contributions made in this research.

Chapter 2 gives an overall review of the crustal deformation studies in the northern Cascadia subduction zone and results from previous geodetic surveys carried out on Vancouver Island.

Chapter 3 first introduces the Western Canada Deformation Array (WCDA) in four aspects: the goal, the configuration, the equipment, and the data acquisition. Then, the precise orbits generated by Natural Resources Canada (NRCan, formerly Energy, Mines and Resources Canada - EMR) and IGS, as an important support and input to the WCDA, are also described.

Chapter 4 descibes the CGPS22 software package employed for the daily WCDA data reduction and analysis, including the history of the software development, the main features, and some new developments. The measurement models in CGPS22 are given in particular as they are the core of the software and critical for the high-precision GPS applications. The practical procedures of data processing are also presented in detail.

Chapter 5 explains the estimation strategy applied to the WCDA data reduction and gives an error budget which evaluates possible contributions of major error sources to the WCDA solutions.

Chapter 6 describes the results of the WCDA daily data reduction and analysis.

The solutions spanning 31 months and some problems encountered in the data reduction are first presented. Secondly, the errors manifested in the solutions are analysed and identified by using a spectral estimation technique and by several tests involved with elevation cutoff angle, tropospheric modelling, tidal effects, precise orbits, etc. Thirdly, the precisions achieved in terms of the short-term and long-term repeatabilities are given. Last, the crustal deformation signals inferred from the WCDA solutions are discussed.

Chapter 7 summarizes this thesis with conclusions drawn from the results and gives some recommendations for future developments.

Chapter 2

Crustal Deformation in the Northern Cascadia Subduction Zone

The northern Cascadia subduction zone, located in southwestern British Columbia, is known to be one of the most seismically active areas in Canada and the northwest Pacific coast of North America. There is strong evidence supporting the claim that major megathrust earthquakes repeatedly occurred throughout history in the region. To help assess the potential major earthquake hazard and study the tectonic mechanism in the region, many geodetic measurements have been conducted in the past, ranging from conventional techniques to the most modern techniques. These measurements, combined with theoretical deformation models, provide the means and foundation for earthquake studies.

In this chapter, the tectonic setting of the northern Cascadia subduction zone

is first presented in section 2.1. Section 2.2 then briefly summarizes the previous geodetic measurements of the crustal deformation in this region. Based on the results of the geodetic measurements and a simple elastic dislocation model, the theoretical inference on present crustal deformation is discussed in section 2.3. Section 2.4 gives a concluding summary for this chapter.

2.1 Tectonic Setting and Earthquake Hazard

The Cascadia subduction zone is located at the margin of the oceanic Juan de Fuca Plate and the continental North America Plate (**Figure 2.1**). It extends from offshore southern Vancouver Island to Oregon State along the west Pacific coast. The distance between the deformation front and the outer coast of southern Vancouver Island is about 100 km. The contemporary plate convergence rate across the Cascadia margin is estimated at about 4.5 cm/yr [Dragert et al., 1994a].

To the north of the Cascadia subduction zone is the Explorer Plate which converges with the continental North America Plate at a rate of about 2 cm/yr in a direction that likely varies as a function of position because of the close proximity of its pole of rotation [Riddihough, 1984]. The boundary between the Juan de Fuca Plate and the Explorer Plate is the Nootka Transform Fault zone and its extension underlies central Vancouver Island [Dragert and Lisowski, 1990].

The primary thrust or detachment surface of subduction zones and most convergent margins are known to have produced the largest earthquakes in the world. Historically, as inferred from extensive paleoseismicity data, major megathrust earthquakes have occurred on the Cascadia margin at irregular intervals ranging from 300

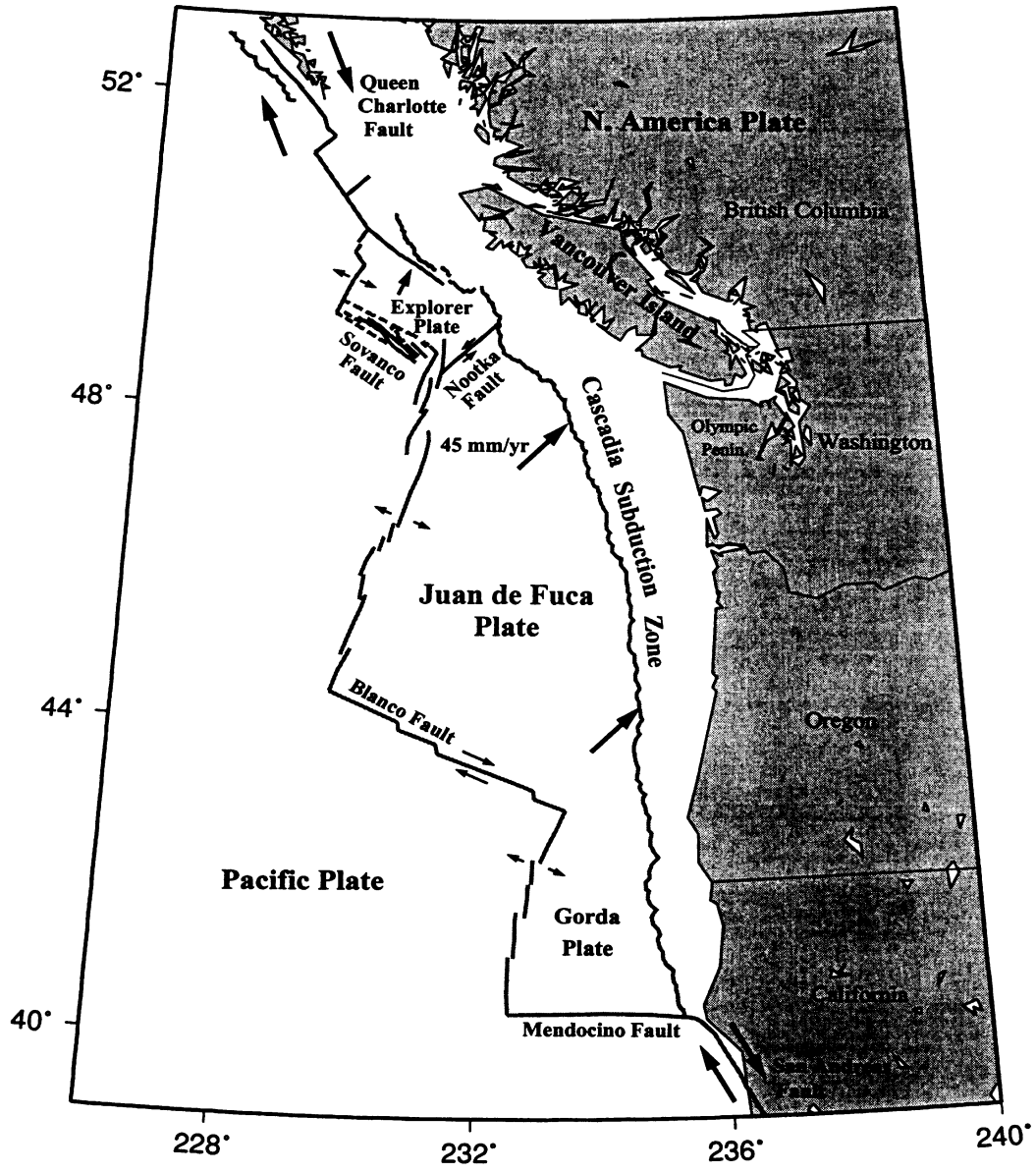

Figure 2.1: Current understanding of the plate tectonic regime of the Cascadia subduction zone. The arrows show relative plate motion.

to 600 years, most recently about 300 years ago. However, although low-level seismicity is extensive in the entire region and two major ($M > 7$) earthquakes have been observed on central Vancouver Island during this century (1918 and 1946), there have been no megathrust earthquakes on the Cascadia margin, not even small ones, during the past 200 year written historical period [Dragert, 1987; Wang et al., 1994]. In a comparison between the Cascadia margin and other convergent margins around the world, Rogers [1988] noted that this unusual lack of seismicity might well imply a potential risk for a forthcoming megathrust earthquake. Such being the case, the Cascadia margin has entered the second half of an earthquake cycle or perhaps even has approached the recurrence of the very large event.

2.2 Previous Geodetic Measurements and Results

Geodetic techniques can be used to measure the motion and deformation of the Earth's surface, which, in the case of a plate boundary area, is presumably caused by the true tectonics underneath the Earth's surface. Through geodetic measurements, strain accumulation and release in the crust can be quantified and, by inference, these quantified strain measurements provide constraints on the forces acting on the crust and on the rheology of the mantle and crust. Thus, geodetic measurements take on an important role in the study of the tectonic mechanism and in the assessment of earthquake hazard.

Extensive geodetic measurements have been carried out in the past on Vancouver Island. The conventional terrestial data include long-term tide gauge records, repeated levelling measurements, precise gravity measurements, triangulation, and

trilateration. The deformation data resolved from these measurements are summarized briefly in the following paragraphs. More detailed descriptions can be found in Dragert et al. [1994a].

Long-term tide gauge records allow a measure of coastal uplift and subsidence relative to a global sea level reference. Results from 32 to 80 years worth of tide gauge records at 9 sites in the region (2 on the inland coast, 6 on Vancouver Island or nearby islets, and 1 on the Olympic Peninsula in Washington State) show that the uplift rates range from -1.1 to +3.5 mm/yr and the outer coast of lower Vancouver Island is uplifting relative to the inland sites at a rate of 2 to 3 mm/yr. The uncertainties of these rates are estimated at approximately 0.5 to 0.6 mm/yr.

Repeated levelling surveys provide the most direct measure of relative elevation change or regional tilting across the margin. The changes are assumed to take place continuously between the times of the surveys and thereby define an average rate of ongoing crustal tilting. Three precise special order levelling lines have been repeatedly measured in the region, two on southern Vancouver Island and one on the Olympic Peninsula. The data from all the three lines show a consistent trend of uplifting along the outer coast relative to the inner coast of Vancouver Island at a rate of about 4 mm/yr with an uncertainty of about 1 mm/yr between the two ends of a 100 km levelling line.

Repeated high precision gravity surveys provide another measure of relative elevation change by measuring gravity changes which result primarily from changes in elevation, i.e., the vertical displacement. However, gravity changes also depend on strain induced density changes or redistribution of mass, so they are not exactly comparable to other vertical motion indicators. Repeated high-precision gravity surveys

have been carried out across southern Vancouver Island on one of the three levelling lines. The data indicate an uplift of the outer coast of southern Vancouver Island compared to the inner coast at a rate of 8 ±2 mm/yr assuming the Bouguer gradient (about 5 ±1 mm/yr for the Free Air gradient).

Repeated triangulation and trilateration surveys can provide 2-D horizontal strain measurements. For triangulation surveys, only two shears of the three independent 2-D strain model parameters (dilatation, pure shear, and engineering shear [Grant, 1990]) can be resolved due to the nature of the angular measurements. For trilateration surveys, all three parameters can be determined assuming the same scale throughout the surveys. Data from six triangulation or trilateration networks in the region have been analysed. The results have shown a consistent shortening across the margin, as expected for interseismic elastic shortening in the direction of convergence approximately orthogonal to the margin. For the southern Vancouver Island, the estimated shortening rates, when projected onto the profile orthogonal to the margin, range from 0.06 to 0.18 μstrain/yr (mm/km/yr) with uncertainties at ± 0.03 or ± 0.04 μstrain/yr. The directions of maximum shortening for two networks which are very close to two of the WCDA sites (UCLU and ALBH) are N18°E ±11° and N64°E ±5° (another estimate is N82°E ±8° using more historical data) respectively.

Measurements from modern extraterrestrial techniques such as **VLBI** and **GPS** have also been made in this region [Dragert et al., 1994a; Kleusberg et al., 1988] prior to the establishment of the Western Canada Deformation Array. However, since there is only one VLBI site in the region (Victoria) and very few measurement epochs, the VLBI data obtained from Victoria have not been used for the regional deformation study, but are included for global tectonic study. Two GPS surveys were carried out on one triangulation network and one EDM (Electromagnetic Distance Measurement)

trilateration network in 1986 and 1987 respectively. Baseline precisions of 0.3 to 0.5 parts per million (ppm) were achieved using the broadcast ephererides. The GPS results from one of the two surveys were compared with results previously obtained from EDM trilateration. Since the defined scales for GPS and terrestrial techniques are different, no strain analysis has been attempted using the combined GPS and terrestrial data.

In summary, geodetic surveys carried out previously on southern Vancouver Island and northern Washington State showed a horizontal shortening in the direction approximately orthogonal to the Cascadia margin. The estimated shortening rates correspond roughly to an annual displacement rate of a few mm/yr for the outer coast of southern Vancouver Island relative to the inland coast. Meanwhile, vertical uplifting was observed at the outer coast of the southern Vancouver Island relative to the inner coast. The magnitude of the uplifting rate was estimated from 2 to 8 mm/yr. Although these resolved deformation quantities from the conventional geodetic surveys have relatively large uncertainties, they provided valuable and consistent evidences of the ongoing tectonic process in the region.

2.3 Elastic Dislocation Models of Interseismic Crustal Deformation

The interseismic crustal deformation can be modelled with elastic dislocation models or viscoelastic models. The **elastic dislocation models** simply assume that the crustal deformation during the interseismic period is entirely elastic. Obviously, these models are not perfectly realistic due to the inelasticity of the crust. The **viscoelastic**

models, in contrast, are more sophisticated and give a more complete description of the crustal deformation by allowing temporal variations in the rate of deformation between earthquakes. However, in the main interseismic period, the simple elastic models are a reasonable approximation to the more sophisticated viscoelastic models. More importantly, both models result in deformations with similar spatial layout [Dragert et al., 1994a]. For these reasons, the simple elastic dislocation models are employed in the comparison with geodetic measurements.

Figure 2.2 illustrates the pattern of interseismic and coseismic deformation associated with a subduction thrust fault based on purely elastic dislocation models. During the interseismic period, the shallow seismogenic portion of the plate interface remains locked and stress accumulates. At some distance downdip, there is continuous slip throughout the earthquake cycle at the plate convergence rate. The steady slip rate decreases upward through a transition zone to zero at the downdip end of the locked zone [Hyndman and Wang, 1993]. On the continental plate, horizontal shortening occurs in the direction perpendicular to the margin and there is uplifting beyond the close vicinity of the margin. During the coseismic period, the deformation shows the opposite characteristic on the continental plate, i.e., horizontal extension in the direction perpendicular to the margin and vertical subsidence on the portion which uplifts during the interseismic period.

By comparisons with the geodetic measurements summarized in the last section, Dragert et al. [1994a] concluded that the elastic dislocation models which best fit the data have a locked zone extending about 40 to 60 km landward from the deformation front and a transition zone extending another 40 to 60 km to about the coast of southern Vancouver Island. A similar conclusion has been drawn by Hyndman and Wang [1993] through thermal arguments.

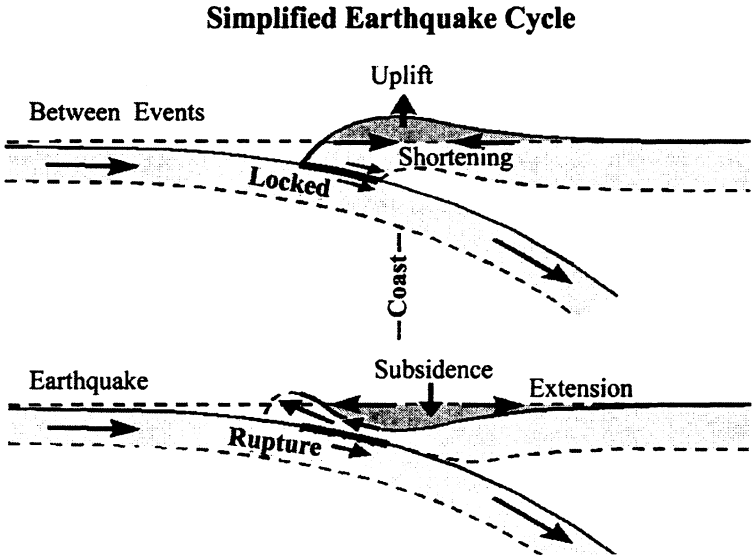

Figure 2.2: Patterns of the interseismic and coseismic deformation.

According to the best-fit elastic dislocation models, the vertical deformation on southern Vancouver Island should be everywhere uplifting at a rate decreasing with the distance to the outer coast, where the maximum rate could reach about 6 mm/yr. The horizontal shortening rate on southern Vancouver Island could be in a range from -0.02 to -0.2 μstrain/yr, also depending on the distance to the outer coast.

2.4 Chapter Summary

The tectonic setting and recent and current deformation studies of the northern Cascadia subduction zone were briefly introduced in this chapter. Based on tectonic plate models and geological data, the Juan de Fuca plate is believed to be converging with the North America plate at a rate of approximately 4.5 cm/yr across the margin. Paleoseismic data suggest that large earthquake events occurred in the past in a cyclic pattern, and so, by inference such events could occur in the future. The conventional geodetic measurements provide an approximate measure of the current deformation

and its spatial settings. In spite of the relatively large uncertainties associated with these geodetic measurements, they have shown a horizontal shortening and vertical tilting both at a rate of a few mm/yr across the region. Based on these conventional data, different deformation models and underlying geophysical processes have been studied. However, a more accurate measurement and thus better understanding of the ongoing deformation would require a modern geodetic technique such as GPS, which will be discussed in the next chapter.

Chapter 3

Western Canada Deformation Array (WCDA)

Although the terrestrial geodetic measurements summarized in section 2.2 have provided important means for crustal deformation monitoring, they suffer from several shortcomings:

1. Their uncertainties are relatively large. As shown in section 2.2, most of the measurements have an uncertainty of greater than 25% of the measurement values themselves.

2. They lack a continuous, precise, common fiducial framework which defines the space scale and datum. As a consequence, the strain analysis can only be carried out in separate dimensions, i.e., vertical and horizontal. In addition, some assumptions, such as a common scale throughout the repeated trilateration measurements, have to be made in the strain analysis.

3. They are intermittent. Thus, a continuous monitoring of the crustal deformation by means of the terrestrial geodetic techniques is not possible, which is sometimes requested by the seismological and other scientific communities.

4. They are more labour intensive, less efficient and less flexible than the modern GPS technique.

In contrast to the terrestrial geodetic techniques, the modern GPS technique can monitor crustal deformation continuously with high-precision in near-real time. It provides a precise, common fiducial framework which makes high-precision 3-D strain analysis possible.

For the reasons given above, a regional network of automated, continuous GPS tracking stations called the Western Canada Deformation Array was established in the summer of 1992 in southwest British Columbia by the Geological Survey of Canada (GSC), in cooperation with the Geodetic Survey Division (GSD) of Natural Resources Canada (**NRCan**). The WCDA is designated to provide 3-D station solutions with a few millimetre level horizontal and vertical precision, with a goal of eventually replacing the conventional terrestrial geodetic techniques. It is comprised of several continuously operating GPS tracking stations and a central processing facility at the Pacific Geoscience Centre (**PGC**). Each GPS tracking station is equipped with high standard instruments and automatic data communication link. The collected 24-hour GPS data are downloaded to PGC every day automatically. Upon completion of data downloading from all the tracking stations, the process for data quality check is then executed. The data reduction and analysis, however, is carried out in a post-event fashion using the most precise orbits available. In accordance with the objective of the WCDA, the precise orbits generated by either IGS or NRCan have been used and a well suited software package called CGPS22 has been adopted for WCDA data

reduction and analysis. GPS data processing at PGC was performed by the author from 1992 to early 1995 using NRCan orbits only, and then Mr. J. Henton took over the task using IGS orbits and also re-ran part of the early solutions whenever IGS orbits were available. It should be mentioned here that the solutions used in this study were the early solutions and the divergence between the solutions using IGS orbits and NRcan orbits is totally negligible, only at sub-millimetre level.

In section 3.1, the WCDA network configuration is described. Data acquisition and preliminary data quality assessment are presented in section 3.2. Section 3.3 gives a brief introduction of the IGS and NRCan precise orbits and section 3.4 summarizes this chapter.

3.1 Network Configuration

The WCDA is a GPS network with a growing number of permanent stations. The initial set of three permanent stations which were operational by September 1992 included **DRAO** (Dominion Radio Astrophysical Observatory, Penticton), **ALBH** (Albert Head, southern Vancouver Island), and **HOLB** (Holberg, northern Vancouver Island). Stations added later in the region included **WILL** (Williams Lake) in October 1993, **UCLU** (Ucluelet, western Vancouver Island) in May 1994, and NANO (Nanoose Harbour, eastern Vancouver Island) in May 1995. **Figure 3.1** shows the basic tectonic setting of the region and the geometric configuration of the WCDA prior to May 1995. The distances of the four WCDA sites from DRAO are shown in Figure 3.1 and range from 302 to 627 km. Through cooperative work with the University of Washington the station NEAH (Neah Bay) was also established on the northwest coast of Washington in July 1995. Additionally, there are two WCDA

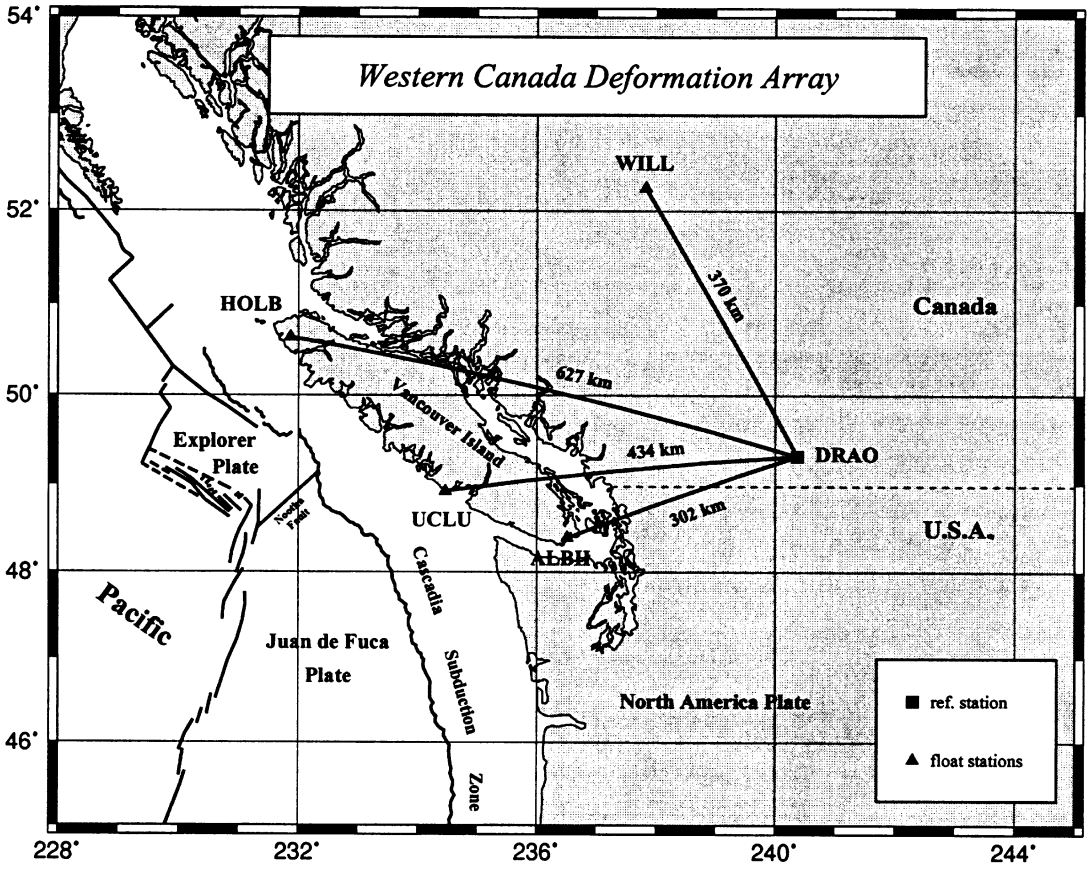

Figure 3.1: Western Canada Deformation Array up to May 1995.

sites outside British Columbia: WHIT (Whitehorse, Yukon; June 1996) and FLIN (Flin Flon, Manitoba; June 1996), and PGC1, a site at the Pacific Geoscience Centre (**PGC**), is used only for equipment tests. The geophysical locations of most of the permanent stations were intended to span the most seismically active and most densely populated region of southwest Brtish Columbia. As this study only concerns the permanent WCDA stations operational before May 1995, the stations added later will not be included in the following discussions.

The selection of a permanent site for GPS tracker installation is constrained by a number of factors including clean tracking environment, stability, security, availability

of power, communications, bedrock, and integration with other existing facilities and geophysical measuring systems. Mobile VLBI measurements and absolute gravity observations have been carried out at DRAO and ALBH, and HOLB and DRAO are also seismometer sites in the Canadian Seismic Network. All of the permanent sites have inner and outer local stability networks with about 8 monuments in total at distances of a few hundred metres for the former and 10 km for the latter, in order to monitor the stability of the main tracker sites [Dragert et al., 1995].

Table 3.1 gives some details of the WCDA tracking sites as of May 1995 [Dragert et al., 1994b]. It should be emphasized in particular that the instrumentation setup, including receiver, operating software (O/S), antenna and clock, at each site has been changed many times since the starting operational date. For example, Rogue (SNR-8, SNR-800) and Mini Rogue (SNR-8100) receivers have been used by some of the WCDA sites before the present Turbo Rogue (SNR-8000) receivers were deployed; the antennas were changed from Dorne Margolin type B to type T in 1994; and the receiver operating software has also been upgraded a number of times. Most of these changes had little or no impact on post-processing of the data, but some of the antenna changes were found to have unexpected effects on the final solutions, as will be discussed in Chapter 6. For convenience of later discussions, the antenna setup at each WCDA station from September 1, 1992 to April 5, 1995 is given in **Table 3.2**. In the table, "B" and "T" denote Dorne Margolin antenna type B and type T respectively. "R" represents the plexi-glass dome (or radome). The number following the antenna type is the serial number. Entries with "-" denote no change during the period.

Two receiver tests were carried out before the receivers were installed at the tracking sites. The first test of the Mini Rogue receivers reported by Kouba and Chen

Table 3.1: Particulars of GPS tracking stations of the WCDA network.

	ALBH	DRAO	HOLB	WILL	UCLU
Location	Albert Head	Penticton	Holberg	Williams Lake	Ucluelet
Latitude	N48.3897	N49.3225	N50.6403	N52.2369	N48.9256
Longitude	E236.5125	E240.3750	E231.8650	E237.8322	E234.4587
Elevation	32 m	542 m	550m	1097 m	10 m
Operational date	92/05	91/02	92/07	93/10	94/05
Receiver	Turbo Rogue	Turbo Rogue	Turbo Rogue	Turbo Rogue	Turbo Rogue
O/S vers.	3.0.32.2	3.0.32.3	2.8.32.1	0.0 SFG2	2.8.32.1
Antenna	DM+C	DM+C	DM+C	DM+C	DM+C
Frequency standard	Cesium	Cesium Super Tube	Rubidium	Rubidium	Rubidium
VLBI co-loc.	Yes	Yes	No	No	No
Stab. net.	Yes	Yes	Yes	Yes	Yes
UPS	Yes	Yes	Yes	Yes	Yes
Marker	Concrete Pier Forced Centre	Concrete Pier Forced Centre	Concrete Pier Forced Centre	Concrete Pier Forced Centre	Concrete Pier Forced Centre

* DM+C: Dorne Margolin antenna with choke ring.

[1992] showed that the root-mean-square (rms) receiver internal noise estimates (no antenna noise included) of L_1 and L_2 double-differenced phase data are 0.2 and 0.4 mm respectively. For the second test of three Turbo Rogue receivers, these noise indicators were estimated to be 0.2 and 0.3 mm, as reported by Chen and Dragert [1992]. Consequently, the receiver internal noise for undifferenced L_1 and L_2 phase data is at the level of 0.1 to 0.2 mm. For undifferenced P_1 and P_2 pseudorange data, the rms receiver internal noise is at 1 to 3 cm level for both receiver types in the two tests.

Table 3.2: Antenna setup during 1992-1995 at WCDA tracking stations.

Station	09/01/92 - 02/09/94	02/10/94 - 04/13/94	04/14/94 - 05/02/94	05/03/94 - 06/20/94	06/21/94 - 01/10/95	01/11/95 - 04/05/95
ALBH	B119 + R	-	T172 + R	-	-	T368 + R
DRAO	B105 + R	T174 + R	-	-	-	-
HOLB	B120 + R	-	-	T383 + R	-	-
WILL	T168	-	-	-	T168 + R	-
UCLU				T380 + R	-	-

All the GPS tracking sites are equipped with telephone lines and high speed (19.2 kbps) modems for fast daily data transmission to the central facility at PGC near Victoria. Highly stable external frequency standards are used to take over from the internal oscillators of the GPS receivers at all WCDA sites. These external frequency standards have long term stability of $\pm 2 \times 10^{-12}$/month for the HP 5061B Cesium Super Tube, $\pm 3 \times 10^{-12}$/month for the HP 5061A Cesium frequency standard, and ± 1 to 5×10^{-12}/month for the HP 5065A and the Osborne (Efratom FRS) Rubidium frequency standards.

To ensure long term local stability, the GPS antennas are mounted on concrete, forced-centre piers. Each pier is anchored in bedrock using 5/8 inch or larger steel re-enforcement bars to a depth of 1.5 to 3 metres (site dependent). The concrete piers vary in dimension and height. At ALBH and WILL, the piers are up to 3 metres in height and 60 cm in diameter due to security concerns (human and wildlife) and/or snow accumulation. All antennas are covered by hemispherical, unheated plexi-glass domes to prevent snow/ice accumulation within the choke rings and to discourage birds from nesting on the antennas.

3.2 Data Acquisition

Data collected at each WCDA tracking station include dual-frequency (L_1, L_2) pseudoranges (P_1, P_2) as well as carrier phases (ϕ_1, ϕ_2) from all visible satellites above a 10-degree elevation angle, up to a maximum of 8 satellites, at a rate of one sample per 30 seconds. When the Anti-Spoofing is switched on, however, the access to P-code is denied and alternatively Turbo Rogue receivers can operate in cross-correlation mode and produce a C/A code pseudorange (C_1), ϕ_1 carrier phase, synthetic P_2-like pseudorange (C_2) and ϕ_2-like carrier phase (ϕ_2'). $(C_2 = C_1 - X$, where X is a $(L_1 - L_2)$ cross-correlated pseudorange, and $\phi_2' = \phi_1 - \delta$, where δ is a $(L_1 - L_2)$ cross-correlated carrier phase).

The raw data collected at the GPS tracking stations are temporarily stored in the CONAN binary, compressed format in the receivers' local memory (4 Mb of non-volatile RAM) which forms a circular buffer capable of holding about seven days worth of data. Every 24 hours (at 0:00 UTC), the data are downloaded from each tracking site through an automated process running on a Sun Sparc workstation at PGC. It typically requires 8 minutes or so to download the daily binary data of about 400 Kb from each station using XMODEM protocol.

Having been downloaded, the data are then automatically validated using two programs developed by GSD: GIMP (GPS Ionospheric and Multipath Program) and DCRAP (Differential Corrections to Ranges and Positions). The two programs preliminarily assess the quality of the data, primarily the pseudoranges, and give a variety of statistics at station level, such as the number of observations, cycle slips and gaps, the level of multipath, the clock offset and drift, etc. The full quality inspection of the data, especially the carrier phases, is carried out in the post-processing of the

data.

3.3 The NRCan and IGS Precise Orbits

There are seemingly four options of GPS satellite orbit data acquisition for the WCDA data reduction: the broadcast ephemerides, the estimated orbits using WCDA data only, the improved orbits using WCDA data and data from a few IGS stations, and the precise orbits computed using global data sets. Since the precision pursued for the WCDA is the a few millimetre level for baselines of lengths from 302 to 627 km, or equivalently, a few parts per billion (ppb) in terms of relative precision, the broadcast ephemerides with at best metres of accuracy is obviously insufficient for this goal. For the second option, due to the regional size of the WCDA network, orbit determination using WCDA data only can hardly meet the requirements of high consistency and precision, not to mention the greatly increased complexity and amount of work. The third option is not quite realistic because of the limited capability of CGPS22 in orbit determination and also because of the reasons for the second option. Therefore the only realistic and also the most efficient choice is to use precise orbits with sub-metre precision, continuously and promptly computed by utilizing data from a set of globally distributed stations yet with a reasonable density of stations over Canada.

Presently, precise orbits from many IGS analysis centers may have all the merits just mentioned. However, for historical reasons and consideration of precision and station coverage over Canada, the NRCan and IGS precise orbits are comparatively more preferable, and thus have been adopted for the WCDA data reduction. The two sources of precise orbits are introduced in the following paragraphs.

The NRCan orbital products are produced by the Master Active Control Station (MACS) of the Canadian Active Control System (CACS) of NRCan's Geomatics Canada in Ottawa, Ontario. The MACS to date uses data from 6 to 9 Canadian Active Control Points (**ACP**s) including several WCDA sites (ALBH and DRAO continually; HOLB and WILL occasionally), and up to 25 IGS global core stations. Daily precise orbits and Earth orientation parameters (EOP) have been computed continuously in a weekly cycle and archived at GSD since August, 1992. The software adopted for NRCan orbit computation is the **GIPSY/OASIS II** [Blewitt, 1993] using a sophisticated Kalman filtering algorithm and thorough mathematical modellings. Typically the NRCan orbit/EOP products are submitted to a public FTP site at MACS within one week of the last observation. This delay does not pose a serious problem for the WCDA data processing. Quality assessments on NRCan products have been carried out initially by Kouba et al. [1993] and later routinely by the IGS on a weekly basis, by comparing the NRCan orbit/EOP with products from other IGS analysis centers or the IGS combined orbits, and with the **IERS** (International Earth Rotation Service) series of EOP. In the initial assessment, a precision of about 20 cm for satellite orbits and 0.5 milliarc seconds (mas) for EOP parameters was reported. The precision has been getting better as the modellings in orbit determination are getting refined. The current precision for NRCan orbit/EOP products is believed to be approximately 10 cm for orbits and 0.2 mas for EOP [Lahaye et al., 1997]. Obviously, a precision of this level satisfies the requirements for the WCDA data reduction very well.

The NRCan orbit files are generated in two different formats: SP1 and SP3. In SP1 format, the file contains 24 hours' worth of tabulated X, Y, Z coordinates in ITRF Earth-centred Cartesian system and first order derivatives with respect to time (i.e., velocity components), at intervals of 15 minutes, for each of the GPS satellites. In

SP3 format, the velocity components are substituted with satellite clock offsets with respect to a well-behaved clock reference (e.g., the Hydrogen Maser at the Algonquin Radio Observatory), also tabulated at 15 minute intervals. The NRCan EOP files contain the daily solutions of the pole position (x, y) in units of 10^{-5} arc seconds, UT1-UTC in μs, and length of day (LOD) in $\mu s/d$, compiled on a weekly basis.

Along with the orbit/EOP files, a summary file is also compiled and archived weekly for users' interests. It's worth mentioning that although data from DRAO, ALBH, and HOLB or WILL have been included in the NRCan orbit determination, none of the sites has been fixed. Besides, a 450-second (7.5 minutes) sample interval is used in the orbit computation, which is different from the 2-minute sample interval used in the WCDA data reduction. The two facts arise from the differences of purpose at Geomatics Canada and PGC, and validate the fact that the WCDA data reduction is not simply reproducing or back-substituting into the NRCan solutions. In fact, a better precision of the station solutions in the WCDA data analysis should be expected compared to the NRCan global solutions, due primarily to the reduced systematic errors compared to those present in global scale anlyses and to the higher sample rate.

The IGS orbits are in fact a combination of the precise orbits generated by several IGS analysis centers including NRCan. The combination is performed by weighted averaging and removing small reference frame errors from the individual precise orbits with respect to a common reference frame. The IGS orbits are believed to be comparable to, or better than, the best individual orbits [Beutler et al., 1995]. However, considering that the IGS orbits became available only after November 14, 1993, and NRCan orbits are comparable with the IGS orbits, the NRCan orbits therefore have been used routinely throughout the WCDA data reduction discussed in this thesis.

The IGS orbits are used only for test purpose in this study, though they have replaced the NRCan orbits in the WCDA data reduction conducted at PGC since May 1995.

3.4 The WCDA in Summary

The basic components and advantages of the WCDA were introduced in this chapter. In summary, the WCDA is a network of permanent GPS trackers to accurately monitor the crustal deformation across the northern Cascadia subduction zone. It is equipped with state-of-the-art instrumentation including Rogue GPS receivers and atomic frequency standards, and the operation of this network is highly automated. To acquire the highest precision, the WCDA data are processed with NRCan or IGS precise orbits using a scientifically oriented CGPS22 software package, which is going to be elaborated on in the next chapter.

Chapter 4

GPS Data Analysis Software Package CGPS22

The software package used for the WCDA GPS data reduction and analysis is the Canadian version of GPS22 (CGPS22). It evolved from an early version of the software package GPS22 developed by the U.S. National Geodetic Survey (NGS). Since its acquisition in 1988, GPS22 has undergone extensive modifications, improvements, rewriting and additions of new modules [Chen, 1994]. To distinguish this modified version from the original, it has been christened CGPS22. **Figure 4.1** illustrates aspects of the software's functionality. The shadowed blocks in the figure are those usually not utilized in the WCDA data reduction, while the rest represent the procedures used routinely. The data flow in Figure 4.1 is controlled by a series of command files written in Unix shell script to make the procedure fully automated.

To restrict the length of this chapter, except for some newly developed models and those mathematical models very important for the forthcoming discussions,

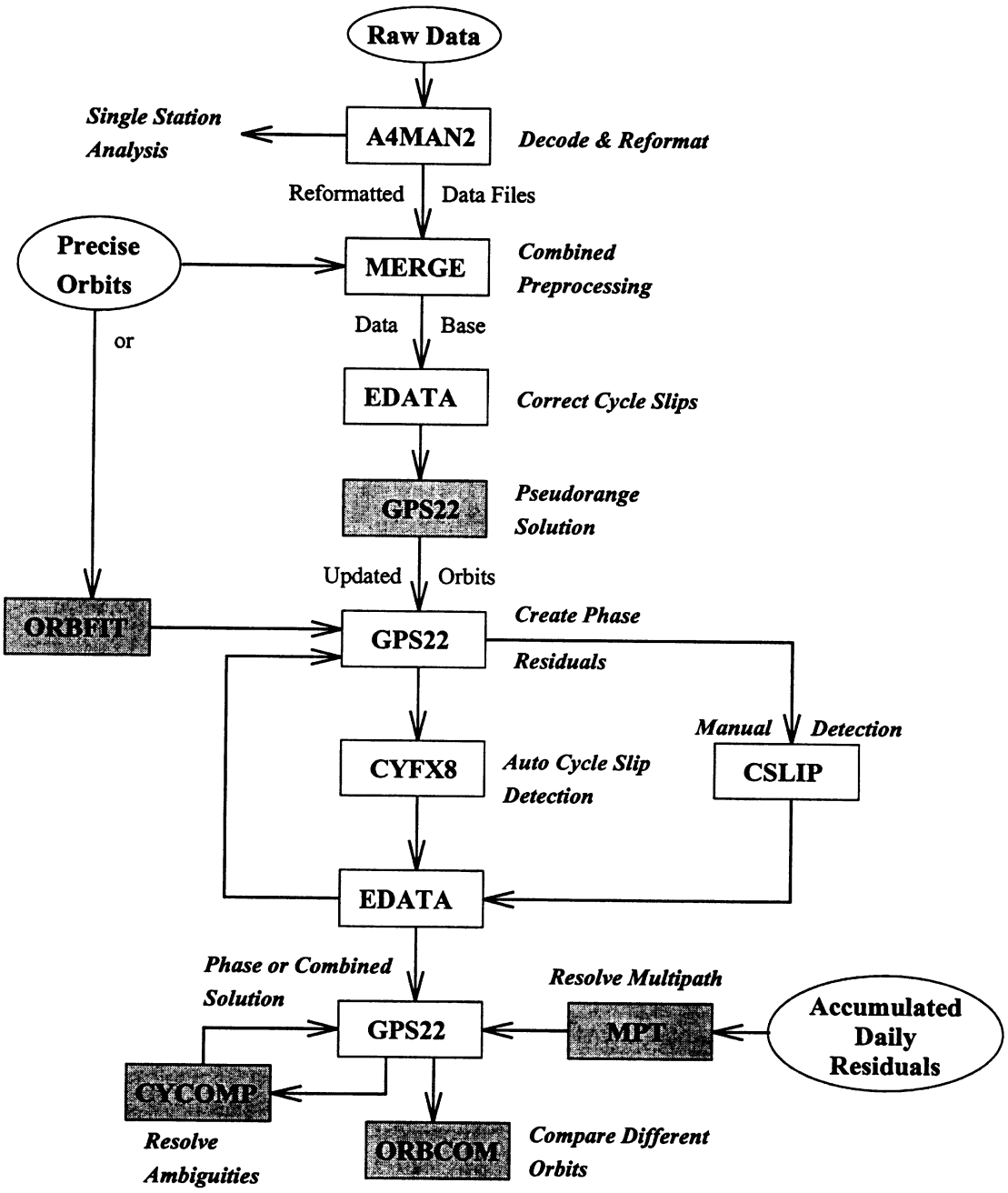

Figure 4.1: Flow chart of CGPS22. The shadowed blocks are usually not used for the WCDA data reduction.

most other mathematical models are not described. For the same reason, the model descriptions in this chapter are mainly narrative. The first section of this chapter presents a brief introduction to the history of CGPS22 software development. Next, the descriptions of the methods and procedures used in the pre-processing are given in section 4.2. The measurement models and algorithms used in the CGPS22 main processor are described in section 4.3, and the procedures and methods used in the post-processing are given in section 4.4. The last section describes the control and auxiliary modules accompanying CGPS22.

4.1 History of the Software Development

As stated at the beginning of this chapter, CGPS22 originated from GPS22, which was designed by NGS to process GPS observations and perform parameter estimation for high precision GPS relative positioning. The original version was ported onto an HP-900 mini-computer in 1988 at the Geophysics Division of Geological Survey of Canada (GD/GSC) [Kouba and Popelar, 1990]. The modification and enhancement of CGPS22 then proceeded in three stages. The following paragraphs summarize the main improvements corresponding to each of the stages in chronical order.

In the first stage from 1988 to 1990, a few improvements were made at GD/GSC [Kouba and Popelar, 1990]:

- stochastic modelling of the tropospheric parameters taking both the temporal and spatial correlations into account,
- *a priori* orbit weighting,
- solid Earth tides and ocean tide loading corrections,

- orbit representation in Chebyshev coefficients,
- interactive and batch processing.

In the second stage from 1990 to 1992, further improvements were made also at GD/GSC [Kouba and Chen, 1992]:

- coarse single station cycle slip detection and ionosphere/multipath analysis by evaluating a variety of phase/pseudorange combinations and by performing pseudorange smoothing by carrier phases,
- **RINEX** (Receiver INdependent EXchange) format and Rogue CONAN binary format incorporated,
- improved short-arc modelling including GEM-T2 (8×8) Earth gravity field, Sun and Moon direct attractions and nominal solar radiation pressure,
- pseudorange weighting scheme according to Euler and Goad [1991],
- fully automated initial cycle ambiguity fixing by means of P-code pseudoranges,
- carrier phase multipath monitoring and removal in the post-processing stage by averaging several days' worth of properly aligned phase residuals,
- separate pseudorange and combined (pseudorange and carrier phase with proper relative weighting) double-difference solutions,
- ocean tide loading according to Pagiatakis [1982].

In the third stage from 1992 to the present, the CGPS22 package was first ported from the HP-900 mini-computer at GD/GSC to a Sun Sparc workstation in the Unix environment at PGC. In order for CGPS22 to satisfy the requirements for the WCDA

data analysis, modifications and enhancements were made at PGC in cooperation with Dr. Jan Kouba of GSD and at the University of New Brunswick [Chen, 1994]. These included:

- daily 24 hour data processing using precise orbits in SP1 or SP3 formats (each satellite pass is represented by a set of polynomials fit to the precise orbit),
- fully automated selection of reference satellites,
- more phase ambiguity parameters allowing for a satellite associated with long data gaps or multiple satellite passes within a day,
- optional initial normal matrix input from the previous day's solution,
- GEM-T3 gravity field (8×8),
- pole tide correction due to Yoder [Sovers and Border, 1987],
- second order ionospheric delay correction according to Bassiri and Hajj [1993],
- a new graphical user interface module for manual and interactive cycle slip and outlier editing,
- carrier phase weighting scheme according to Kouba et al. [1993],
- improved automatic cycle slip detection program which now can do both forward and backward searching such that the cycle slips at two ends of a satellite pass can be detected more easily,
- multipath removal by means of a spectral estimation technique,
- added options for the tropospheric mapping function including Herring's and Niell's models recommended by Mendes and Langley [1994],

- optional Saastamoinen model for the tropospheric zenith delay [Saastamoinen, 1973],
- added schemes in the estimation of tropospheric delays: estimating total combined wet and dry (non-hydrostatic and hydrostatic) delays without model corrections, and estimating a stochastic wet delay and a constant dry delay separately.

4.2 Pre-processing of GPS Data

The ultimate goal of the pre-processing with CGPS22 is to form a data base including a clean (cycle slip and outlier free) data file, an orbit file, and a header file containing all station information and other miscellaneous data, for the main-processing. To realize this, three steps have to be taken: single station pre-processing, combined pre-processing, and cycle slip editing. The three steps are described briefly in the following subsections.

4.2.1 Single Station Pre-processing by A4MAN2

At this stage, the raw data recorded in receiver dependent formats such as the Rogue receiver formats (including compressed CONAN binary, standard (STD), and tracking (TRK)) or the RINEX format are first reformatted into a compact internal binary format which is specific to CGPS22. The carrier phases are then decimated from the receiver sample interval to the interval specified for the data reduction by the user. Pseudorange smoothing by carrier phases can be requested and carried out

whenever possible. Coarse cycle slip detection using combinations of carrier phases and pseudoranges can be implemented. The plots of various linear combinations of the data such as wide-lane, narrow-lane, ionosphere, and multipath can be output, along with system messages and tracking status for data quality control and trouble shooting.

4.2.2 Combined Pre-processing by MERGN

The reformatted station observation files, the precise orbit file in SP1 or SP3 format, station information files and the setup input file are processed together to form a combined data base. The station information files contain the station coordinates, antenna offsets from the GPS monument, $L_1 - L_2$ phase centre offsets, and surface meteorological data. The setup input file specifies the values of such processing parameters as the satellites to be used, the time window, the data interval, the elevation cutoff angle, the ephemerides type, etc.

In order to calculate station clock offsets, the carrier phase and pseudorange observations are corrected using the satellite clock offsets represented by a linear polynomial (order 2) derived from the clock offsets given in the precise orbits file in SP3 format. By this correction, the time reference is now defined to be the same as the one specified in the precise orbits. When SA (δ technique) is activated, the effect of the high-frequency satellite clock dithering cannot be represented by the simple linear polynomial, so that this dithering effect remains in the observations. Although in double-differencing algorithm used in our main-processing it is not necessary to correct normally small clock offsets ($\ll$ 1 ms), the calculation of station clock offsets can help monitor the performance of the station frequency standards and help

trouble-shooting when a problem arises.

The initial cycle ambiguities of the carrier phases are estimated using wide-lane and narrow-lane combinations. When true P-code pseudoranges are available, a resolution of approximately one cycle can be achieved for the estimated ambiguities. In this case, large cycle slips can also be detected to the same resolution. However, when P-code pseudoranges are not available, the resolution of cycle slip detection is greatly degraded to a level of tens of cycles, and thus cycle slip detection is disabled to prevent false detections.

A quadratic polynomial fit of the station clock offsets is carried out using pseudoranges for each of the stations. The estimated polynomials refer to the same time reference as mentioned above. Again, the effect of the high-frequency satellite clock dithering remains because it cannot be absorbed by the quadratic polynomials.

In order for the main-processing to have a quick and accurate way of interpolating the satellite orbit and clock data, a set of Chebyshev polynomials of order 15 are computed by least squares fit for each satellite pass. The advantage of Chebyshev polynomials is their efficiency, i.e., having the same accuracy with a lower order compared to other types of polynomials.

A pseudorange rms (root-mean-square) error computed from phase/pseudorange combinations is estimated for each of the stations as the data base is being created. This rms error is an indicator of the pseudorange measurement noise (plus multipath effect, if any) and it can be used as a noise scale factor in the pseudorange weighting in the main-processing.

If the approximate coordinates of a new station are not accurate to within a

metre, a triple-difference phase solution can be carried out. The solution is usually run iteratively until it converges.

4.2.3 Cycle Slip Editing

The purpose of this stage of pre-processing is to fix all remaining cycle slips and remove outliers. At present, it is fulfilled by an automatic module CYFX8 and a manual module CSLIP (**Figure 4.1**).

The automatic module is based on a search technique using triple-differenced dual-frequency carrier phases φ_1 and φ_2, and double-differenced φ_3 (**ionosphere-free combination** of φ_1 and φ_2, i.e., $\varphi_3(cm) \approx 48.44 \times \varphi_1(cy) - 37.75 \times \varphi_2(cy)$) to detect cycle slips and outliers. Since triple-differencing eliminates the initial phase ambiguities as well as all the errors in common to the stations, satellites and consecutive epochs, any cycle slip or outlier will create an isolated peak in the triple-differences. The double-differenced φ_3 is a constraint on the triple-difference estimates of cycle slips, and also helps to detect small cycle slips where triple-differences may fail. For example, a slip of one cycle in φ_1 only can cause a jump of +48.44 cm in φ_3; and -37.75 cm for a slip of one cycle in φ_2 only; and +11.69 cm for a slip of one cycle in both φ_1 and φ_2. In contrast, a big cycle slip of 7 cycles in φ_1 and 9 cycles in φ_2 will make an indistinguishable jump of just -0.67 cm in φ_3. Therefore, the double-differenced φ_3 and triple-differenced φ_1, φ_2 are complementary in cycle slip editing.

The automatic searching algorithm accumulates the rate of change in the double-differences and triple-differences. After a few epochs, the accumulated rate of change will be stablized and any abrupt change in the rate hints of the occurence of a cycle

slip or outlier. There are two searching modes in the algorithm, one forward and one backward. For the forward mode, a cycle slip at the beginning of a satellite pass may be difficult to detect because the accumulated rate has not been stablized sufficiently. The backward mode gives a remedy to the problem because the beginning of the satellite pass now becomes the end of the searching pass.

For well-behaved dual-frequency receivers in normal situations, the automatic module rarely fails. Very few, if any, cycle slips would escape the automatic detection. However, in extreme situations such as strong multipath or RF (radio frequency) interference, large ionospheric variations during geomagnetic storms, large clock bias and drift rate, and "buggy" receiver operating software, massive false detections could occur. For instance, the Turbo Rogue operating software at ALBH was once replaced by version 3.0, which, as later turned out, had some bugs that could produce fractional cycle slips in L_2 carrier phases [Young, 1995]. Another example is that ALBH has experienced strong multipath at low elevation angles. In the first example, the automatic module output many false detections, while in the second example, the failure repeated every day at the same sidereal epoch (about 4 minutes per day ahead of UT time).

After the automatic cycle slip editing, the manual module can be run interactively to examine the quality of the automatic editing and detect any remaining cycle slips and outliers. It uses window graphics of double-differenced φ_1, φ_2, and φ_3 residuals. Cycle slips and outliers are visually inspected, and a search algorithm in the program can determine the most probable size of the slip on both L_1 and L_2 at the point clicked on the display. The residuals after the correction of the determined cycle slip are displayed to show how good the correction is, and the determined cycle slip is subject to the analyst's acceptance.

After the two steps of cycle slip editing, a 100% clean data set can usually be guaranteed and it is then ready for the main-processing.

4.3 Measurement Models and Algorithms in the CGPS22 Main Processor

Proceding to the descriptions about the main-processing procedure with CGPS22, some important measurement models and algorithms used in the CGPS22 main processor are introduced in this section. The models to be presented below are those either newly developed or already applied to the WCDA data analysis and they are also critical in the forthcoming error analysis.

4.3.1 Carrier Phase Observations

There are two basic GPS observables: the pseudorange and the carrier phase. As carrier phases are much more precise than pseudoranges, they are the major observations used in high-precision GPS relative positioning. This subsection gives detailed observation equations for carrier phases. Those for pseudoranges can actually be derived analagously to the observation equations for carrier phases except for few differences, therefore they are not presented here.

The observation equation of a carrier phase measurement from station i to satellite j can be expressed as [Wei, 1986]

$$\varphi_i^j = -\frac{f}{c}\rho_i^j - fdt^j + f(1 - \frac{\dot{\rho}_i^j}{c})dT_i - \frac{f}{c}(I_i^j + T_i^j) + N_i^j \tag{4.1}$$

where f is the L_1 or L_2 carrier frequency, c is the speed of light in a vacuum = 299 792 458 m/sec, ρ_i^j is the geometric range between the station i at the signal reception time and the satellite j at the signal transmission time, $\dot{\rho}_i^j$ is the first derivative of ρ_i^j with respect to time, dt^j is the satellite clock error, dT_i is the station clock error, I_i^j is the ionospheric delay, T_i^j is the tropospheric delay, and N_i^j is the initial integer ambiguity. The unit of the carrier phase here is number of cycles. The terms due to relativity, multipath and system noise are neglected in equation (4.1).

In order to remove the clock error terms in equation (4.1), the operators called single-differencing and double-differencing are applied. The operations are defined as

$$\texttt{single}-\texttt{differencing}: \quad \varphi_{ik}^{l} = \varphi_k^l - \varphi_i^l \tag{4.2}$$

$$\begin{aligned} \texttt{double}-\texttt{differencing}: \quad \varphi_{ik}^{jl} &= \varphi_{ik}^{l} - \varphi_{ik}^{j} \\ &= (\varphi_k^l - \varphi_i^l) - (\varphi_k^j - \varphi_i^j) \end{aligned} \tag{4.3}$$

where $\varphi_i^j, \varphi_k^j, \varphi_i^l, \varphi_k^l$ are the carrier phases measured simultaneously at stations i and k to satellites j and l.

After double-differencing, the observation equation (4.1) becomes

$$\begin{aligned} \varphi_{ik}^{jl} &= -\frac{f}{c}\rho_{ik}^{jl} - \frac{f}{c}[(\dot{\rho}_k^l - \dot{\rho}_k^j)dT_k - (\dot{\rho}_i^l - \dot{\rho}_i^j)dT_i] - \frac{f}{c}(I_{ik}^{jl} + T_{ik}^{jl}) + N_{ik}^{jl} \\ &= -\frac{f}{c}\rho_{ik}^{jl} - \frac{f}{c}[\dot{\rho}_k^{jl} bT_k + \dot{\rho}_{ik}^{jl} dT_i] - \frac{f}{c}(I_{ik}^{jl} + T_{ik}^{jl}) + N_{ik}^{jl} \end{aligned} \tag{4.4}$$

where $bT_k = dT_k - dT_i$ is the relative clock bias of station k with respect to the reference station i.

Evidently, the satellite clock errors are completely removed in equation (4.4). The double-differenced station clock errors are reduced by a factor of $c/\dot{\rho} \approx 10^5$ compared to the single-differenced clock errors. Therefore, the double-differenced carrier phases

are insensitive to the receiver clock errors, though these errors can be estimated approximately from the double-differenced carrier phases.

Since the ionospheric delay I in first-order approximation is proportional to $1/f^2$, a linear combination of dual-frequency carrier phases can be devised to eliminate the first-order effect of ionospheric delay. It is called the **ionosphere-free** combination or L_3 combination. In units of length, it can be expressed as

$$\begin{aligned} \varphi_i^j(L_3) &= \frac{c}{f_2^2 - f_1^2}[f_1 \cdot \varphi_i^j(L_1) - f_2 \cdot \varphi_i^j(L_2)] \qquad (4.5) \\ &= \rho_{ik}^{jl} + [\dot{\rho}_k^{jl} bT_k + \dot{\rho}_{ik}^{jl} dT_i] + T_{ik}^{jl} + N_{ik}^{jl}(L_3) \end{aligned}$$

Here, the initial ambiguity term $N_{ik}^{jl}(L_3)$ loses the integer property. A second disadvantage of the L_3 combination is that its noise level is about three times that of L_1 or L_2 carrier phases.

There are two types of correlations involved in the double-differenced obseravtions. One is the **mathematical correlation** that results from the double-differencing operations. The other is the **physical correlation** caused by unmodelled or mismodelled systematic errors that are temporally and/or spatially correlated. Propagation anomalies (atmospheric inhomogeneities) are one significant source of the physical correlation [Wells, 1986]. The mathematical correlation is easy to handle because we know exactly how the observations are correlated. By the Choleski decomposition method or equivalently the Gram-Shimdt orthonormalization method, the mathematical correlation can be completely eliminated from the double-differenced observation sequence before the observations come into the adjustment process introduced in subsection 4.3.7. In contrast, the physical correlation is much more difficult to deal with because we do not know exactly how it behaves. Two attempts have been made to

partly account for the physical correlation: a weighting scheme applied to the observations introduced in subsection 4.3.8 and the stochastic tropospheric modelling with spatial correlation taken into account as described in subsection 4.3.6. However, the physical correlation has not posed a significant problem in most cases. Therefore, it has rarely been considered so far in the literature.

4.3.2 Antenna Phase Centre Corrections

There are two antenna phase centre offsets that need to be corrected. One is the offset between the GPS ephemeris reference point (satellite centre of mass) and the phase centre of the satellite transmitting antenna. This offset is corrected by [Sovers and Border, 1987]

$$\begin{cases} \vec{r}_{phase} = \vec{r}_{mass} + (0.211\vec{x} + 0.886\vec{z}) \quad \texttt{metres for Block I satellites} \\ \vec{r}_{phase} = \vec{r}_{mass} + (0.279\vec{x} + 0.952\vec{z}) \quad \texttt{metres for other satellites} \end{cases} \tag{4.6}$$

where $\vec{r}_{phase}$ and $\vec{r}_{mass}$ are satellite position vectors referenced to the phase centre of the satellite antenna and to the centre of mass respectively, $\vec{z}$ is the unit vector from the mass centre of the satellite to the geocentre, $\vec{y}$ is the normalised cross product of $\vec{z}$ with the unit vector from the satellite to the Sun, and the unit vector $\vec{x}$ completes a right-handed coordinate system.

The second offset is the one between the receiver antenna phase centre and the bench mark. It can be easily corrected by

$$\vec{R}_{phase} = \vec{R}_{mark} + \vec{R}_{offset} \tag{4.7}$$

where $\vec{R}_{mark}$ and $\vec{R}_{phase}$ are the station position vectors referenced to the bench mark and to the antenna phase centre respectively, and $\vec{R}_{offset}$ is the offset vector pointing from the bench mark to the antenna phase centre.

4.3.3 Relativistic Effect

A **relativistic rate correction** for satellite clocks is applied to the measurements. It can be written as [Sovers and Border, 1987]

$$\Delta t_{rel} = 2\vec{r}(t_{tr}) \cdot \dot{\vec{r}}(t_{tr}) \tag{4.8}$$

where $\vec{r}(t_{tr})$ is the satellite geocentric position vector at the time of signal transmission t_{tr}. Although this effect can be completely removed by double-differencing, the correction can benefit the calculations of partial derivatives.

4.3.4 Solid Earth Tides Displacement

The **solid Earth tide** is the Earth's elastic response to the time-varying forces exerted by celestial bodies such as the Sun and the Moon. This tidal phenomenon is well understood and can be modelled to an accuracy of about 2 mm [Baker et al., 1995].

The displacement due to solid Earth tides is modelled in terms of dimensionless parameters called the Love numbers. The first Love number h is defined as the ratio of the elastic radial displacement of a mass element of the real Earth to the radial displacement of the corresponding element of a hypothetical fluid Earth. The third Love number or Shida's number l is defined as the ratio of the horizontal elastic displacement of an actual mass element to the horizontal displacement of the corresponding element of a hypothetical fluid Earth. For degree 2, which is the dominant harmonic term in tidal potentials, $h_2 = 0.62$ and $l_2 = 0.08$ [Vaniček and Krakiwsky, 1982]. The vector of tidal displacements are expressed in the North-East-Upward

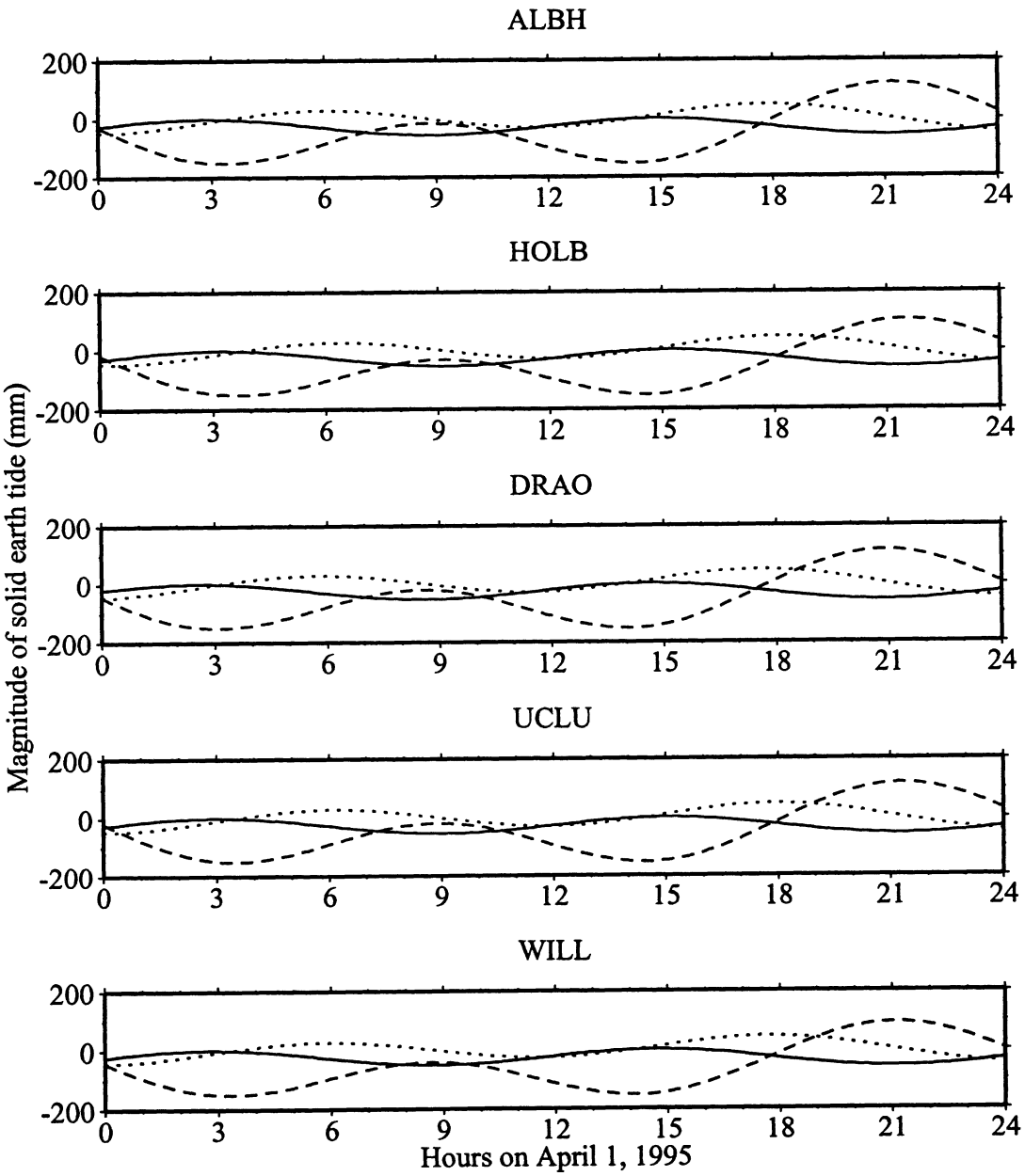

Figure 4.2: Daily solid Earth tide effects at each of the WCDA sites. The solid line denotes the north component, the dotted line the east component, and the dashed line the upward component.

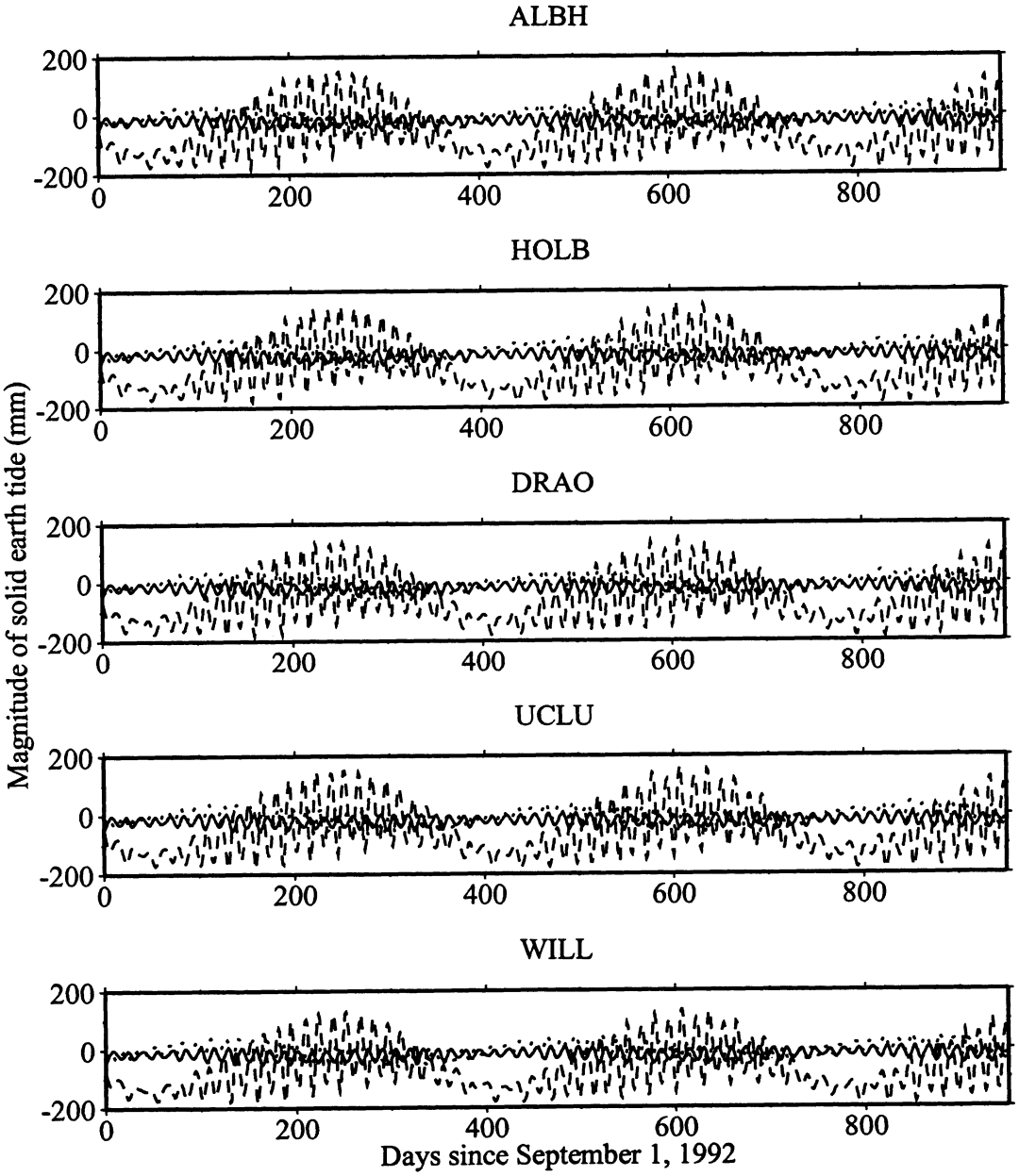

Figure 4.3: Long-term solid Earth tide effects at each of the WCDA sites. The solid line denotes the north component, the dotted line the east component, and the dashed line the upward component.

(N-E-U) topocentric coordinate system,

$$\Delta_{sol} = \sum_j [l_2 d_{N,j}, l_2 d_{E,j}, h_2 d_{U,j}]^T \tag{4.9}$$

where j represents the tide-producing celestial body (1 for Sun and 2 for Moon) and

$$d_{N,j} = \frac{3GM_j r^2}{2gR_j^3}[sin2\psi(sin^2\delta_j - cos^2\delta_j cos^2 H_j) + sin^2 2\delta_j cos H_j cos2\psi]k_j^3 \tag{4.10}$$

$$d_{E,j} = \frac{3GM_j r^2}{2gR_j^3 cos\psi}(2cos^2\psi cos^2\delta_j sin H_j + \frac{1}{2}sin2\psi(sin^2\delta_j sin H_j)k_j^3 \tag{4.11}$$

$$d_{U,j} = \frac{3GM_j r^2}{4gR_j^3}(cos2z_j + \frac{1}{3})k_j^3 \tag{4.12}$$

where G is Newton's universal constant, g is the magnitude of gravity, r is the equatorial radius of the Earth, ψ is the geographic latitude; M_j, z_j, δ_j, H_j are the mass, the apparent zenith distance, the declination, and the hour angle of the celestial body respectively, R_j is the mean distance between the Earth and the celestial body, k_j is the ratio of R_j to the apparent distance of the celestial body from the Earth. The ephemerides of the Sun and the Moon are calculated according to Pagiatakis [1982].

The solid Earth tides corrections due to both the Sun and the Moon are included in CGPS22 according to the above equations. The typical peak-to-peak amplitude of this correction for the WCDA can be as large as 40 cm in the vertical component and several cm in the horizontal components, but the horizontal gradient of this displacement is small. **Figure 4.2** shows the daily displacement due to solid Earth tides on April 1, 1995 for each of the WCDA stations, and **Figure 4.3** shows its long-term variation from September 1, 1992 to April 5, 1995 (one sample per day at the same UT epoch).

4.3.5 Ocean Tide Loading Displacement

The **ocean tide loading** is the elastic response of the Earth's crust to ocean tides and it is one of the secondary tidal effects. The ocean tide loading is a rather complicated phenomenon related to the rheology of the Earth and the local geology, and thus mathematically it is not well modelled by far.

The present model in CGPS22 is described by Pagiatakis [1982]. The tidal displacement vector expressed in the N-E-U topocentric coordinate system at time t is

$$\Delta_{ocn} = [d_1, d_2, d_3]^T \tag{4.13}$$

where

$$d_j = \sum_{i=1}^{N} \epsilon_i^j cos(\omega_i t + V_i - \delta_i^j) \tag{4.14}$$

where N is the number of the tidal constituents, ω_i and V_i are the frequency and astronomical argument of tidal constituent i, and ϵ_i^j and δ_i^j are the amplitude and Greenwich phase lag of tidal constituent i and coordinate component j respectively. ω_i and V_i can be determined from the solar and lunar ephemeris information. The origin of time t depends on the time epoch of ω_i and V_i. The tidal amplitudes and Greenwich phase lags are independent of time origin. They are determined based on an elasitc Earth model and a global ocean tide model (typically $1° \times 1°$ resolution) supplemented with a higher resolution numerical tide model for some local effects. Six tidal constituents are included in the present model ($N = 6$): three semi-diurnal tides M_2, S_2, N_2 and three diurnal tides K_1, O_1, P_1.

The displacements due to ocean tide loading are typically at the several centimetres level in the vertical component and at the sub-centimetre level in the horizontal

components. However, unlike the solid Earth tides effect, the ocean tide loading can have large spatial variations, especially in coastal regions. Moreover, the errors of the present ocean tide loading model can be as large as 10% or even 20% of the ocean tide loading amplitudes [Baker et al., 1995]. **Figure 4.4** shows the daily displacement according to equation (4.13) for each of the WCDA stations, and **Figure 4.5** shows the long-term variation from September 1, 1992 to April 5, 1995 (one sample per day at the same UT epoch). It is evident in both figures that the amplitude and phase of the ocean tide loading effects have large spatial variations among the WCDA stations.

4.3.6 Pole Tide Displacement

Polar motion is the motion of the Earth's spin axis relative to the Earth's crust. It has two major periodic constituents: the annual and the Chandler (about 430 days) periods. The polar motion induces a deformation of the Earth through changes of the centrifugal potential. This effect is called the **pole tide**. Depending on geographic location, the maximum displacement due to pole tide is 1 to 2 cm in the vertical component and a few mm in the horizontal components.

The present model was derived by Yoder [Sovers and Border, 1987]. Expressed in the N-E-U topocentric coordinate system, the displacement of a point at latitude ψ, longitude λ due to pole tide is

$$\Delta_{ocn} = [d_1, d_2, d_3]^T \tag{4.15}$$

where

$$d_1 = -\frac{\omega_E^2 r}{g} cos2\psi(xcos\lambda + ysin\lambda)l_2 \tag{4.16}$$

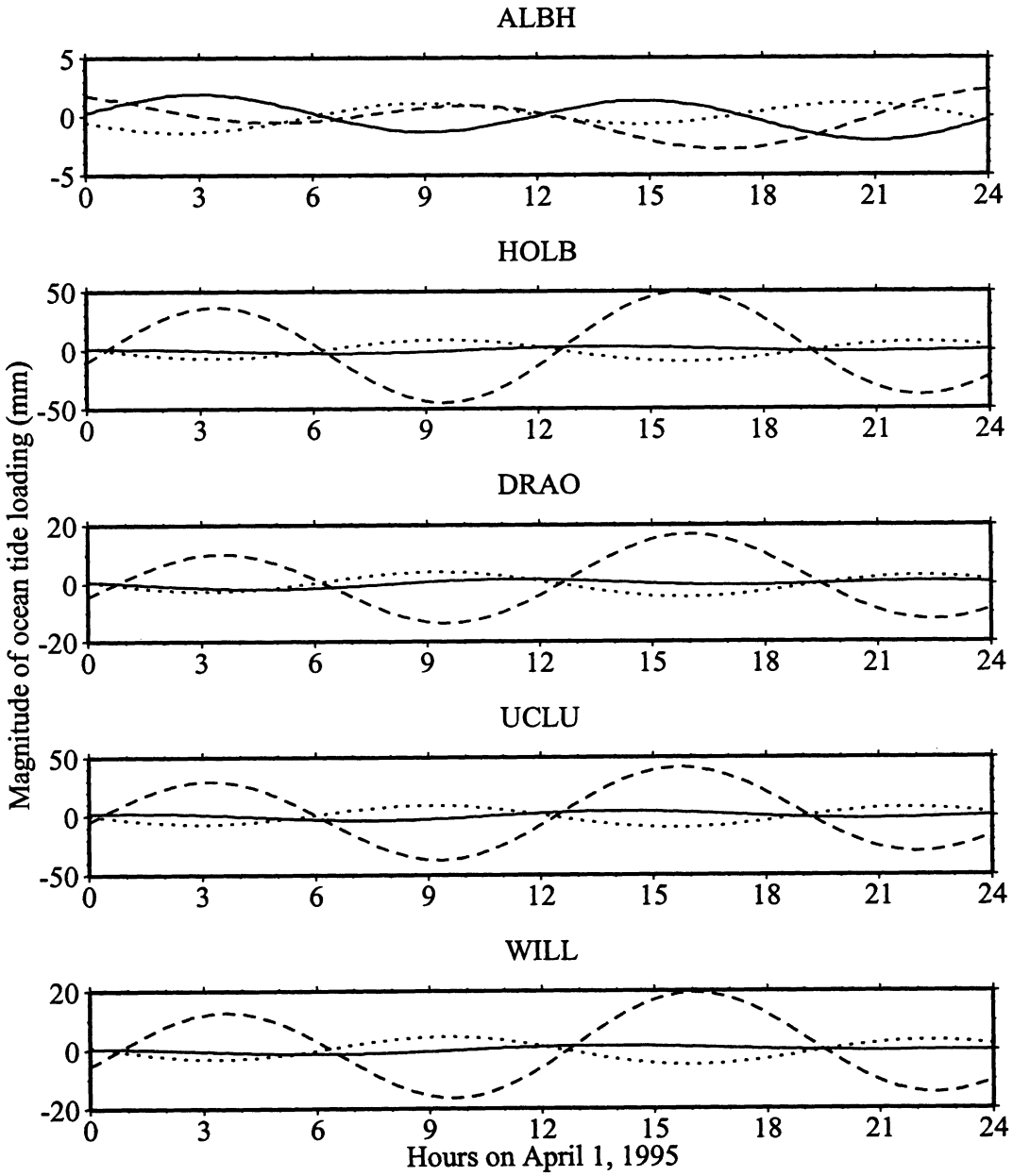

Figure 4.4: Daily ocean tide loading effects at each of the WCDA sites. The solid line denotes the north component, the dotted line the east component, and the dashed line the upward component.

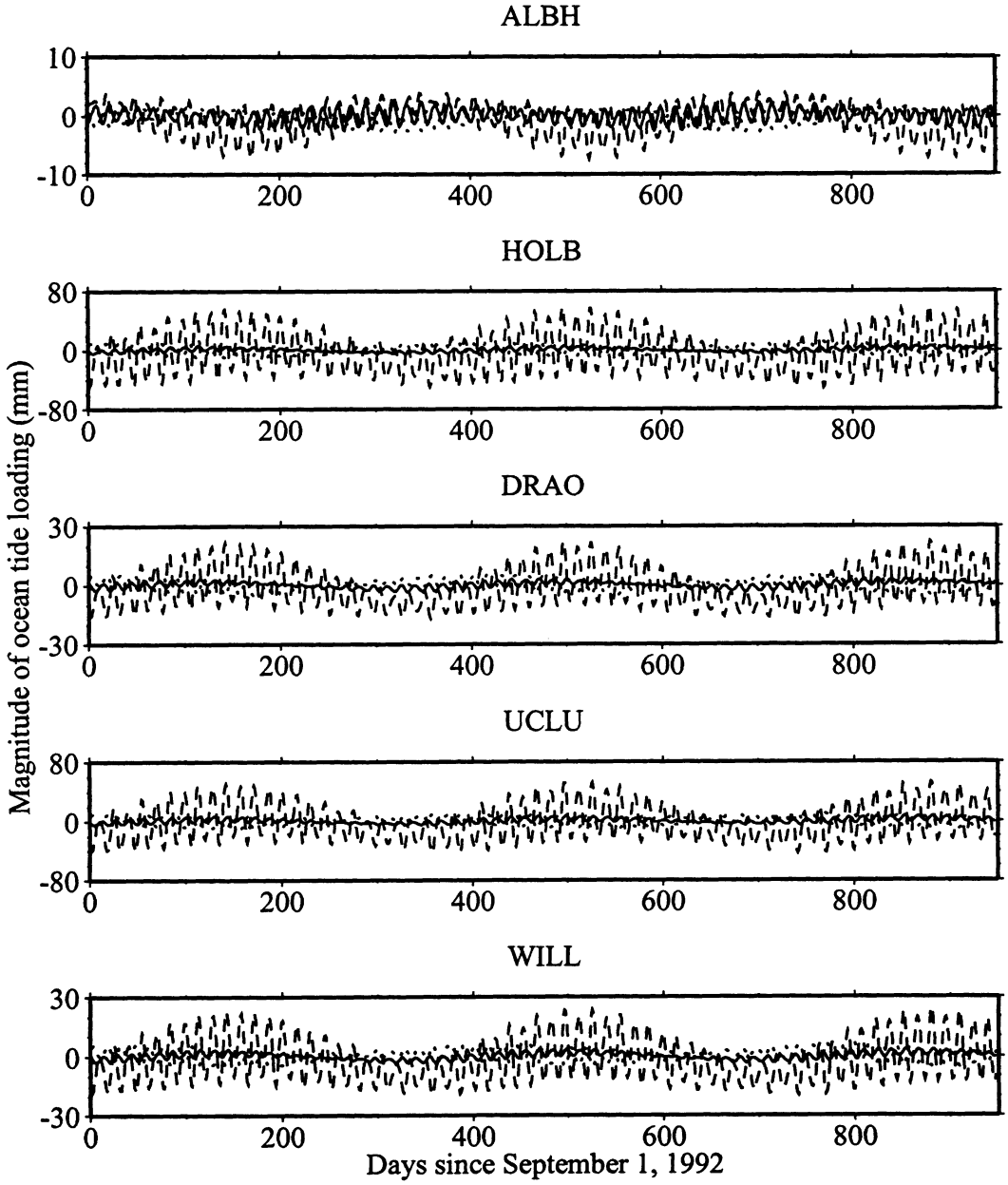

Figure 4.5: Long-term ocean tide loading effects at each of the WCDA sites. The solid line denotes the north component, the dotted line the east component, and the dashed line the upward component.

$$d_2 = -\frac{\omega_E^2 r}{g} sin\psi(-xsin\lambda + ycos\lambda)l_2 \quad (4.17)$$

$$d_3 = -\frac{\omega_E^2 r}{g} sin\psi cos\psi(xcos\lambda + ysin\lambda)h_2 \quad (4.18)$$

Here ω_E is the rotation rate of the Earth, r is the equatorial radius of the Earth, g is the magnitude of the Earth's surface gravity, and h_2 and l_2 are the first Love number and Shida's number. x and y are the pole coordinates with respect to the 1903.0 CIO pole position.

The daily variation of pole tide displacement for the WCDA sites is negligible. **Figure 4.6** shows the long-term variation of the displacement from September 1, 1992 to April 5, 1995 (one sample per day at the same UT epoch) for each of the WCDA sites. The pole coordinates are from the NRCan EOP products.

4.3.7 Tropospheric Delay

The term **tropospheric delay** is actually used to designate the global effect of the neutral atmosphere, which is essentially a non-dispersive medium at radio frequencies, i.e., the effects on GPS measurements are independent of the signal frequencies [Mendes and Langley, 1994]. It reaches about 1.9 - 2.5 m in the local zenith direction and increases approximately with the cosecant of the elevation angle, yielding about a 20 - 28 m delay at a 5° elevation angle [Leick, 1995].

The tropospheric delay is usually separated into hydrostatic or '**dry**' and non-hydrostatic or '**wet**' components. The dry term is the contribution of the dry air which accounts for about 90% of the total delay. Since it typically varies slowly and smoothly, it can be accurately modelled to 1 cm or better at zenith using surface

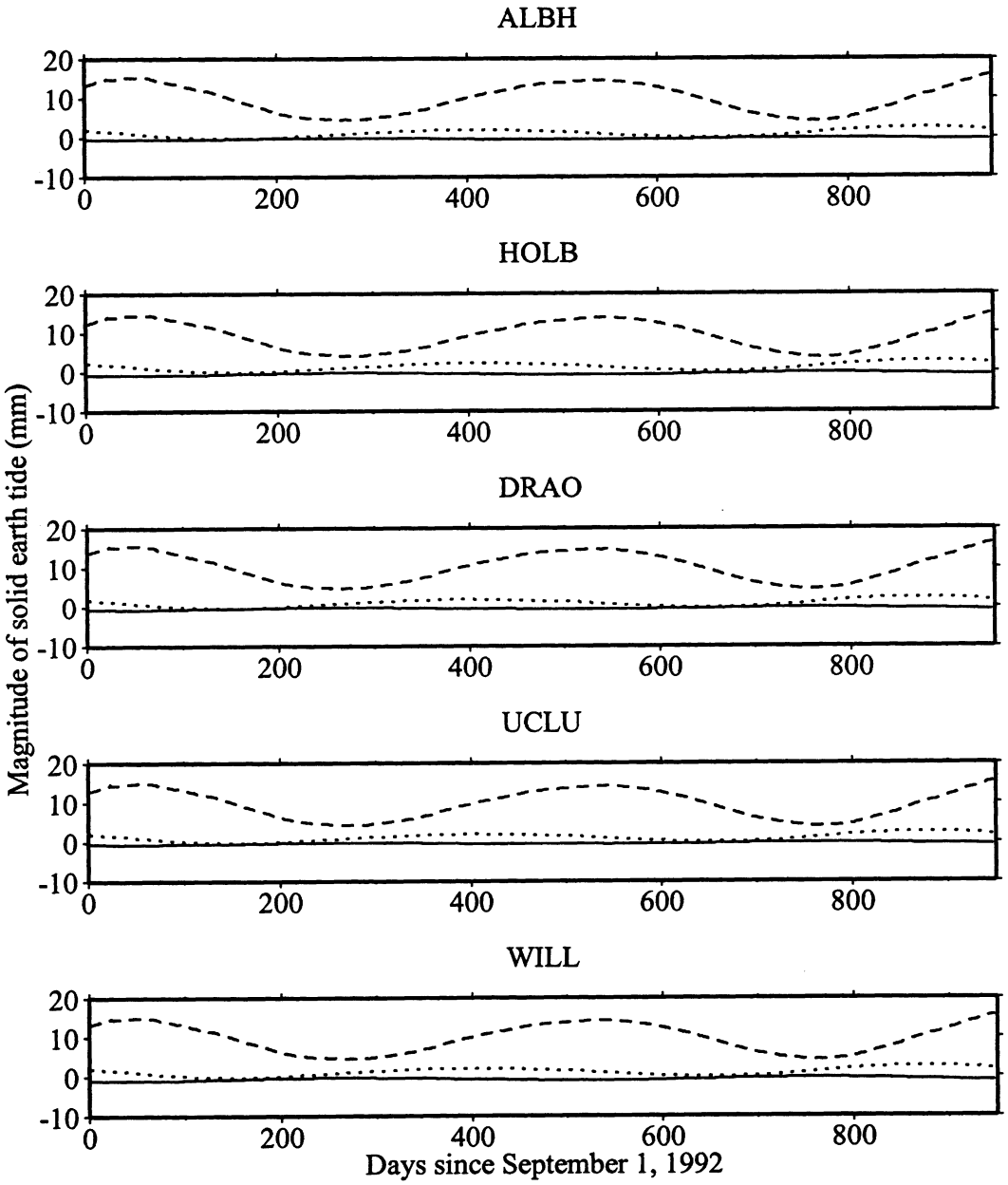

Figure 4.6: Long-term pole tide effects at each of the WCDA sites. The solid line denotes the north component, the dotted line the east component, and the dashed line the upward component.

meterological (**SM**) measurements [Yunck, 1993]. The wet term is the contribution of the water vapor content. Although the wet component only makes up about 10% of the total delay on average, it is poorly modelled at present because the water vapor is not well mixed in the atmosphere and varies randomly over a broad spatial and temporal scale due to atmospheric turbulence. Therefore the water vapor content is not well correlated with the ground-based SM measurements [Thompson et al., 1986]. As a result, instead of the true SM measurements, the extropolated standard SM data based on the standard atmospheric condition for the region of interest and the assumed vertical gradient of temperature are often used in GPS data processing. There are suggestions that these standard data can sometimes provide a better calibration than the true SM measurements [Tralli and Lichten, 1990].

The total tropospheric delay at elevation angle E is usually expresseded as

$$d_{trop} = d^z_{dry} \cdot m_{dry}(E) + d^z_{wet} \cdot m_{wet}(E) \tag{4.19}$$

where d^z_{dry} and d^z_{wet} are the dry and wet delays in the zenith direction, $m_{dry}(E)$ and $m_{wet}(E)$ are the **mapping functions** corresponding to the dry and wet delays respectively. In CGPS22, the tropospheric zenith delay is calculated using either the Hopfield model [Hopfield, 1969; 1971] or the Saastamoinen model [Saastamoinen, 1973], and the mapping function can optionally be Black's model [Black, 1978], Herring's model [Herring, 1992] or Niell's model [Niell, 1996]. With these models, the wet zenith delay can be calculated with an accuracy of about 10 - 20%, corresponding to a standard deviation of 3 to 5 cm [Leick, 1995].

Since the tropospheric delay, especially the wet component, cannot be satisfactorily calibrated with any of the existing models, it has to be parameterized and estimated in GPS data reduction for high-precision geodetic applications. A simple method is to introduce a **tropospheric scale parameter** which can be defined by

the following equation

$$d_{trop} = (1 + s_{trop}) d_{0,trop} \tag{4.20}$$

where $d_{0,trop}$ is the computed or predicted tropospheric delay according to the models and s_{trop} is the scale parameter to be estimated (in the unit of %). There are a number of estimation strategies for these local tropospheric scale parameters in terms of their assumed statistics. They can be modelled as random variables or stochastic processes and there could be more than one parameter for each station during the observation period. The stochastic model of the tropospheric parameters used in the CGPS22 is discussed in the next subsection.

4.3.8 Stochastic Modelling of Tropospheric Parameters

Since tropospheric delay varies randomly with time and space, its statistics cannot be well represented by a single random variable with invariant statistics (called **random constant**). In fact, the irregular variations of the tropospheric delay reflect the random temporal and spatial variations of multiple factors such as the water vapor content, pressure and temperature. A better approach to approximate the tropospheric delay is by Kolmogorov turbulence theory, in which the tropospheric delay can be regarded as realizations of certain **random fields** - random functions of time and space [Treuhaft and Lanyi, 1987; Yaglom, 1987]. A **random function** is an ensemble of an infinite number of random variables. Thus, a random field can better describe the complexity of the tropospheric delay.

In order to simplify the problem, two basic assumptions are made. First, the random field for the tropospheric delay is taken to be homogeneous and **isotropic**, i.e., the correlation function $R(\vec{\varrho}_1, \vec{\varrho}_2)$ of the random field $X(\vec{\varrho}), \vec{\varrho} \in \Re^n$ is independent

of the origin as well as the direction of the increment vector $\vec{d} = \vec{\varrho}_2 - \vec{\varrho}_1$, namely $R(\vec{\varrho}_1, \vec{\varrho}_2) = R(d)$. Second, the temporal stochastic (or random) process in the random field must be **stationary**, ergordic, and Gaussian-distributed. Here, stationary means that the mean value of the process must be a constant and its correlation function depends only on the time increment. Ergordic means that the time average of a single realization of the stochastic process equals to the ensemble average. It should be noted that these two assunptions are different from the original two assumptions in Kolmogorov turbulence theory. The original assumptions require that the random field for tropospheric delay be locally homogenous and isotropic in space domain and have a stationary increment process in time domain. Our approach is a simplification from the Kolmogorov theory.

An exponentially correlated random field, in which correlation decays with both time and space, is empirically assumed for the tropospheric delay. The correlation function is defined as

$$R(\tau, d) = \sigma_0^2 \cdot e^{-\sqrt{(\tau/T)^2+(d/D)^2}} \tag{4.21}$$

$$\approx \sigma_0^2 \cdot e^{-(\tau/T+d/D)} \qquad (\texttt{when } \tau/T \ll d/D \texttt{ or } d/D \ll \tau/T) \tag{4.22}$$

where τ and d are the increments in time domain and space domain respectively, T is a constant called the correlation time, D is the correlation distance, and σ_0 is the steady state sigma of the random field. Yaglom [1987] has proven that equations (4.21) and (4.22) are isotropic correlation functions and they are also stationary in the time domain when $d = 0$. The random process defined by equation (4.22) in the time domain is called **colored noise** or first order Gauss-Markov process.

It must be emphasized that equation (4.21) is an empirical model since the actual physical nature of the troposphere is not involved. The choice of the exponential function is based on both mathematical simplicity and the fact that it reasonablly

approximates reality. For example, Treuhaft and Lanyi [1987] showed that according to Kolmogorov turbulence theory the wet tropospheric delay has a structure function (the correlation function of the increment field $X(\vec{\varrho}+\vec{d})-X(\vec{\varrho})$) proportional to $d^{5/3}$ when d is only a few kilometres or less and to $d^{2/3}$ when d is greater than a few tens of kilometres. The former structure function, in fact, defines a fractal random walk (also called fractal Brownian motion) of fractal dimension $d_f = 7/6$ and the latter structure function defines a fractal white noise of fractal dimension $d_f = 5/3$ [Yaglom, 1987 and Mandelbrot 1982]. In spite of having somewhat different statistical properties from the fractal random fields, the classical random walk and white noise (structure functions are proportional to d^1 and d^0 respectively) render a good approximation to the fractal random fields, especially when the spatial or temporal span is not too large. The advantage of the exponentially correlated random field is that it resembles a classical random walk when d is small and a classical white noise when d is large, as illustrated in **Figure 4.7** with their structure functions. Moreover, the exponentially

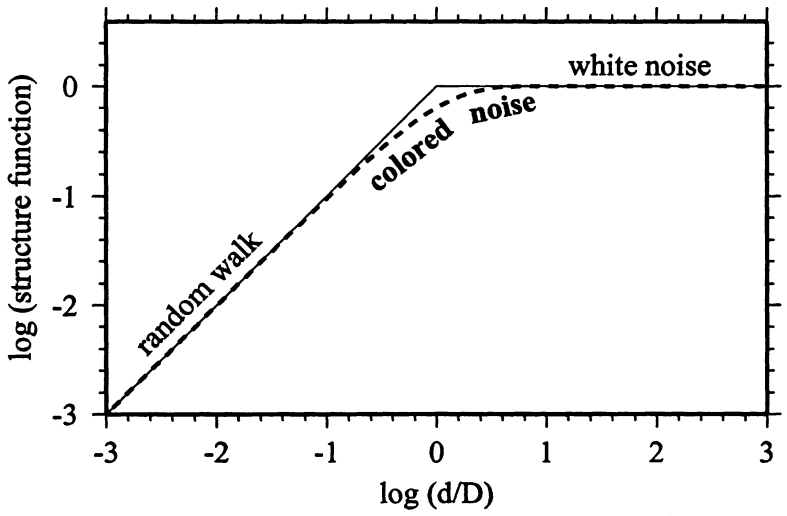

Figure 4.7: Structure functions of random walk, white noise, and colored noise.

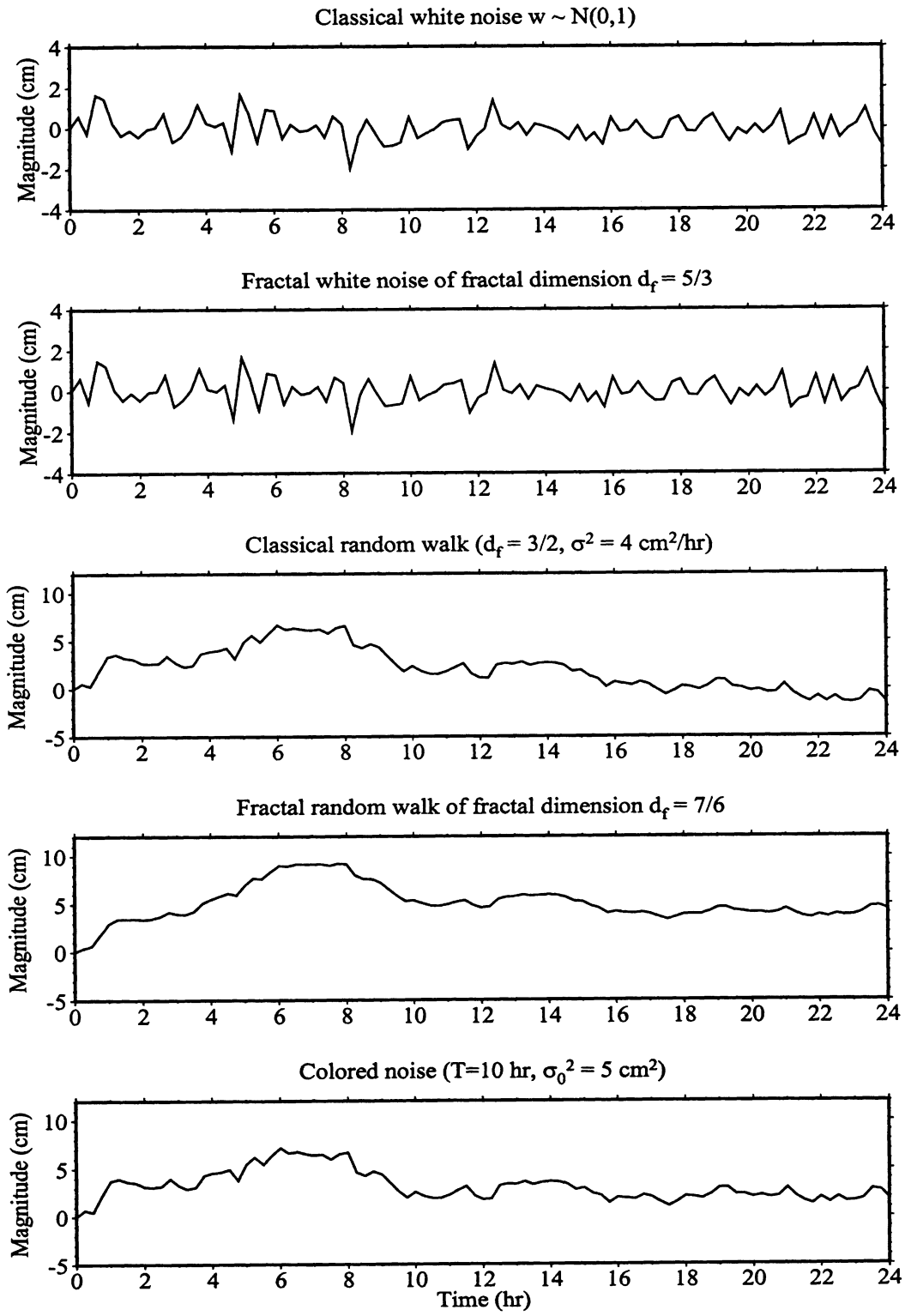

Figure 4.8: Different simulated stochastic processes (sample interval = 15 minutes).

correlated random field decorrelates when $\tau = \infty$ or $d = \infty$, while the Kolmogorov random field does not which is unphysical. To illustrate the similarity between the different random processes, **Figure 4.8** shows simulated random functions in time domain including classical white noise with normal distribution N(0, 1 cm), fractal white noise ($d_f = 3/5$), classical random walk ($\sigma = 2cm/\sqrt{hr}$, fractal random walk ($d_f = 7/6$), and exponentially correlated colored noise ($T = 10hr$, $\sigma_0 = \sqrt{5}cm$). The time span in the simulation is 24 hours with a 15 minute sample interval (equivalent to the batch length used in parameter estimation for WCDA daily data reduction). The simulated colored noise has a 10 hr correlation time. It is shown that within a day the fractal random walk, classical random walk, and colored noise bear great similarity. So do the classical white noise and fractal white noise. The similarity among the fractal random walk, classical random walk, and colored noise decreases as time span increases.

A closer inspection of equation (4.21) reveals some important implications embedded in the equation. For instance, τ and d can be viewed as two orthogonal components of a joint time-space vector. The temporal correlation and the spatial correlation are completely interchangable. That is to say, the temporal variation of the troposphere at one site ($d = 0, \tau > 0$) can be considered equivalent to the spatial variation of the troposphere between two sites at the same moment ($\tau = 0, d > 0$). This characteristic corresponds to a "frozen" tropospheric structure driven by wind at a speed of D/T (though the correlation is independent of the wind direction). The Kolmogorov random field has the same characteristic [Treuhaft and Lanyi, 1987]. The interchangability between the temporal and spatial correlations is justified in Kolmogorov random field because in reality the two types of correlations are basically due to the same causes in a local scale [Tatarskii, 1961]. In our approach, this concept is extended to a larger scale, as implied in the two assumptions made at the

beginning of this subsection.

The correlation distance D for wet tropospheric delay can be determined empirically from [Treuhaft and Lanyi, 1987]. We chose $D_{wet} = 30$ km, which is approximately where the spatial structure function shows the feature of a fractal white noise. Due to its more uniform spatial distribution, the dry tropospheric delay has a much larger correlation distance. Treuhaft and Lanyi [1987] suggested $D_{dry} = 4D_{wet}$. Thus $D_{dry} = 120$ km is chosen in CGPS22.

The correlation time T depends on the average wind speed for the region. As this data is not available, we chose to run solutions for the WCDA for a number of days with a few different values for T ranging from 1 to 12 hours, and the value that produced the best repeatability is assigned to T. In this way, we obtained $T = 10$ hours, which corresponds to a very slow wind speed of 3 km/hr. Meanwhile, for the WCDA, as spatial increment $d > 30$ km and temporal increment $\tau \ll 10$ hr, the approximation in equation (4.22) is therefore valid in our case.

The tropospheric delay parameters modelled as random fields defined by equation (4.22) can be estimated along with other parameters using a Kalman filtering algorithm, in which temporal and/or spatial correlations of the parameters are described with a discrete stochastic model and a statistical model. The complete model description and execution procedure of a Kalman filtering algorithm used in CGPS22 is introduced in the next subsection.

In discrete form, the stochastic process $p(t)$ defined by equation (4.22), namely the first order Gauss-Markov process, is expressed as

$$p_{k+1} = e^{-(t_{k+1}-t_k)/T} \cdot p_k + w_k \tag{4.23}$$

where $p_k = p(t_k)$, k denotes the kth time epoch, T is the correlation time of $p(t)$, and w_k is a white noise sequence. Accordingly, the transition coefficient for this tropospheric parameter is $e^{-(t_{k+1}-t_k)/T}$.

The covariance matrix Q_k in statistical model (4.29) of the Kalman filtering algorithm can take into account both the temporal and spatial correlations of tropospheric parameters. The diagonal term of Q_k for the ith tropospheric parameter at the kth time epoch, denoted by $q_{i,k}$, corresponds to the temporal correlation only (because $d = 0$), and the off-diagonal term $q_{ij,k}$ between the ith and the jth tropospheric parameters at the kth time epoch is caused by the spatial correlation. The two terms are calculated as

$$q_{i,k} = \sigma_{0,i}^2 \cdot (1 - e^{-2(t_k - t_{k-1})/T_i}) \tag{4.24}$$

$$q_{ij,k} = \sqrt{q_{i,k} \cdot q_{j,k}} \cdot \frac{1}{2}(e^{-d_{ij}/D_{wet}} + e^{-d_{ij}/D_{dry}}) \tag{4.25}$$

where $\sigma_{0,i}$ and T_i are the steady state sigma and the correlation time of the ith tropospheric parameter respectively, and d_{ij} is the distance between stations i and j. It should be noted that equation (4.25) is for the case where the total tropospheric delay is estimated. If only the wet tropospheric delay is estimated, the spatial correlation term in equation (4.25) should be modified accordingly ($e^{-d_{ij}/D_{wet}}$).

The above equations developed for exponentially correlated random fields can actually be extended to other types of random fields. If correlation time T and correlation distance D are both zero, it is a classical white noise model. The transition coefficient is zero. The variance term $q_{i,k}$ is σ_0^2 and covariance terms $q_{ij,k}$ are zero. From equation (4.37), this implies that the variance term of the white noise parameter in the predicted covariance matrix P^- is reset to σ_0^2 and all covariance terms of the parameter are reset to zero, and that the predicted estimate of the parameter is also reset to zero.

In the case of random walk, both T and D are infinity. This random field is in fact neither isotropic nor stationary. Steady state is never reached (σ_0 does not exist). The transition coefficient equals one and the $q_{i,k}$ term is defined by a constant increment at each time interval, i.e.,

$$q_{i,k} = \dot{q}_i \cdot (t_k - t_{k-1}) \tag{4.26}$$

where $\dot{q}_i$ is the rate of change of the process noise covariance. Since random walk is only locally isotropic, the spatial correlation is usually ignored in a scale larger than local, i.e., $q_{ij,k} = 0$. In a local scale, the spatial correlation is one. One parameter is enough for the whole local region in which isotropic property can hold.

It should be mentioned that the above spatial correlation model (equation (4.25)) has not been tested with experimental data. Hence the performance of the spatial correlation model needs to be verified in the future.

4.3.9 Batch Sequential Least Squares Adjustment

CGPS22 uses the batch sequential least squares adjustment (**BSLSA**) for parameter estimation. In this algorithm, the whole observation time interval is divided into many small equal intervals with user-defined length, called **batches**. The length of the batches is always longer than that of the sample intervals, and is determined by the nature of the stochastic processes used for the modelling of the tropospheric delays. It should be small enough so that sufficient resolution is obtained for the stochastic processes. Empirically, 15 to 30 minutes is the appropriate range for the batch length in dealing with the stochastic tropospheric parameters. Consequently for the batch sequential algorithm the processing unit is a batch instead of an epoch. Within a batch, the stochastic parameters are actually piecewise constants. Only at

the end of a batch do the statistical properties of a stochastic process come into play.

For a deterministic system which CGPS22 is designated to deal with, the BSLSA, as a matter of fact, has no difference in form from the Bayes filter (or the Kalman filter in Bayes form). The name BSLSA for CGPS22 has been kept partly because of historical reason and partly because there are no dynamics involved in the adjustment as is usually the case in a filtering problem. Therefore, the algorithm of BSLSA given below is the same in form as that of the Bayes filter, though the batch processing scheme is addressed compared to the scalar or epoch processing usually encountered in a filtering situation.

There are three models (in linearized form) involved in the BSLSA:

$$\bullet\ \textit{Stochastic model} \ : \ p_{k+1} = \phi_k p_k + w_k \tag{4.27}$$

$$\bullet\ \textit{Measurement model} \ : \ z_{k+1} = H_{x,k} x_k + H_{p,k} p_k + v_k \tag{4.28}$$

$$\bullet\ \textit{Statistical model} \ : \ E(w_k) = 0, \quad E(w_k w_i^T) = Q_k \delta_{ik} \tag{4.29}$$

$$E(v_k) = 0, \quad E(v_k v_i^T) = R_k \delta_{ik} \tag{4.30}$$

$$E(w_k v_i^T) = 0 \tag{4.31}$$

where p_k is an $m_1 \times 1$ stochastic parameter vector (typically including tropospheric parameters) at time t_k, ϕ_k is the $m_1 \times m_1$ transition matrix, w_k is the $m_1 \times 1$ system driving noise assumed to be white Gausian sequence with known covariance matrix Q_k, x_k is an $m_2 \times 1$ constant parameter vector (typically including station coordinates and phase ambiguities), z_k is the $n \times 1$ measurement vector at time t_k, $H_{x,k}$ is $n \times m_2$ design matrix for constant parameters x_k, $H_{p,k}$ is $n \times m_1$ design matrix for stochastic parameters p_k, v_k is $n \times 1$ measurement noise assumed to be white Gausian sequence with known covariance R_k, E denotes the mathematical expectation operator, and δ_{ik} is the Kronecker delta ($\delta_{ik} = 1$ if $i = k$ and $\delta_{ik} = 0$ if $i \neq k$).

The batch sequential algorithm forms a recursive loop as summarized in the following. The superscript "-" denotes the predicted or *a priori* quantities and the hat "^" denotes the estimated quantities.

1. initialize the loop with the batch number $j = 1$, the given *a priori* estimate vector $\hat{y}_j^- = [\hat{x}_j^- \ \hat{p}_j^-]^T$ and its error covariance matrix P_j^-.

2. accumulate the normal equation $N_j\hat{y}_j + U_j = 0$ for the jth batch according to

$$N_j = (P_j^-)^{-1} + \sum_{k=1}^{l} H_k^T R_k^{-1} H_k \tag{4.32}$$

$$U_j = \sum_{k=1}^{l} H_k^T R_k^{-1}(z_k - H_k\hat{y}_j^-) \tag{4.33}$$

where $H_k = [H_{x,k} \ H_{p,k}]$, l is the number of epochs in the jth batch.

3. solve the normal equation and obtain the updated estimate,

$$P_j = N_j^{-1} \tag{4.34}$$

$$\hat{y}_j = \hat{y}_j^- + N_j^{-1} \cdot U_j \tag{4.35}$$

4. update the *a priori* estimate $\hat{y}_{j+1}^-$ and its error covariance P_{j+1}^- for the next batch $j + 1$,

$$\hat{y}_{j+1}^- = F_j\hat{y}_j \tag{4.36}$$

$$P_{j+1}^- = F_j P_j F_j^T + Q_j \tag{4.37}$$

where $F_j = \begin{bmatrix} I & 0 \\ 0 & \phi_j \end{bmatrix}$.

5. $j = j + 1$; if $j \leq$ the total number of batches, then go to step 2, otherwise stop the loop.

It should be noted that the statistical properties of the stochastic parameters are incorporated into the adjustment in step 4. Q_j adds noise to the process at the end

of each batch, in accordance with the stochastic model (4.27).

4.3.10 Measurement Weighting Scheme

A weighting scheme for both the pseudoranges and carrier phases has been developed according to Euler and Goad [1991], Kouba and Chen [1992], and Kouba et al. [1993]. It properly down-weights the obseravations at lower elevation angles which usually have lower signal-to-noise ratio. Meanwhile, when both phases and pseudoranges are used in the adjustment, it also properly down-weights the pseudoranges. The weighting scheme is based on an exponential function of the satellite elevation angle and the observation noise factors σ_0 which are pre-estimated for pseudoranges during the combined pre-processing stage as a constant for each station and empirically determined for the carrier phases. That is,

$$\sigma(E) \;=\; \sigma_0 + \sigma_1 e^{-(E/E_0)} \tag{4.38}$$

where σ_1 is the scale factor of an elevation-angle-dependent term, E is the elevation angle in degrees and E_0 is a constant. Both E_0 and σ_1 are empirically determined [Euler and Goad, 1991], and the latter are different for pseudoranges and for carrier phases.

By this weighting scheme, some physical correlations in the measurements are reduced to a certain degree. Therefore a better precision of the station coordinates should result from the weighted adjustment if the weights are chosen properly. In a test run, the sigmas were set to be $\sigma_0 = 7$ mm, $\sigma_1 = 25$ mm, and $E_0 = 20°$ for 2 minute sampled carrier phases (pseudoranges were not included). Seven days of data in GPS week 794 were processed using two schemes: one with carrier phase weighting and the other without. **Table 4.1** summarizes the repeatabilities in North

(N), East (E), and Upward (U) baseline components and baseline length (L), with and without carrier phase weighting. As can be seen, most baseline components show

Table 4.1: Repeatabilities with and without carrier phase weighting (mm). N denotes north component, E is east component, U is upward component, and L is baseline length.

	with weighting				without weighting			
	N	E	U	L	N	E	U	L
ALBH-DRAO	2.0	1.9	6.9	1.9	2.1	2.1	7.0	2.2
HOLB-DRAO	1.3	2.5	4.1	2.4	1.3	2.6	4.2	2.5
WILL-DRAO	1.3	2.6	2.1	2.1	1.3	2.6	1.8	2.0
UCLU-DRAO	0.9	2.1	5.7	2.1	1.0	2.3	5.9	2.4

slight improvements in repeatabilities. The somewhat worse repeatability for the upward component of the WILL-DRAO baseline may indicate that for this particular baseline the sigmas were not quite appropriate. For this reason, it might be better if the sigmas are chosen differently for different baselines according to their physical environments.

4.4 Main-processing of GPS Data

Depending on the purpose and interests of the user, the main-processing of GPS data with CGPS22 may take different options, as illustrated in Figure 4.1 by the shadowed blocks. In this section, the implementation aspects of the CGPS22 main processor and some options are introduced.

In the CGPS22 main processor (GPS22), the batch sequential least squares adjustment is implemented using double-differenced carrier phases and/or properly down-weighted pseudoranges. The parameters that can be estimated include: non-fixed station coordinates, station clock biases, initial carrier phase ambiguities, local tropospheric delays, and initial Kepler satellite orbital elements.

The measurements in the adjustment can be any of the double-differenced carrier phases (φ_1, φ_2, ionosphere-free combination φ_3) and pseudoranges (P_1, P_2, ionosphere-free combination P_3), or both carrier phases and pseudoranges.

The output files from the CGPS22 main processor include the summary file, residual file, clock file, and $GEOLAB^{TM}$ G-file. The summary file contains all input and adjustment information such as the adjusted parameters, the data statistics, and complete covariance matrix, etc. The residual file contains the *a posteriori* residual time series, which is critical for visual quality check. The clock file contains the clock residual time series after the corrections for satellite and receiver clocks are applied. The G-file is in the format specified by $GEOLAB^{TM}$ software and can be used to perform a multi-session readjustment of the GPS network.

To resolve the carrier phase initial ambiguities, the program CYCOMP, as shown in Figure 4.1, can be used. It is based on a simple algorithm searching through the solved $\varphi_1, \varphi_2, \varphi_3$, and wide-lane combination ($\varphi_4 = \varphi_1 - \varphi_2$) ambiguities. It needs to be run recursively to gradually resolve as many ambiguities as possible. This procedure is far from automatic and needs tedious work and expertise.

The module MPT in Figure 4.1 is designed to remove multipath effects from the carrier phase measurements. There have been two methods developed to extract the multipath signatures from the *a posteriori* residuals. Both methods make use of the

fact that the multipath signatures repeat from day to day with an approximately four minute time advance. The first method, or stacking method, simply averages phase residuals properly aligned from day to day for a period long enough to isolate the multipath signals (typically about one week) [Kouba and Chen, 1992]. The second method, or spectral method, uses a multi-channel spectral estimator to obtain the coherence and phase lag (or advance) spectra of the carrier phase residuals on two different days. By picking the significant frequency constituents corresponding to the *a priori* known phase lag and implementing the inverse Fourier transform, the multipath time series can be recovered. After the multipath signatures have been isolated, they can be fed into the adjustment and removed from the carrier phase measurements. However, it must be noted that the performance of the two methods relies on the assumption that the daily repeated signatures be solely caused by the multipath. If such not being the case, the performance of the two methods would degrade and even make harm to the solutions.

4.5 Control and Auxiliary Software

The control software is written in Unix shell scripts and is designed to streamline and automate the daily GPS reduction by CGPS22. The shell programs were developed jointly by the author and Ms. Y. Lu at PGC.

The auxiliary software includes three types of programs as briefly summarized in the following:

- display programs - make use of the PGPLOT drawing subroutine package to display all kinds of data files.

- statistics programs - calculate statistics from the solutions.
- supplementary programs - implement some optional functions, e.g., ORBCOM and ORBFIT in Figure 4.1 for orbit comparison and polynomial fit, and CHKDIF for zero-baseline data analysis.

4.6 Chapter Summary

Various aspects of the GPS software package CGPS22 have been introduced in this chapter with emphasis on the measurement models in the main-processor. CGPS22 uses the double-differencing technique and both carrier phase and pseudorange observables. The capability of CGPS22 in cycle slip editing has been improved and enabled a higher degree of automation in daily data reduction. The selected measurement models in the main-processor aim at a millimetre level positioning precision in a regional scale. The stochastic modelling of the tropospheric delay can take both temporal and spatial correlations into account. A measurement weighting scheme based on an exponential function of the satellite elevation angle has been incorporated and tested with seven days of WCDA data. The solutions with the weighting scheme show a small but consistent precision improvement of up to 0.2 mm. Efforts have been made on multipath removal using spectral estimation technique. However, the tests with WCDA data resulted no encouraging improvement on solutions.

Since this chapter serves for a general purpose, the models introduced are not specific to the WCDA data analysis. Some of the models have in fact been disabled in the regular WCDA data reduction. Thus, it is in order now to give the details of estimation strategy used for the WCDA data reduction and the corresponding error

budget in the next chapter.

Chapter 5

Estimation Strategy and Error Budget for WCDA Data Analysis

This chapter is divided into two parts. First, in section 5.1, a specific estimation strategy is presented for the WCDA data reduction in order to achieve high precisions. Various aspects of the estimation strategy are given and explained. Second, based on the estimation strategy, the potential major error sources of the solutions and the level of their influences are discussed in section 5.2.

5.1 Estimation Strategy

The estimation strategy used for the WCDA daily data reduction is listed below:

- Reference station (held fixed): DRAO.
- Stations to be adjusted: all others (ALBH, HOLB, WILL, UCLU).

- Nominal station coordinates: **ITRF91** (International Terrestrial Reference Frame) or well determined from more than two weeks solutions. DRAO coordinates have been changed to **ITRF93** values at epoch 1995.0 (based on ITRF93 velocity field) since February 1, 1994.
- Satellite orbits: NRCan (or IGS) precise orbits in SP3 format, held fixed.
- Satellites used: all available.
- Elevation cutoff angle: 15°.
- Sample interval: 120 seconds.
- Daily data interval: 0^h to 24^h UT.
- Solution type: L_3 carrier phase (pseudoranges not included and ambiguities not fixed).
- Parameters estimated: station coordinates, carrier phase initial ambiguities, local tropospheric scale factors.
- Minimum data gap for introducing new ambiguity parameters : 30 minutes.
- Batch length: 15 minutes.
- Stochastic tropospheric parameters: colored noise, no spatial correlations, correlation time 10 hours, steady state sigma 5% (refer to equation (4.20)).
- Tropospheric modelling: Hopfield model for zenith delay and Black's mapping function.
- Meteorological data: extrapolated with Hopfield model from standard atmosphere at sea level (288 K, 1013.0 mbar, and 50% relative humidity) to the station elevation assuming 6.8 K/km temperature lapse rate.

- Tidal corrections: solid Earth tide, ocean tide loading, and pole tide.

DRAO was selected to be the reference station because it is a well maintained IGS core station and co-located with the VLBI site. Also, it is situated on the North America Plate and at an appropriate distance to the monitored Cascadia subduction zone. In the data reduction, DRAO was held fixed to its ITRF nominal coordinates (ITRF91 before February 1, 1994 at epoch 1991.0 and ITRF93 thereafter at epoch 1995.0). The ITRF nominal coordinates have an accuracy of less than 1 cm as reported in the corresponding ITRF reports. However, the ITRF velocity of DRAO was not considered, which is approximately 2 cm/yr. Therefore, the actual accuracy of DRAO coordinates was up to about 6 cm before Febuary 1, 1994 and was within about 2 cm thereafter. No other stations were held fixed or constrained, as there were no geometrically well configured permanent stations in the region suitable to serve as a fiducial network.

The reference frame for the WCDA solutions is in fact implied in the estimation strategy. It is defined jointly by the fixed NRCan (or IGS) orbits and the fixed reference station DRAO. Optimally, the coordinates of DRAO should be kept in the same ITRF reference frame (with the velocities considered) as the NRCan (or IGS) orbits. In this way, if there are no significant orbital or EOP errors, the WCDA solutions should directly refer to the ITRF reference frame, which is well defined and maintained by the IGS. This processing scheme is based on the concept of the Active Control System (ACS) proposed by Delikaraglou [1989] and not having to estimate satellite orbits greatly relieves the computational burden for the WCDA data analysis. However, in practice, the adopted DRAO coordinates were not always consistent with those used in NRCan orbital computations as DRAO was not held fixed in NRCan solutions and the ITRF velocity for DRAO was overlooked in the WCDA analysis.

This may cause small reference frame misalignment, or small systematic errors in the solutions, and it should be corrected and studied in future WCDA data analysis.

The 24-hour data sets are used with data decimation to increase the data interval from 30 seconds to 120 seconds. This balances the gain from extra redundant data and the loss from unmodelled physical correlation between successively sampled observations. The physical correlation decreases as the sample interval increases. The 24-hour length of session is very important for two main reasons. First, the long observation period provides the maximum redundancy and helps average out the influence of unmodelled systematic errors. Second, as the length of session increases, the benefit from initial cycle ambiguity fixing gets less significant. Hence, in the WCDA solutions, no attempt has been made to fix the initial cycle ambiguities. This approach also reduces the computational burden.

The 15° elevation cutoff angle was chosen as suggested by Yunck [1993]. This choice considers the balance between the benefit from observations at lower elevation angles (more data and stronger geometric observing strength) and errors such as the multipath effects (more significant at lower elevation angles) and tropospheric mismodelling (errors in zenith delay are amplified at lower elevation angles).

When a data gap of more than 30 minutes occurs, it is rather difficult to bridge the phases correctly. Hence, in this case, a new ambiguity parameter will be introduced and the old one can be removed from the normal equation in the least squares adjustment. The same scheme is applied to multiple passes of the same satellite within the whole 24-hour data interval.

The batch length defines how often the solutions are sequentially updated in the batch sequential least squares adjustment. The correlation time and steady state

sigma of the tropospheric parameters are empirically determined for the WCDA data analysis.

Although stations DRAO, ALBH and HOLB (sometimes WILL) have been included in the NRCan orbit determination, none of them is held fixed in the NRCan computation. Besides, a 450-second sample interval is used in the NRCan orbit computation, which is different from the 120-second sample interval used for the WCDA data reductions. These two facts justify the claim that the WCDA data reductions are not simply reproducing or back-substituting into the NRCan solutions.

5.2 Error Budget

This section discusses the potential error sources and their corresponding level of influence on the WCDA solutions. The major error sources, including orbital errors, tropospheric modelling error, and multipath effects, are described in the following three subsections, while the secondary error sources such as antenna phase centre variation are discussed briefly in the last subsection.

5.2.1 Orbital Errors

Since the NRCan (or IGS) precise orbit is held fixed in the WCDA data reduction, the orbital errors are certainly one of the major error sources in the WCDA solutions. There are two possible effects resulting from the NRCan orbital errors. One is the direct effect of the NRCan satellite position error, and the other is the effect due to the error of the NRCan EOP parameters.

The NRCan satellite position error was initially estimated to be about 20 cm by Kouba et al. [1993], and later improved to the current about 10 cm level [IGS weekly reports at http://igscb.jpl.nasa.gov]. Thus it is reasonable to assume an average of 15 cm for the period of this study. The orbital error typically has an effect to the baseline estimates by

$$\frac{db}{b} = \frac{dr}{\alpha \cdot h} \tag{5.1}$$

where b is the baseline length, h is the height of GPS satellites (about 20200 km), db and dr are the baseline error and orbital error respectively, and α is a constant between 4 and 10 for random orbital errors [Zielinski, 1989] and 1 or even smaller for systematic orbital errors [Chen and Langley, 1990]. This implies that a systematic orbital error can do four to ten times as much damage as a random orbital error of the same magnitude, or in other words, a systematic orbital error can have the same effects as a random orbital error of four to ten times smaller in magnitude. Thus, for the WCDA solutions, the NRCan orbital error of 15 cm, if totally random, should have an effect between 0.7 and 1.9 parts per billion (**ppb**), or 0.2 to 0.6 mm for the shortest baseline (302 km) and 0.5 to 1.2 mm for the longest baseline (627 km). However, if there are global, systematic orbital errors of a few cm (whether or not reflected by the 15 cm rms), the effect on the solutions would be much more significant due to the scale factor α in equation (5.1).

Different components of an orbital error have different effects on baseline solutions. The radial component of the orbital error introduces an error in scale, while the lateral (along-track and cross-track) components cause an error in rotation. As suggested by Chen and Langley [1990], in double-differenced observations, the lateral orbital error has a larger effect on the baseline solution than the radial one. Meanwhile, from the perspective of a baseline, the vertical componenent of a baseline is more

readily to be impaired by an orbital error than the horizontal components. As the satellite geometry varies and the length of observation session and number of observed satellites increase, the effect due to orbital errors is usually largely reduced and tends to affect the solutions in a mainly random pattern. Nonetheless, small systematic effects due to orbital errors may exist and be manifested in long-term solutions.

In the NRCan orbit computations, the final orbits need to go through a transformation from an inertial coordinate system into an Earth-fixed coordinate system using the the estimated EOP parameters. Therefore, the error in the NRCan EOP estimates can bring about a rotation of the orbits of all satellites. If this error includes a systematic component, then the two defining factors of the reference frame for the WCDA become inconsistent: the precise orbits are rotating, while the reference station is held fixed in space. In other words, the DRAO coordinates implicitly defined by the precise orbits and the nominal ITRF values of DRAO coordinates are not identical. The systematic EOP error should be well within 1 milliarc second (mas). (1 mas is equivalent to 13 cm at the GPS orbital height, 3 cm on Earth's surface, or about 5 ppb in terms of relative positioning precision). The effect on the solutions due to such an inconsistency could probably be similar to that due to an error in the coordinates of the reference station, which unfortunately is highly systematic [Chen and Langley, 1990]. The magnitude of this effect, however, is expected to be small because of the normally small NRCan EOP errors (initially 0.5 mas and later improved to current 0.2 mas [Kouba et al., 1993; Lahaye et al., 1997].

5.2.2 Tropospheric Modelling Error

The second major error source is the tropospheric modelling error. As the tropospheric delay is highly correlated with the vertical component of a baseline, the estimate of the vertical component of a baseline is impaired the most among the three components by the tropospheric modelling error. According to Blewitt [1993], a qualitative assessment of the error in the vertical baseline component (σ_V) in millimetres due to tropospheric modelling error can be made for a regional or local scale network using a simple empirical equation:

$$\sigma_V\ (mm) \;=\; 0.75 \cdot L^{1/3} \tag{5.2}$$

where L is the length of a baseline in kilometres. This gives values of 5.0 mm for the shortest baseline (302 km) and 6.4 mm for the longest baseline (627 km) in the WCDA. There are assumptions associated with the above equation, however. One is that the wet tropospheric component is estimated only to within 5% and other error sources are negligible.

For the horizontal components of station coordinates, the tropospheric modelling error should be mostly averaged out because of the variation in the satellite geometry during a long observation period. However, asymmetric sky distribution of the observed satellites as well as any horizontal gradients (i.e., non-isotropic) in the tropospheric delay can certainly map the tropospheric modelling error into the horizontal components. Because of the mainly north-south satellite ground tracks, the east component is more readily affected by tropospheric errors than the north component.

The stochastic modelling of the local tropospheric parameters improves the baseline repeatability by a factor of 2 compared to deterministic modelling [Lichten and Border, 1987; Dixon and Wolf, 1990]. It compensates for the inaccuracy of the

adopted standard atmospheric data and the tropospheric model used. Hence different tropospheric models (for zenith delay calibration) such as the Hopfield model and Saastamoinen model would make insignificant difference to the solutions. However, the stochastic model also tends to compensate for any other height-dependent and elevation-angle-dependent systematic errors such as the tidal effects, antenna phase centre variations, and multipath effects, so that the estimated station heights in particular may still be biased [Kaniuth et al., 1989; Elósegui et al., 1995].

5.2.3 Multipath/Scattering Effects

There are two types of **multipath effects**. One is induced by **signal reflection** from far-field reflecting objects. The reflected signal interferes with the direct line-of-sight signal and causes a phase shift in the measured phase with respect to the phase of the direct signal. The phase shift varies in a cyclic pattern with the changing antenna-reflector-satellite geometry. This is conventionally what the signal multipath refers to. The other type of multipath is caused by a combination of **signal scattering**, **diffraction**, and even **imaging** from near-field reflecting/conducting structures in the vicinity of the antenna. For example, the GPS antenna at permanent tracking stations is typically mounted on a concrete-steel pillar, and it was found by Elósegui et al. [1995] that the pillar surfaces can scatter and its edges diffract the GPS signals. The scattering and diffraction can change the antenna electromagnetic properties. In addition, the conducting materials inside or around the pillar can cause antenna imaging, which changes the antenna phase pattern as well. These three effects are lumped together into the second category of multipath effects, because scattering, diffraction, and imaging have a similar, but not identical, effect on GPS phase measurements as signal reflection has and they usually take place at the same time and

their effects are indistinguishable from one another. It is clear, from the above descriptions, that the main difference between the two types of multipath effects is that while the former one does not affect the antenna electromagnetic field properties, the latter one does and causes a non-negligible coupling between the antenna phase pattern and the near-field reflecting and conducting structures. For clarity, in the following discussions and chapters, unless otherwise stated, the second type of multipath effect (near-field multipath) will be refered to as scattering, and the first type (far-field signal reflection) simply as multipath.

The boundary between the near-field and far-field of an antenna can be determined using the expression [Elósegui et al., 1995],

$$R = 2D^2/\lambda \tag{5.3}$$

where R is the radius of the assumed spherical boundary from the antenna phase centre, D is the maximum dimension of the antenna, and λ is the signal wavelength. For the Dorne-Margolin antenna with choke ring groundplane, which is used for all the WCDA sites, $D = 38.1$ cm, $\lambda_1 = 19.0$ cm for the L_1 frequency, and thus $R = 1.5$ m. For L_2, $R = 1.2$ m.

For multipath, the frequency of the multipath error, as summarized by Georgiadou and Kleusberg [1987] using geometric optics, depends on the signal wavelength, the perpendicular distance of the antenna phase centre from the reflector, the cosine of the satellite elevation angle above the reflector plane, and the rate of change of the satellite elevation angle. In general, the farther the reflector is located from the antenna phase centre, the higher the multipath frequency is. For example, in a standard situation (where average values are used) for the L_1 GPS signal, if the perpendicular distance from the reflecting plane to the antenna phase centre is 1.5 m, the period

of the multipath variations would be about 21.3 minutes. In contrast, the same reflector located at 10 m away would produce multipath variations with a period of 3.2 minutes. Hence, the variation period caused by multipath should typically be shorter than 20 minutes. If the observation time is significantly longer than the multipath periods, the effect of multipath error on the solutions can be largely averaged out. However, there is a pitfall related to the high frequency multipath. When the multipath frequency is higher than the **Nyquist frequency**, which is one half of the data sampling rate, **aliasing** would occur. That is, the high frequency multipath would appear to have some lower frequency constituents. For the WCDA data reduction, the Nyquist frequency is 1/240 Hz (corresponding to a period of 4 minutes, or two times the sample interval). Specifically in the above example, multipath from reflectors further than 8 m from the antenna phase centre could be aliased in the frequency domain.

For scattering, physical optics, rather than geometric optics, applies. Nevertheless, as shown by Elósegui et al. [1995], geometric optics can still be used as a good approximation. Therefore, in the standard situation described above, variation periods caused by scattering are in a range from 20 minutes to 11 hours (corresponding to scattering distances from 10 cm to 1.5 m). Furthermore, the low frequency errors are more difficult to average out. What makes the scattering more unwanted than the multipath is that the scattering/conducting structures can have a strong coupling with the antenna phase pattern. In this kind of environment, the scattering and conducting structures in fact become part of the antenna! Any change in the antenna setup, such as those related to the mounting device, the plexi-glass dome, the pillar, etc., could trigger an unexpected change in the antenna phase pattern, and thereby bias the solutions. Of course, the same kind of bias could also occur in

the case of multipath when the reflecting environment is changed or removed. However, permanent tracking sites are usually chosen very carefully to avoid any potential reflecting structures. In contrast, changes in antenna setup are unavoidable due to many reasons such as upgrade of the hardware and installation of auxiliary devices, etc. Therefore, it is the scattering that is much more difficult to deal with in regard to the permanent GPS tracking stations.

Without environmental/antenna setup changes, multipath/scattering can recur every sidereal day, or every UT day with about 4 minutes time advance, due to the repeated day-to-day satellite geometry. This important characteristic provides a way to identify multipath/scattering from the phase residuals. In addition, the multipath/scattering effect can be viewed as a modification to the antenna phase pattern, so it should have similar characteristics as the effect caused by antenna phase centre variation, in spite of the fact that the latter is completely independent of the environment. Consequently, changes associated with satellite elevation cutoff angle and GPS satellite geometric coverage can also affect the solutions. This makes the satellite elevation cutoff angle test a convenient method to identify multipath/scattering effects in the solutions.

Among the estimated baseline components, the vertical is affected the most by multipath/scattering, up to several centimetres. When the tropospheric parameters are estimated simultaneously with baseline components, the multipath/scattering effects on the vertical component can be magnified as the minimum satellite elevation angle increases [Elósegui et al., 1995]. This error appears in the daily solutions mainly as a constant bias from day to day until the environment or data processing strategy changes. Nonetheless to a certain extent, long-term, especially annual variations may exist due to the gradual daily change of satellite geometry in UT days. Normally,

the multipath effects on horizontal baseline components are insignificant, as shown by Elósegui et al. [1995]. However, the possibility that the multipath error can be mapped into horizontal baseline components under certain circumstances cannot be completely ruled out.

Due to the complexity of multipath effects, this error has not been modelled successfully thus far for high-precision relative positioning larger than a local scale. The stacking method and spectral method of multipath removal briefly introduced in section 4.4 have not been implemented satisfactorilly in the WCDA data analysis because other systematic errors may have biased the estimates of the multipath signal and the assumption on the whiteness of the residuals does not generally hold. Therefore, the multipath is certainly one of the major error sources at present in the WCDA data analysis.

5.2.4 GPS Monument Motions

Accurate monitoring of crustal deformation requires not only accurate instrumentation and state-of-the-art data processing, but also adequate coupling of the geodetic monuments to the Earth's crust. At present, most of the existing permanent GPS monuments are anchored only up to 3 metres below ground surface. Studies on long-term two-color geodimeter data have suggested that these shallowly anchored monuments may have significant motions relative to the crust [Langbein et al., 1995; Langbein and Johnson, 1997]. Primarily two types of displacements may be included in geodetic monument motions. One is a seasonal signal up to 3 mm in amplitude but typically less than 0.5 mm. The other is believed to be a random walk noise of about 1.3 mm/$\sqrt{yr}$ [Langbein and Johnson, 1997]. The seasonal signal is probably a result

of the response of the near-surface layer to the seasonal precipitation, and this signal is only significant for a small fraction of sites analyzed by Langbein and Johnson [1997]. The random walk noise is more commonly present, and is possibly caused by small random motions of the geodetic monuments with respect to the Earth's crust. The impact of these geodetic monument motions is to cause a time-dependent behaviour in the solution time series, therby greatly corrupting the rate estimates. In their studies, Langbein et al. [1995] and Langbein and Johnson [1997] have shown that deeply (5-10 m) anchored geodetic monuments attenuate the seasonal signals to within 1 mm and decrease the random walk noise by a factor of at least 3.

The WCDA GPS monuments are anchored to a depth from 1.5 m to 3 m, and thus are shallowly anchored and may be subject to these monument motions. The detection of these motions can be accomplished by proper spectral techniques. The seasonal signals should have an annual period and a phase lag correlated to the local precipitation cycle. The random walk noise should have a power spectral density proportional to f^{-2}, where f is frequency. However, without precipitation data, the source of the seasonal signals may not be identified exactly or with high confidence since other error sources, such as tropospheric mismodelling and systematic orbital errors, may also cause annual periodic signals. The detection of the random walk noise requires long time series. For instance, to detect a 1 mm/$\sqrt{yr}$ random walk noise, 5 years of daily GPS solutions with 3 mm horizontal precision are required [Langbein and Johnson, 1997]. Therefore, the current WCDA time series (about 2.5 years) is not sufficient to resolve the random walk motions of the GPS monuments.

5.2.5 Error in the Reference Station Coordinates

The error in the reference station coordinates can systematically affect the baseline solutions. Its effect is similar to what an orbital error could make, though it is comparatively much more systematic [Chen and Langley, 1990]. The error in the fixed reference station DRAO coordinates, as stated in section 5.1, can be up to about 6 centimetres before Febuary 1, 1994 and 2 cm thereafter as the ITRF velocity was not taken into account and DRAO was not held fixed in the NRCan daily orbit solutions. Therefore, this error may cause some small systematic errors in the solutions at the maximum magnitude of about 2 ppb before Febuary 1, 1994. However, this should be greatly improved after the DRAO coordinates was set to ITRF93 value at epoch 1995.0, which is supposedly accurate to 2 cm. This fact can help identify errors related to DRAO coordinates in the WCDA solutions.

5.2.6 Other Error Sources

There are many secondary error sources for the WCDA data analysis. These include the antenna phase centre variation, the uncertainty in tidal models, the higher-order ionospheric delay, the effect of antenna orientation, the effect of the post-glacial rebound, and the thermal and/or precipitation-related deformation of the antenna/pier structure. The following paragraphs give brief discussions on each of these error sources.

The **antenna phase centre variation** is due to the non-sphericity of the antenna phase pattern. It is angle dependent and causes the non-coincidence of the actual phase centre with the antenna geometric centre or the antenna coordinate origin [Wells

et al., 1986]. This effect is thus independent of the the antenna environment. For Dorne-Margolin antennas with choke ring, employed at all WCDA sites, the phase pattern is nearly isotropic with rms azimuthal variations at the 1-2 mm level and peak-to-peak vertical variation of 10-14 mm over an elevation angle range of 0-90 degrees [Elosequi et al., 1995]. Suppose that the phase pattern is similar for all the antennas at the WCDA sites. After the differencing between stations, this effect would be at the few mm level and can be reduced greatly by observing all satellites in view and lengthening the observation period. Hence, if the above assumption holds, the remaining effect on the WCDA solutions should be essentially a very small bias which does not affect the rate estimates at all.

The **uncertainty in the tidal models** is mainly from the ocean tide loading because unlike the solid Earth tides, the ocean tide loading has a more dramatic horizontal gradient, especially along a coastline. When stochastic tropospheric parameters are estimated, however, the mismodelled loading effects can be mostly compensated by these stochastic parameters. This could cause a bias in the solutions, but the bias should not affect rate estimates. In general, the residual tidal effects on the vertical component of baseline solutions could be a bias of few mm, while on the horizontal components its effects should be insignificant.

For a network of regional size, the effects due to **higher-order ionospheric delay, antenna orientation**, and **post-glacial rebound** are at sub-millimetre level, thus can be safely neglected without any significant loss of precision [Bassiri and Hajj, 1993; Wu et al., 1993; Tushingham, 1991; James and Morgan, 1990].

5.3 Chapter Summary

The estimation strategy specifically designed for the WCDA data reduction has been given and discussed in this chapter. Corresponding to this estimation strategy and measurement models used in CGPS22, the error budget is given. The major potential error sources that may cause problems in the WCDA solutions include: the errors in the precise orbit/EOP products, mismodelling of the tropospheric delay, the multipath/scattering effects, GPS monument motions, and the errors in the reference station DRAO coordinates.

Chapter 6

The WCDA Solutions and Analysis

Based on the estimation strategy described in Chapter 5, least squares solutions have been continuously conducted for the WCDA since September 1992. This chapter first summarizes the solutions and then describes extensive error analyses carried out by means of spectral techniques and specially designed tests. Then, the precisions in terms of short-term repeatability and long-term repeatability are presented and the estimated linear trends in the solutions are disussed to infer possible crustal deformation signals.

Section 6.1 presents the WCDA solutions, followed by an error analysis of the solutions in section 6.2. The precision assessment is given in section 6.3, and the deformation signals inferred from the WCDA solutions are discussed and compared with those from other techniques in section 6.4. Section 6.5 gives general remarks on the results.

6.1 The WCDA Solutions

For the purpose of this research, 31 months' worth of data from September 1992 to early April 1995 have been reduced using the NRCan precise orbits and the estimation strategy presented in Chapter 5. The processing of the daily data underwent some difficulties caused by hardware or software bugs, and there are noteworthy signatures of the multipath effects present in the residuals. Consequently, preceding the displays of the time series of the WCDA solutions, this section first describes the problems encountered during the data reduction, and then shows evidences of multipath effects found in the daily *a posteriori* double-differenced phase residuals.

The time series of the WCDA solutions consists of 811 daily solutions. There are some gaps in the time series, which are the days either when the WCDA receivers were not tracking well (mostly due to the activation of AS and equipment failures), or when the precise orbits were not available. The days with large data gaps at the reference station DRAO were also excluded. The receiver at HOLB malfunctioned from Febuary 1 to May 3 of 1994 due to the activated AS, therefore during this period no solutions were obtained for this station.

Some problems arose during the data reduction. 1) When Rogue receivers responded to the switching on (and off) of AS on the GPS satellites, a quarter cycle slip could be produced for the double-differenced carrier phase measurements [Blewitt, 1992]. If the switches were quite many, usually the data for the entire day were discarded. Otherwise, the data before or after the quarter cycle slip occurs were deleted. 2) On January 11, 1995, the operation software for the Turbo Rogue at ALBH was upgraded to version 3.0. However, this version turned out to have two

bugs when the receiver was tracking in the cross-correlation mode. First, the software can introduce a random fractional cycle slip after a break in the $L_1 - L_2$ phase. Second, when a satellite has low signal-to-noise-ratio (SNR), and there is another satellite being tracked with high SNR and the same Doppler, the low-SNR $L_1 \times L_2$ channel can be taken over for a few minutes by the high-SNR satellite. As a result, a "phase surge" is produced in the carrier phase measurement and the SNR jumps to the value of the high SNR satellite [Young, 1995]. The two bugs occurred mostly when a satellite was at low elevation angles, and they created many difficulties in the data editting for baseline ALBH-DRAO. The bugs were corrected in a later version of the software.

Although the WCDA sites were carefully selected and well equipped and maintained to avoid multipath/scattering, signatures that can be attributed to multipath/scattering were found from the *a posteriori* double-differenced phase residuals for two of the WCDA baselines: ALBH-DRAO and WILL-DRAO. As an example, **Figure 6.1** shows the double-differenced L_3 residuals for PRN17-PRN03 at WILL-DRAO on January 3 - 5, 1994. The residuals for January 4 and 5 have been shifted exactly by +2 and +4 cm respectively. The correlations between these residuals on different days are evidently very high and the time advance from day to day is close to 4 minutes. **Table 6.1** gives the correlation peak values and their corresponding time advances between different days (including January 3 - 5, and 9, 1994) for the then three WCDA baselines. For instance, for baseline ALBH-DRAO, the correlation peak value between January 3 and January 5 is 0.67 and its corresponding time advance is 8 minutes. A multipath/scattering signature should have a time advance of about 4 minutes each day. From Table 6.1, it is noted that ALBH-DRAO has the expected time advances, though the correlations are not particularly high. WILL-DRAO has very high correlations, and the time advances are unfortunately slightly biased (due

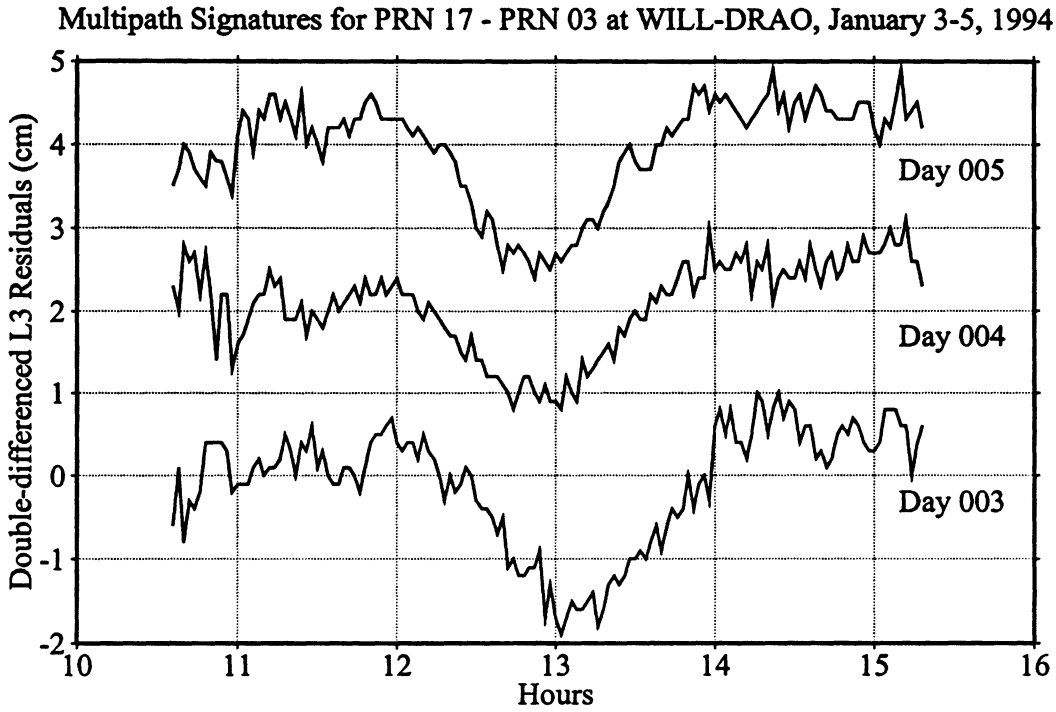

Figure 6.1: An example of multipath/scattering effects in the *a posteriori* double-differenced phase residuals for baseline WILL-DRAO. Days 004 and 005 are shifted by +2 and +4 cm respectively.

possibly to some other smaller systematic errors such as the orbital errors). The time advances for HOLB-DRAO are much more scattered from the expected values as it has the weakest, if any, multipath/scattering. Therefore, in later error analyses, ALBH-DRAO and WILL-DRAO should be monitored in particular for possible multipath effects in the solutions. In addition, the apparent periods for the multipath/scattering signatures in baselines ALBH-DRAO and WILL-DRAO are typically longer than 2 hours, as illustrated in Figure 6.1 for example. Considering that the variations caused by multipath usually have a period shorter than about 20 minutes (see Chapter 5), these signatures are more likely caused by scattering. However, since aliasing from very high frequency multipath (period shorter than 4 minutes in our case) or equivalently from far-far-field multipath (reflectors located more than 8 m

from the antenna phase centre) can also result in apparent low frequency variations, the exact identification of the true cause of the low frequency signatures requires an analysis on the coupling of the multipath/scattering effects with the antenna setups involved in the two baselines.

Table 6.1: The correlation peak values and corresponding time advances (in minutes) in double-differenced daily phase residuals between different days (January 3, 4, 5, and 9, 1994). (see text).

Baseline ALBH-DRAO			
	1/4/94	1/5/94	1/9/94
1/3/94	0.67/4	0.67/8	0.57/24
1/4/94		0.62/4	0.58/20
1/5/94			0.73/16
Baseline WILL-DRAO			
	1/4/94	1/5/94	1/9/94
1/3/94	0.86/12	0.93/14	0.91/30
1/4/94		0.83/2	0.84/18
1/5/94			0.88/16
Baseline HOLB-DRAO			
	1/4/94	1/5/94	1/9/94
1/3/94	0.60/76	0.69/8	0.85/26
1/4/94		0.74/0	0.60/12
1/5/94			0.78/16

The multipath/scattering signatures vary in magnitude during different periods of time. For example, WILL-DRAO suffered the worst during the winter of 1993-1994. Then after the plexi-glass dome was installed in June 1994, the multipath/scattering effects did not appear as significant in the following winters. This seems to indicate that the effects have a coupling with the antenna setup or the environment at the immediate vicinity of the antenna. Therefore, scattering should be held responsible for the low frequency variations present in the phase residuals. In contrast, ALBH-DRAO suffered the worst in the summer of 1994. It was additionally aggravated by

the activated AS since Febuary 1994, which causes lowered signal strength in the cross-correlation operation mode. In addition, there were cycle slips that repeated almost every day at low elevation angles with exactly 4 minutes time advance for baseline ALBH-DRAO. The situation improved after early 1995. The initial suspicion was to the trees in the nearby environment. Effort was made to clear the foliage on the trees in early 1995. However, this was also coincident with the change of antenna setup (Table 3.2). Therefore, the exact cause for the low frequency signatures is still unidentified.

Since the WCDA data processing uses the double-differenced observables, the solutions obtained from the least squares adjustments are the relative displacements in north, east, and upward baseline components and baseline length of the non-fixed WCDA sites ALBH, HOLB, WILL, and UCLU with respect to the reference site DRAO. **Figures 6.2-20** show the time series of the daily WCDA solutions over approximately three years.

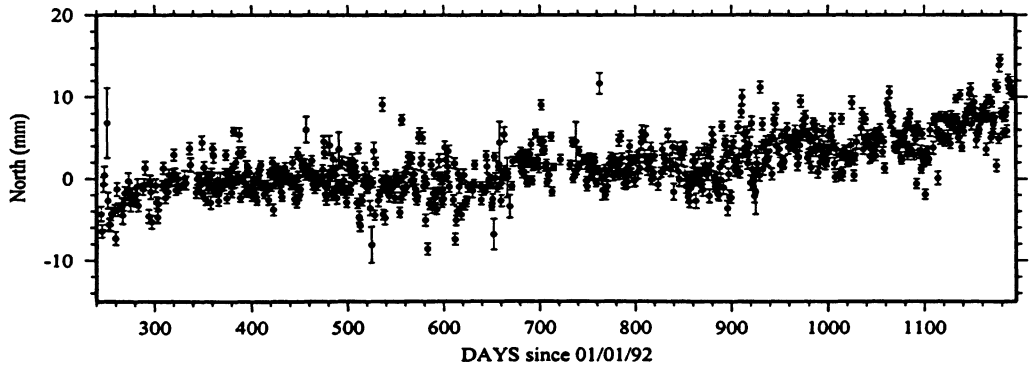

Figure 6.2: North component of the baseline ALBH-DRAO.

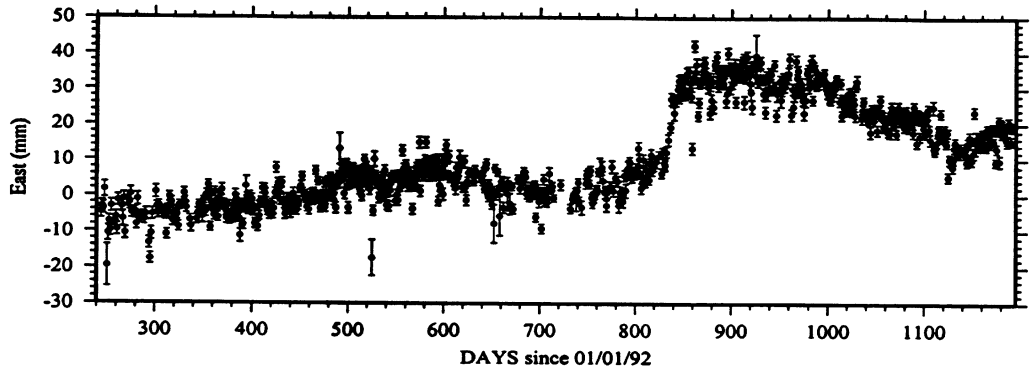

Figure 6.3: East component of the baseline ALBH-DRAO.

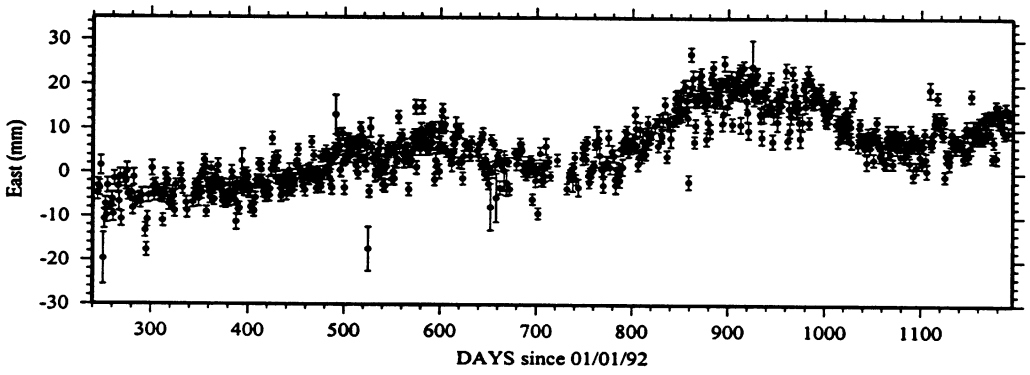

Figure 6.4: East component of the baseline ALBH-DRAO (offsets at days 835 and 1107 corrected).

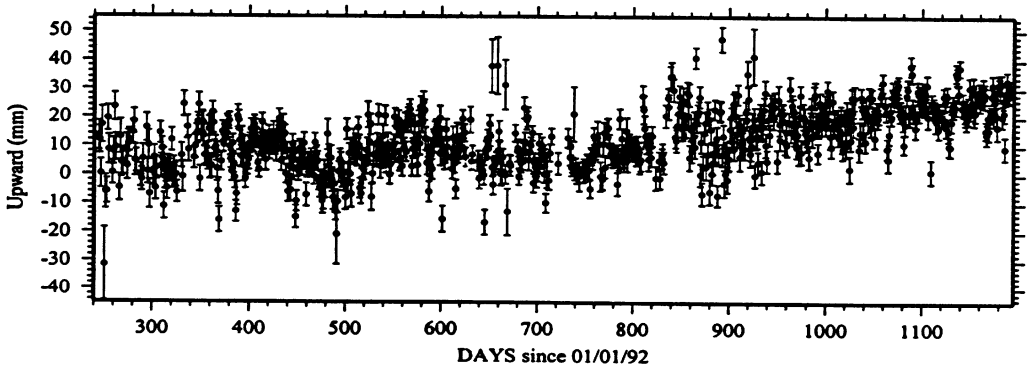

Figure 6.5: Upward component of the baseline ALBH-DRAO.

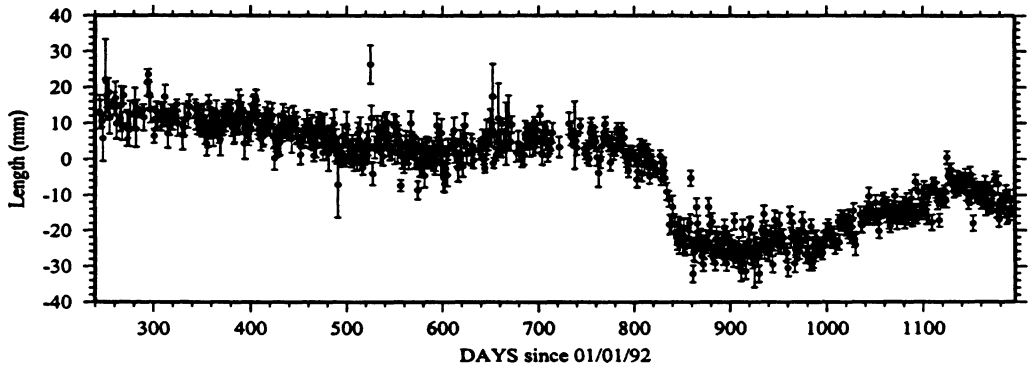

Figure 6.6: Length of the baseline ALBH-DRAO.

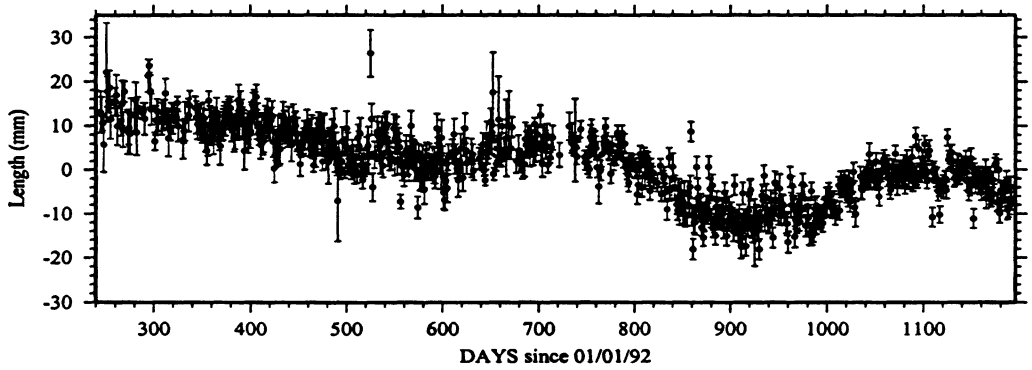

Figure 6.7: Length of the baseline ALBH-DRAO (offsets at days 835 and 1107 corrected).

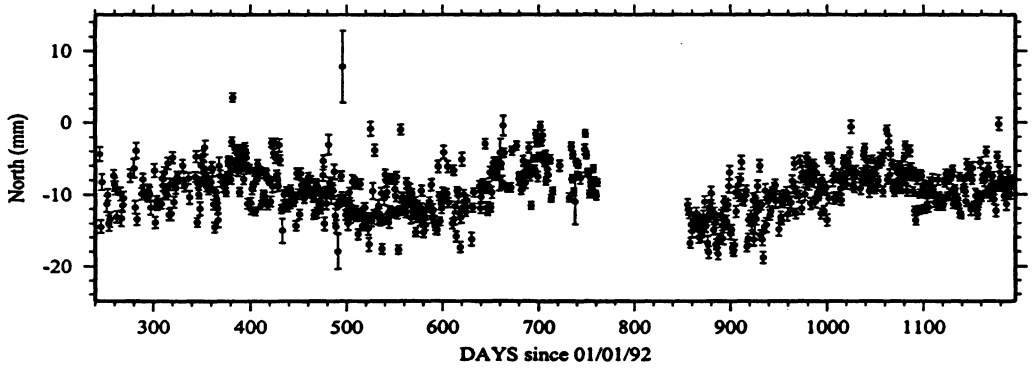

Figure 6.8: North component of the baseline HOLB-DRAO.

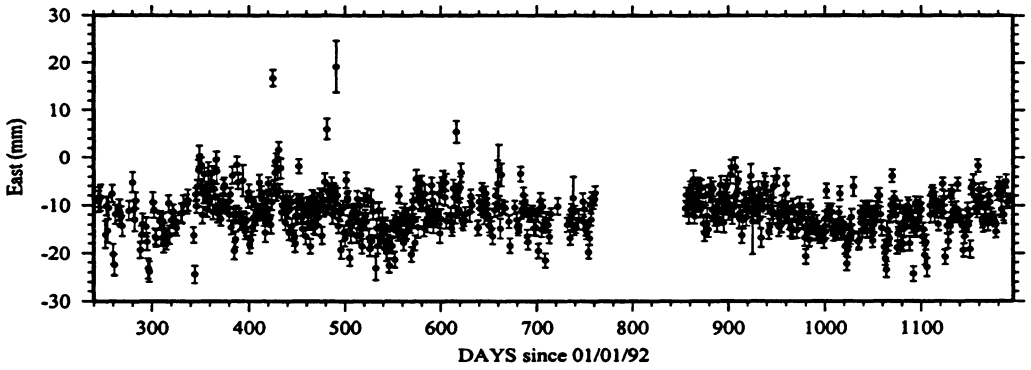

Figure 6.9: East component of the baseline HOLB-DRAO.

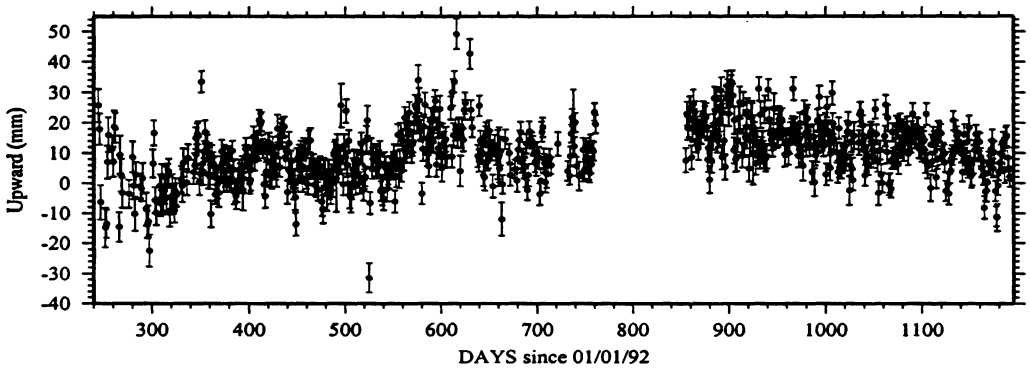

Figure 6.10: Upward component of the baseline HOLB-DRAO.

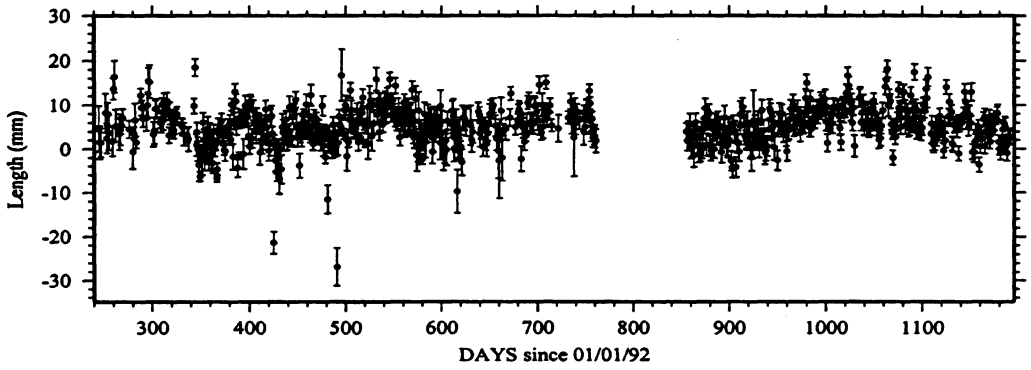

Figure 6.11: Length of the baseline HOLB-DRAO.

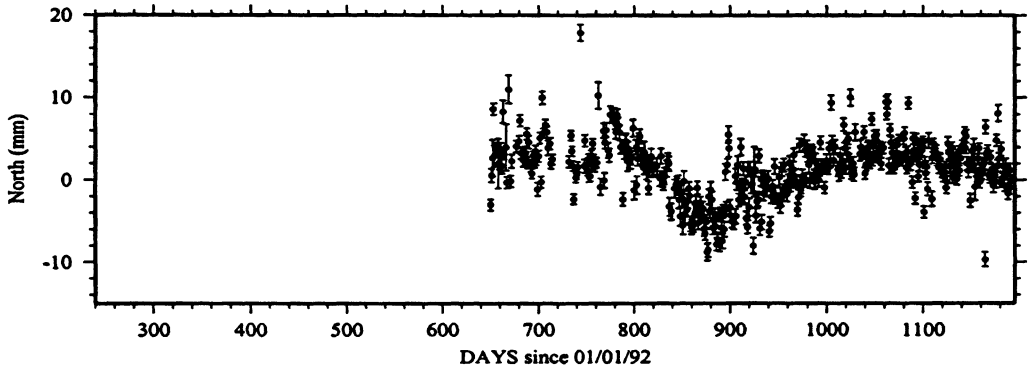

Figure 6.12: North component of the baseline WILL-DRAO.

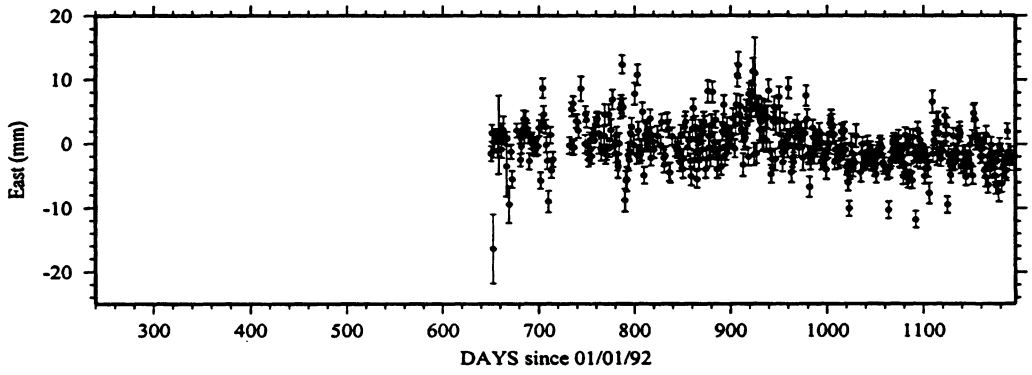

Figure 6.13: East component of the baseline WILL-DRAO.

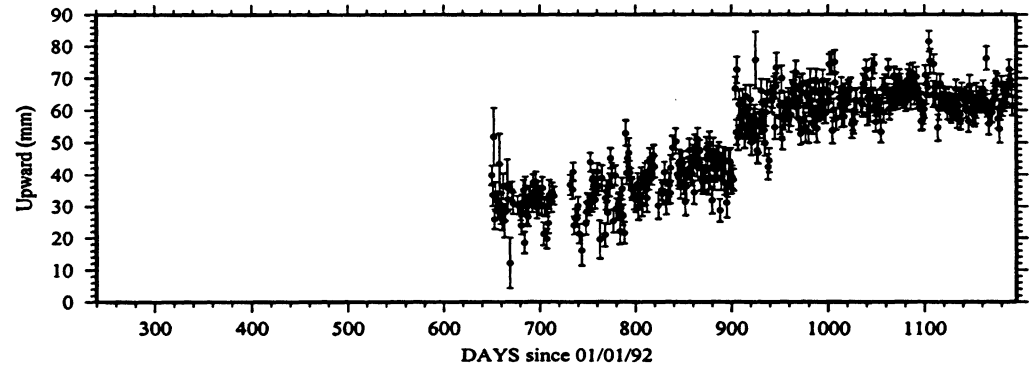

Figure 6.14: Upward component of the baseline WILL-DRAO.

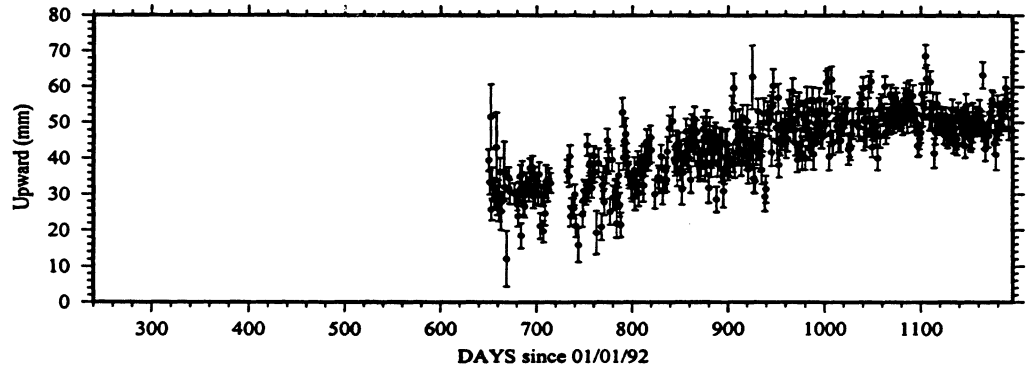

Figure 6.15: Upward component of the baseline WILL-DRAO (offset at day 835 corrected).

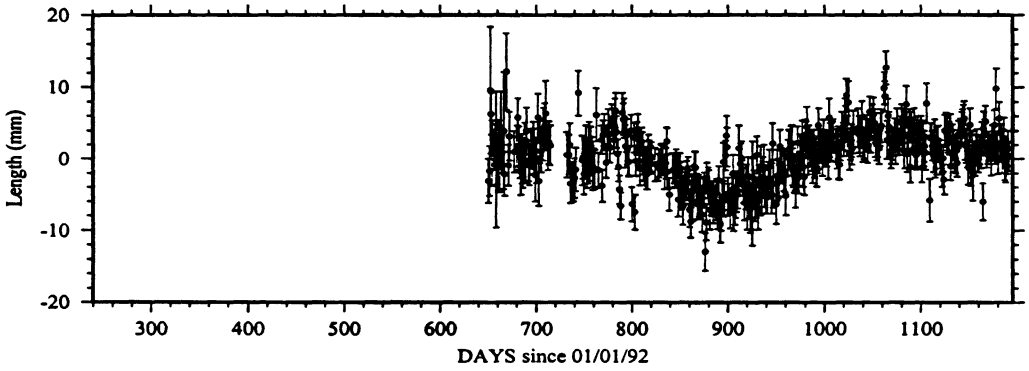

Figure 6.16: Length of the baseline WILL-DRAO.

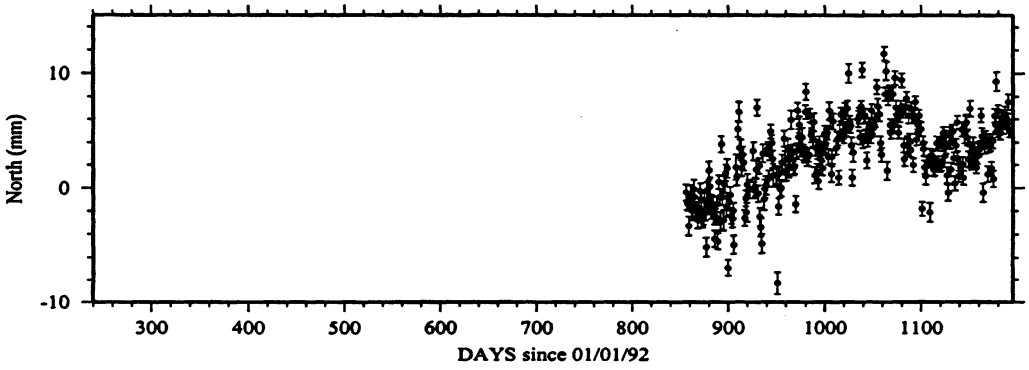

Figure 6.17: North component of the baseline UCLU-DRAO.

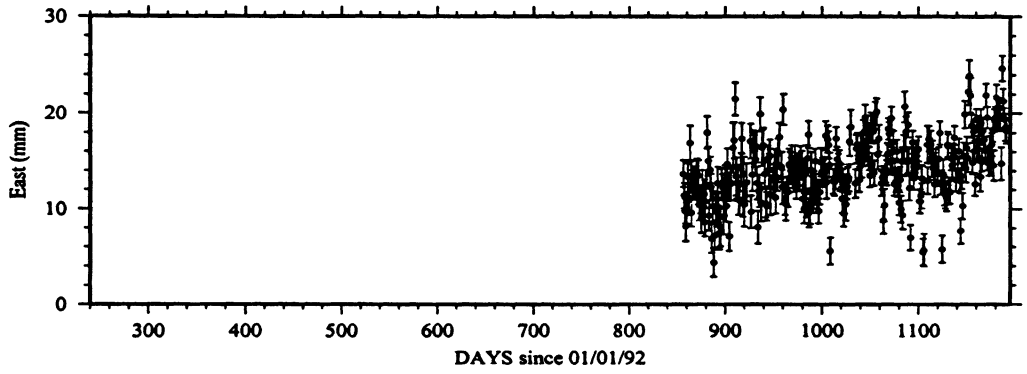

Figure 6.18: East component of the baseline UCLU-DRAO.

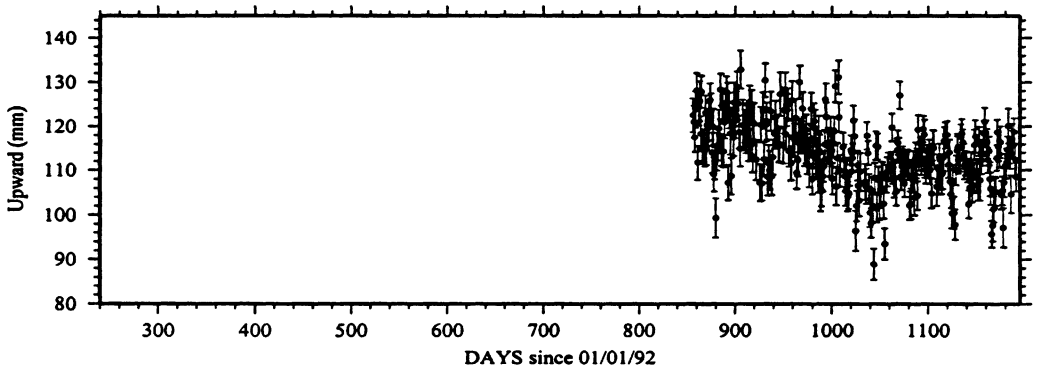

Figure 6.19: Upward component of the baseline UCLU-DRAO.

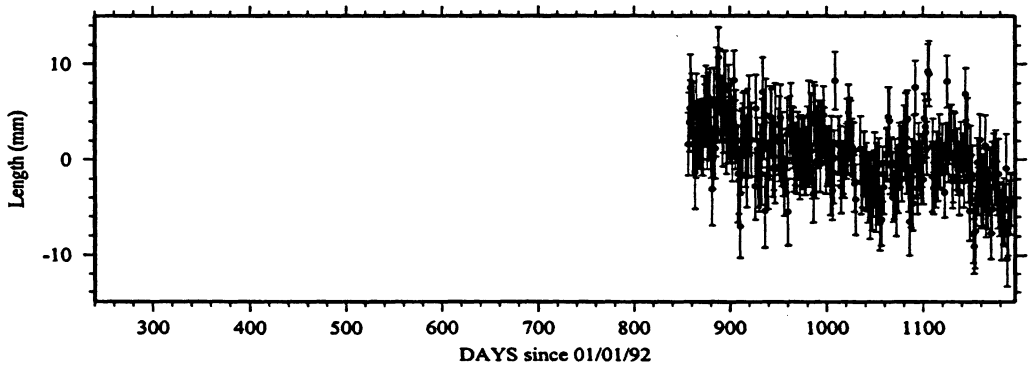

Figure 6.20: Length of the baseline UCLU-DRAO.

The nominal coordinates of DRAO were changed to the ITRF93 values on February 1, 1994. Accordingly, the solutions thereafter have been corrected for the change to maintain consistency. The corrections were obtained for each of the baselines by running daily solutions for a number of days with both the old and new reference coordinates.

In Figures 6.3, 6.6, and 6.14, there are apparent solution offsets. These were found to be coincident with changes in the antenna setup at two of the sites: ALBH and WILL! The antennas at WCDA sites are all forced-centred and the solutions refer to the bench mark by correcting the antenna phase centre offsets. Therefore, these offsets are not at all related to the geometric movement of the antennas. A very possible source for the solution offsets is the scattering effects, considering the multipath/scattering signatures in the phase residuals of the two baselines ALBH-DRAO and WILL-DRAO. A thorough investigation on the offsets and the source of the offsets will be carried out in the next section.

The first offset appears in the east component (Figure 6.3) and baseline length (Figure 6.6) of ALBH-DRAO on day 104 of 1994 (April 14, 1994, or day 835 since 1992.0, see **Table 3.2**) when the antenna at ALBH was changed from a Dorne Margolin type B (serial number 119) to a type T (serial number 172). The second offset is a smaller one, also visible in the the east component and baseline length of ALBH-DRAO, on day 011 of 1995 (January 11, 1995, or day 1107 since 1992.0) when the antenna at ALBH was changed from serial number 172 to serial number 368. The third offset is in the upward component of WILL-DRAO on day 172 of 1994 (June 21, 1994, or day 903 since 1992.0) when a plexi-glass dome was installed over the antenna. These offsets are identified as being significant with errors in the estimates of the offsets no greater than 25% of their magnitudes as determined by the Least

Table 6.2: The estimated solution offsets.

Component & Baseline	*Date*	*Offset ± 1 σ (mm)*
E of ALBH-DRAO	04/14/94 (day 835 since 1992.0)	+19.1±1.2
L of ALBH-DRAO	04/14/94 (day 835 since 1992.0)	-18.0±1.2
E of ALBH-DRAO	01/11/95 (day 1107 since 1992.0)	-13.0±1.7
L of ALBH-DRAO	01/11/95 (day 1107 since 1992.0)	+11.0±1.6
U of WILL-DRAO	06/21/94 (day 903 since 1992.0)	+18.7±4.5

Squares Spectral Analysis (LSSA) technique [Wells et al., 1985]. The maginitudes and formal errors of the estimated offsets are listed in Table 6.2, and the corrected solutions are shown in Figures 6.4, 6.7, and 6.15.

The error bars shown in Figures 6.2-6.20 represent the formal errors of the estimates obtained from the least squares adjustments. Obviously, these formal errors underestimate the true uncertainties by a factor of 2 to 4, possibly due to the errors unmodelled or mismodelled in the GPS measurements.

6.2 Analysis of the WCDA Solutions

This section is divided into three subsections describing three analyses of the solutions. First, a spectral analysis was conducted to identify significant periodic errors in the WCDA solutions; second, an analysis was carried out on the larger annual variations and offsets found in the solutions by means of satellite elevation cutoff angle tests; and third, the smaller annual variations in the north component as a special group were analyzed with extensive tests on potential error sources.

6.2.1 Spectral Analysis

In order to identify any significant frequency constituents and to determine the offsets and linear trends in the solutions, a spectral analysis was conducted using the LSSA algorithm [Wells et al., 1985]. The LSSA method has the capability to deal with gappy data and data with datum shifts (or offsets), trends, and periodic constituents. The **LSSA spectral value** is defined as the ratio (in %) of the contribution of a frequency constituent to the total variance of a time series. Thus, the LSSA spectral value is a measure of the power spectral density. The **resolution** of LSSA is similar to that of the periodogram estimator, i.e., approximately $\frac{1}{N}$ cycle/sample, where N is the length of the sample set. Obviously, the longer the sample set, the more accurate the frequency estimates. For the WCDA, $N = 947$ days for ALBH-DRAO and HOLB-DRAO, $N = 542$ days for WILL-DRAO, and $N = 336$ days for UCLU-DRAO. Correspondingly, the **fidelity** of a period estimate P is $\pm\frac{P^2}{2N}$ samples. For instance, an estimated annual periodic constituent should have a fidelity of ± 70 days for ALBH-DRAO and HOLB-DRAO, ± 123 days for WILL-DRAO, and ± 198 days for UCLU-DRAO. Due to the many gaps in the WCDA solution sets, the true fidelities may be somewhat worse than those given above.

The estimated parameters from LSSA include datum offset(s), one linear trend, and one dominant periodic constituent if the spectral value is greater than 25% (assumed significance level). The results are listed in **Table 6.3**. In Table 6.3, columns 1 and 2 are the baselines and components (N for north, E for east, U for upward, and L for baseline length). Columns 3 and 4 are the dominant periods (P, in days) and spectral values (S, in %). Columns 5 and 6 are the estimated amplitudes (in mm) and phases of the first point in solution sets (in degrees), along with their formal errors, for an annual (365.25 days) period if the spectral value in column 4 is greater

Table 6.3: LSSA results of the WCDA solutions. (see text).

Baseline	C	P (days)	S (%)	Amp. (mm)	Phase (deg)	L. Rate (mm/yr)	σ (mm)
ALBH-DRAO	N	DC	10.8			3.2±0.1	2.5
	E	367	40.3	4.9±0.2	174±12	6.0±0.4	4.0
	U	DC	7.9			8.3±0.4	8.4
	L	376	37.3	4.4±0.2	353±12	-6.4±0.4	3.8
HOLB-DRAO	N	342	30.0	2.5±0.1	345±9	0.0±0.1	2.9
	E	251	11.7			-0.4±0.2	4.5
	U	DC	14.7			3.7±0.4	8.7
	L	251	11.3			0.7±0.2	4.4
WILL-DRAO	N	350	41.6	3.3±0.2	343±10	-0.4±0.3	2.7
	E	188	8.5			-2.2±0.4	3.5
	U	DC	10.7			11.5±1.3	5.9
	L	358	42.4	3.5±0.2	341±11	1.6±0.3	2.8
UCLU-DRAO	N	260	32.9	2.1±0.2	282±19	7.2±0.9	2.3
	E	117	11.6			5.7±0.6	3.0
	U	235	9.7			-12.6±1.4	6.4
	L	118	12.7			-6.9±0.6	3.0

than 25% and the dominant period is within annual period ± fidelity value. Column 7 is the estimated linear rate along with its formal error (in mm/yr), and column 8 is the standard deviation (σ_l in mm) of the residuals. As the baseline length is actually dependent on the three baseline components, the estimates for baseline length may show strong coupling with those for a baseline component. Depending on the baseline orientation, the degree of this coupling varies for the three baseline components. The estimated datum offsets have already been given in Table 6.2. The period estimates that are larger than the length of the time series or significantly longer than one year are termed as **DC** terms. For these terms and those spectral components with spectral values below the 25% significance level, amplitude and phase are meaningless and are thus absent in Table 6.3.

In Table 6.3, there are six spectral values above the significance level. Their

corresponding components are the east and length components of ALBH-DRAO, the north component of HOLB-DRAO, the north and length components of WILL-DRAO, and the north component of UCLU-DRAO. Notably, all these significant periods are relatively close to the annual period considering their accuracies. For example, the periods for both the east and length components of ALBH-DRAO are well within the approximately ±70-day LSSA fidelity for an annual period. The period for the north component of UCLU-DRAO is subject to the largest bias, but the bias is still within the ±198-day fidelity for this baseline.

The annual variations found from the spectral analysis (Table 6.3) can be divided into two groups with different properties. The first is the variation in the east component of ALBH-DRAO, and the second is those in the north component. (Remember that baseline lengths are dependent on the baseline components). The first group of variations, along with the apparent solution offsets, are going to be discussed in the next subsection with satellite elevation cutoff angle tests, while the second group of variations will be analyzed separately in subsection 6.2.3. Additionally, the σ and the linear rate estimates listed in Table 6.3 will be discussed in sections 6.3 and 6.4 respectively.

6.2.2 Elevation Cutoff Angle Tests

Looking more closely into the time series of the east and length components of ALBH-DRAO (Figures 6.4 and 6.7), we can find that the large non-linear variations are not pervasive throughout the time span, but started approximately in the Fall of 1993. Hence, in order to get more accurate amplitude estimates for the variations, LSSA has also been conducted on the subsets of the east and length components time

series of ALBH-DRAO since September 7, 1993 (day 250 of 1993, or day 616 since January 1, 1992), which is assumed to be the approximate start of the variations. The dominant periods estimated from the subsets are 407 days for both the east and length components with the same spectral value of 45%, and the amplitudes for a forced annual period are 6.8 ± 0.4 mm and 6.5 ± 0.4 mm for the east and length components respectively. Although the period estimates are biased more than those in Table 6.3 due to the significantly (1 year) shorter time series, the amplitude estimates should be more accurate than those listed in Table 6.3. Therefore, we can state that the annual variations in the east and length components of ALBH-DRAO have an amplitude of approximately 7 mm.

Tests with different elevation cutoff angles have been carried out to investigate the source of the annual variations and the solution offsets as well. The primary suspects in these tests are the multipath/scattering effects and phase centre variation, as errors caused by these two sources have a strong dependence on the satellite elevation cutoff angle. **Figures 6.21-6.24** show the solutions for baseline ALBH-DRAO with a 30-degree elevation cutoff angle. The LSSA results with the 30-degree elevation cutoff angle are compiled in **Table 6.4**. Evidently, the large variations in the east and length components are significantly reduced. The spectral values are now about 9%, well below the 25% significance level, and the amplitudes become 1.7 mm, considerably smaller than those in Table 6.3 (4.9 and 4.4 mm). The offsets are also reduced significantly, from 19.1 mm to 16.6 mm (or by 13%) for the first offset in the east component and -13.0 mm to -5.5 mm (or by 58%) for the second offset in the east component, although these decreases are not as much as in the amplitudes. These indications prove that the large annual variations and offsets in the east and length components of ALBH-DRAO have an overwhelming dependence on the satellite elevation cutoff angle used in the data processing. Since from the daily data processing

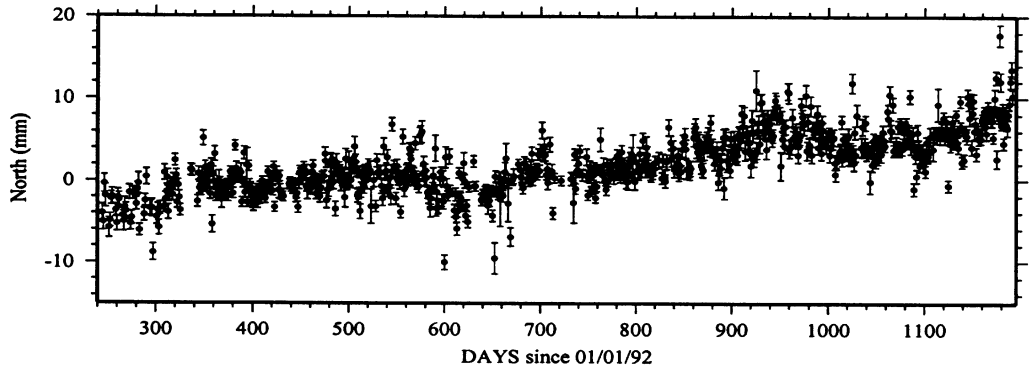

Figure 6.21: North component of the baseline ALBH-DRAO with 30° cutoff angle.

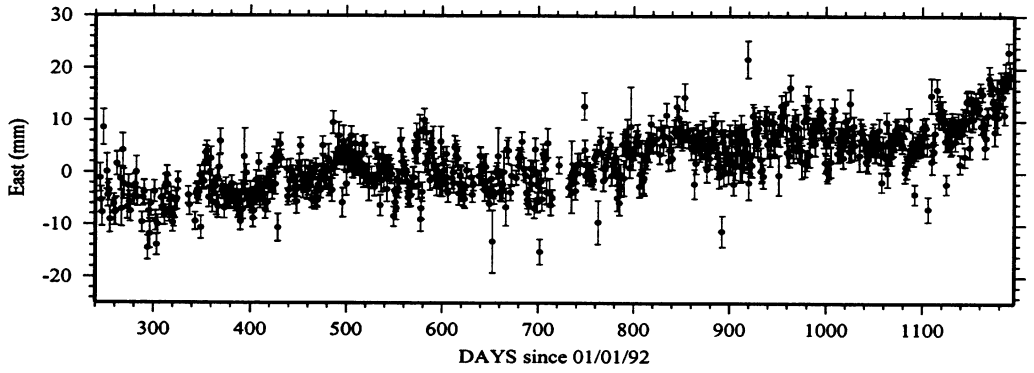

Figure 6.22: East component of the baseline ALBH-DRAO with 30° cutoff angle (offsets corrected).

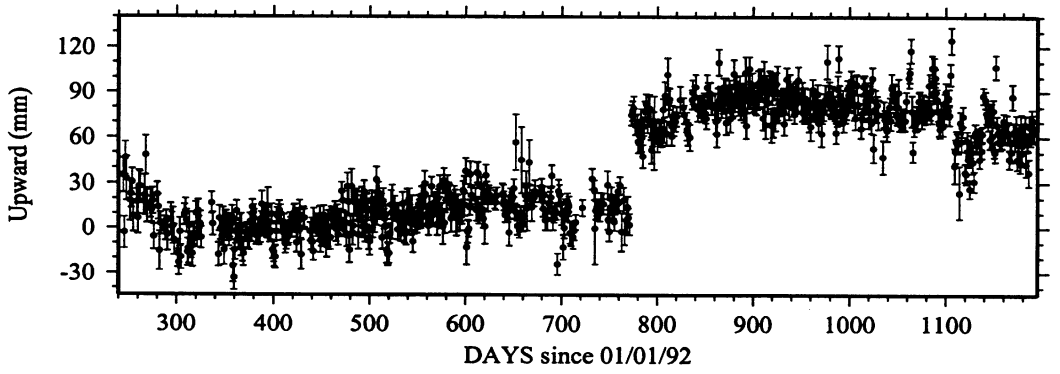

Figure 6.23: Upward component of the baseline ALBH-DRAO with 30° cutoff angle.

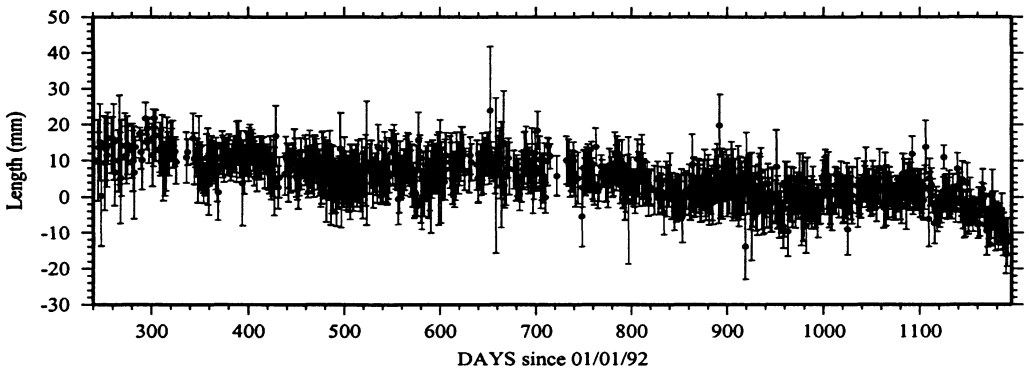

Figure 6.24: Length component of the baseline ALBH-DRAO with 30° cutoff angle (offsets corrected).

we knew that ALBH suffered from multipath/scattering effects during the period (see section 6.1) and more than one antenna was involved at ALBH, it is more likely that these large annual variations in the east and length components of ALBH-DRAO were caused by the multipath/scattering effects than by the anomalous antenna phase centre variations, unless we assume these antennas happened to have the same problem (anomalously large phase centre variation), which is apparently not very plausible. Following discussions will further consolidate this claim.

Table 6.4: LSSA results of the ALBH-DRAO solutions with 30° cutoff angle. (see text for Table 6.3).

Baseline	C	P days	S %	Amp mm	L. Rate mm/yr	Offset 1 mm	Offset 2 mm
ALBH-	E	386	8.6	1.7±0.2	4.5±0.4	16.6±1.2	-5.5±1.7
DRAO	L	418	9.3	1.7±0.2	-4.3±0.4	-15.6±1.2	3.9±1.7

From Figure 6.23, it is interesting to note that there are two new offsets manifested in the upward component on day 772 (Febuary 10, 1994) and day 1107 (January 11, 1995). Neither offset is present in the solutions with 15-degree cutoff angle (Figure

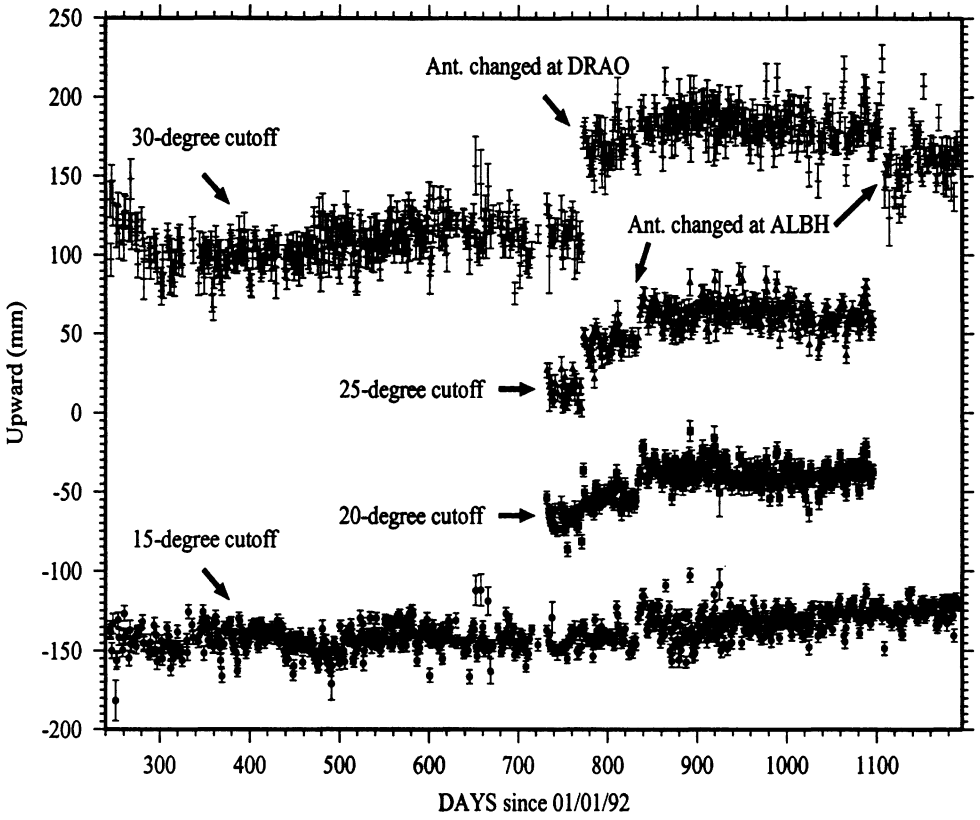

Figure 6.25: Upward component of the baseline ALBH-DRAO with different cutoff angles.

6.5). Checked with Table 3.2 which lists all antenna setup changes, the two offsets are found coincidental with the antenna setup changes at DRAO and ALBH respectively. To verify these offsets and see how they change with satellite elevation cutoff angle, solutions for ALBH-DRAO with 20-degree and 25-degree cutoff angles have been produced for all of 1994. The upward components of these solutions are displayed in **Figure 6.25** with proper vertical shifts (-150 mm for the solution set with a 15-degree cutoff angle, -75 mm for the 20-degree set, 0 mm for the 25-degree set, and +100 mm for the 30-degree set). Before the antenna change at DRAO, each solution set is continuous (or without apparent offset). Clearly, with the increase of the elevation

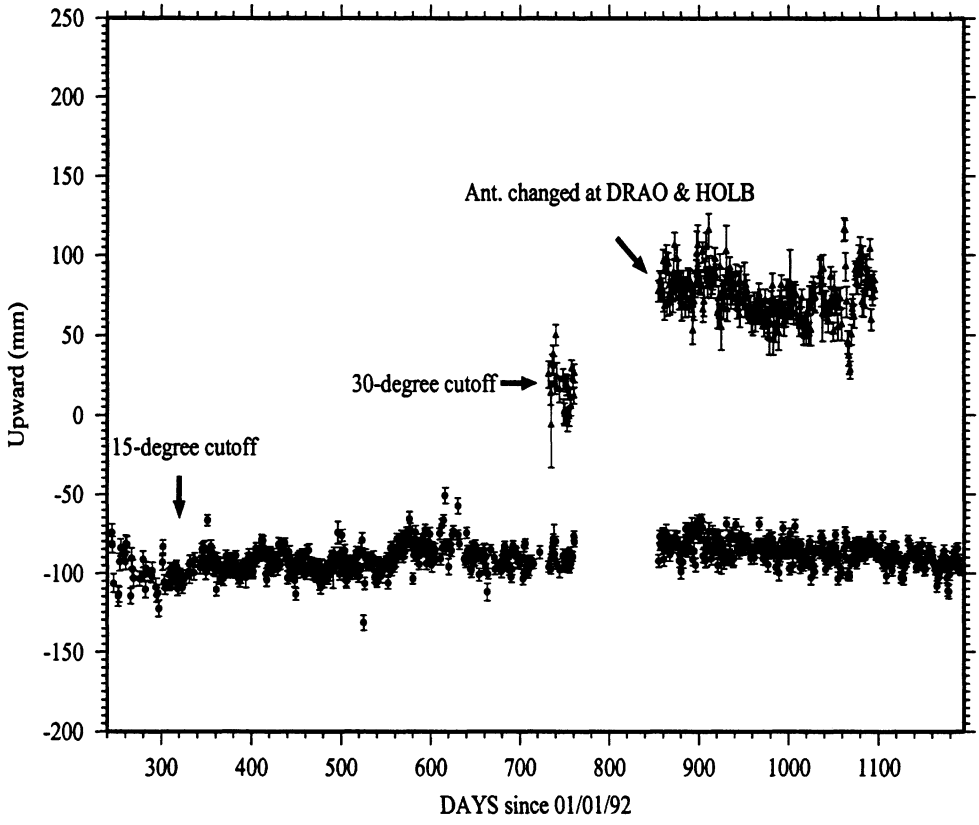

Figure 6.26: Upward component of the baseline HOLB-DRAO with different cutoff angles.

cutoff angle, the first offset on day 772 appears and grows from nought to as much as about 60 mm. The second offset on day 1107 also becomes noticeable with the 30-degree cutoff.

To verify that the first elevation-cutoff-angle-dependent offset is due to the antenna change at DRAO, solutions for baselines HOLB-DRAO, WILL-DRAO and UCLU-DRAO have been produced with a 30-degree cutoff angle. The rationale for doing this test is that if the offset is truely caused by the antenna change at the reference site DRAO, the same elevation-cutoff-angle-dependent offset should appear in all the baselines at the same time with the same size. The results of HOLB-DRAO

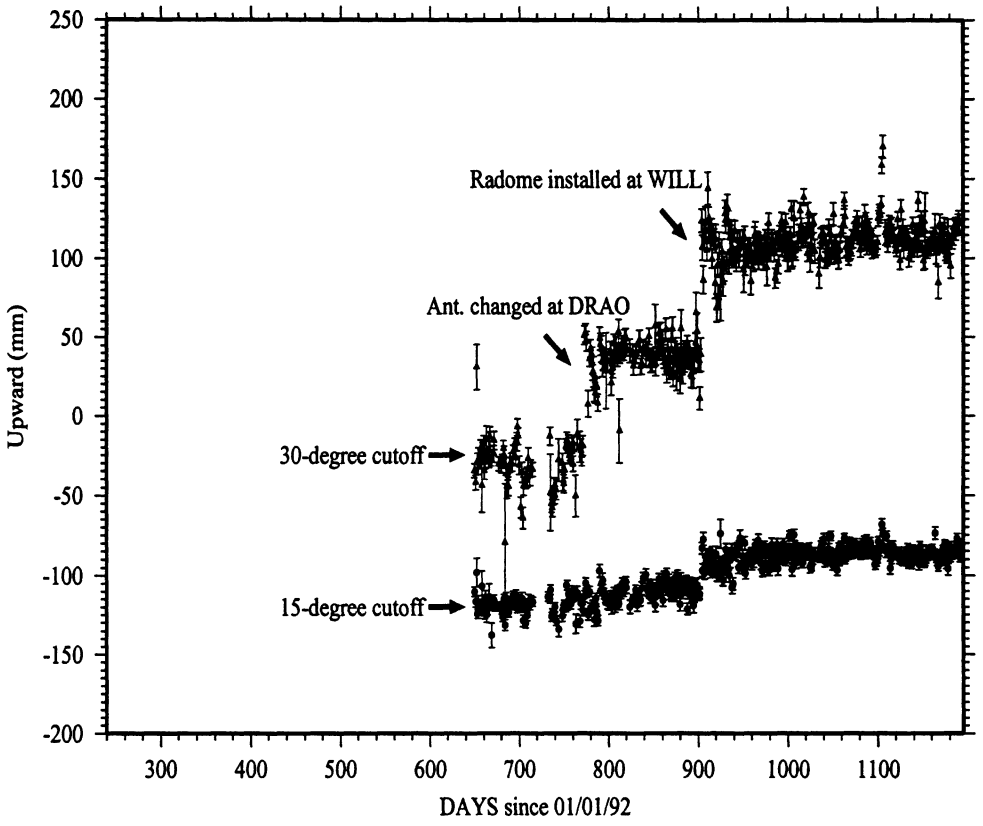

Figure 6.27: Upward component of the baseline WILL-DRAO with different cutoff angles.

and WILL-DRAO are shown in **Figures 6.26** and **6.27** respectively with the same vertical shifts and with the same scale as in Figure 6.25. The solutions for WILL-DRAO with a 15-degree cutoff in Figure 6.27 are not corrected for the offset listed in Table 6.2. It is found that in both Figure 6.26 and Figure 6.27 the offset at the time of the antenna change at DRAO is elevation-cutoff-angle-dependent and has approximately the same size, i.e., 60 mm. The result for baseline UCLU-DRAO gives the same outcome, though it is not shown here. Thus, it is firmly verified that this elevation-cutoff-angle-dependent offset is caused by the antenna change at DRAO. Since it was reported that the Dorne-Margolin antennas had phase centre variations

at most at one centimetre level (see Chapter 5), these large elevation-cutoff-angle-dependent offsets can be attributed to scattering effects triggered by the antenna change at DRAO. The same can be said of the offset on day 1107, except that this one is caused by the scattering effects at ALBH.

It can be noted that there is a small elevation-cutoff-angle-dependent offset for ALBH-DRAO (Figure 6.25) on day 835 (April 14, 1994), when the antenna at ALBH was changed and the offset in the east component occured (Figure 6.3). It seems to reach its maximum with the 25-degree elevation cutoff angle and diminishes both above and below this cutoff. What makes this offset unique compared to others is that it exists not only in the upward component but also in the east component. It is stated in Chapter 5 that multipath/scattering effects usually do not cause a significant error in the horizontal components. However, this statement, which is originally derived from simplified experiments [Elósegui et al., 1995], does not rule out the posibility that in certain adverse circumstances, where, for example, there exists multipath/scattering and signal blocking, multipath/scattering effects do project into horizontal components. At least intuitively it does make sense that an asymmetric azimuthal distribution of observations and multipath/scattering effects would cause significant errors in the horizontal components. The daily repeated cycle slips described in section 6.1 are possibly a sign of signal blocking (physically or electronically). While there is a lack of other plausible candidates, the scattering effects do reasonably explain the elevation-cutoff-angle-dependence displayed by both the large variations and offsets in the east component of baseline ALBH-DRAO.

In Figure 6.27, the second elevation-cutoff-angle-dependent offset for baseline WILL-DRAO on day 903 (June 21, 1994) grows from 18.7 mm with a 15-degree

cutoff to about 75 mm with a 30-degree cutoff. What is special for this offset, however, is that on day 903 the antenna was not changed but a plexi-glass dome was installed. The plexi-glass dome was installed by attaching an extra metal ring to the baseplate of the antenna. Thus there is a high potential that this added structure could cause signal scattering or imaging just because of the metal material alone. The occurance of this elevation-cutoff-angle-dependent offset is a concluding piece of evidence for scattering effects and further rules out other possible error sources such as excessive antenna phase centre variation and far-field multipath.

It should be noted here that not all antenna changes brought about elevation-cutoff-angle-dependent offsets. The occurrance of those offsets after all depend on the scattering environment. For example, in Figure 6.26, there was an antenna change at HOLB during the gap when HOLB failed to produce good data and meanwhile the antenna change at DRAO caused an elevation-cutoff-angle-dependent offset of about 60 mm at a 30-degree cutoff angle for all the baselines. Based on the size of the offset in Figure 6.26, it was found that unlike other antenna changes listed in Table 3.2, this particular antenna change at HOLB did not cause any significant elevation-cutoff-angle-dependent offsets. This is also consistent with the observation from the daily double-differenced phase residuals that HOLB has very weak if not zero multipath/scattering effects, as stated in section 6.1.

In summary, ALBH, DRAO, and WILL experienced apparent scattering effects. They caused satellite elevation-cutoff-angle-dependent offsets in upward components of the pertinent baselines whenever there was an antenna setup change at these sites. The large annual variation and offsets in the east component of ALBH-DRAO also displayed the elevation-cutoff-angle-dependence and are believed to be caused by the same scattering effects, but perhaps with certain special environmental setting such

as signal blocking at ALBH.

6.2.3 Analysis of the Small Variations in the North Components

In order to identify the error source of the small variations in the north component of three WCDA baselines, several tests were carried out. These tests dealt with the polynomial representations of the precise orbits, the tidal corrections, the satellite antenna offsets, the tropospheric modelling, and the quality of NRCan precise orbits.

This subsection is divided into four parts. First, the features of these variations are summarized and the tests are described. Second, the results of these tests are outlined. Third, a more detailed analysis carried out on the result from one of the tests is described , and last, a summary of important results concludes this subsection.

I. Features of the Variations and Descriptions of the Tests

As suggested in Table 6.3, the north components of HOLB-DRAO, WILL-DRAO, and UCLU-DRAO show significant (spectral value > 25%) quasi-annual variations. The time series of the north component of these three baselines are displayed in **Figure 6.28** with proper vertical shifts (+10 mm for HOLB-DRAO, +20 mm for WILL-DRAO, and -25 mm for UCLU-DRAO). Two antenna changes are also indicated in Figure 6.28. Clearly, the three time series show almost the same phase pattern and period.

The amplitudes of these variations are 3.3±0.2 mm for WILL-DRAO (370 km),

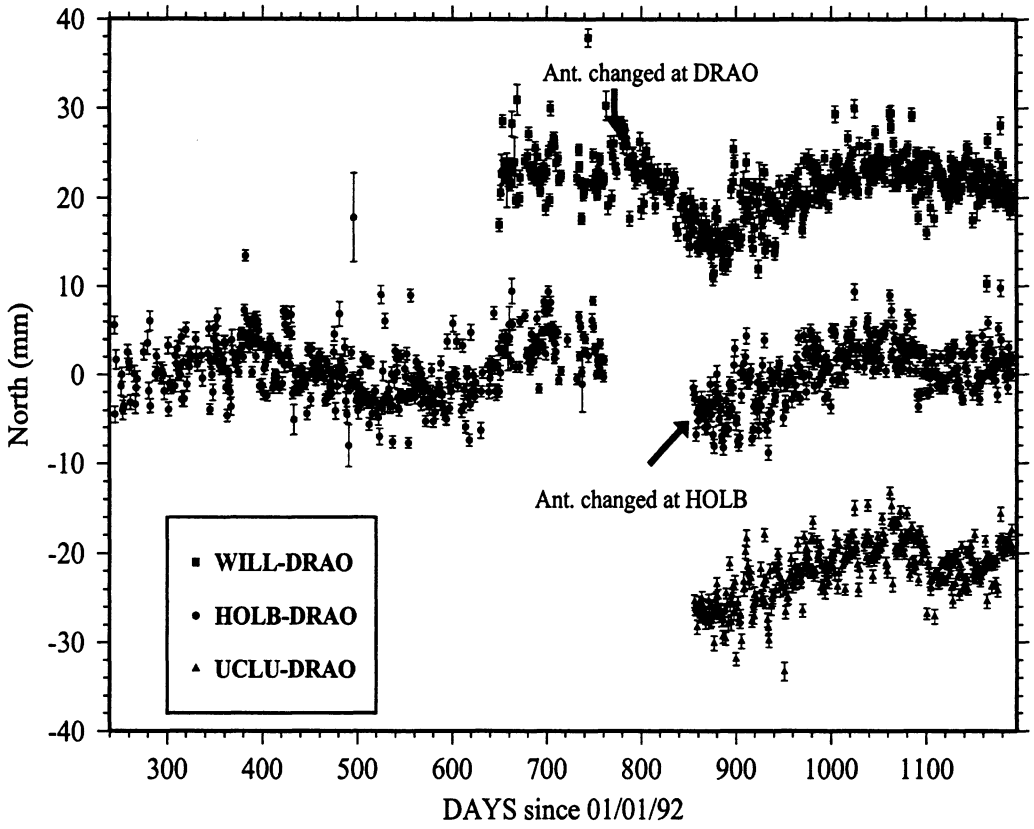

Figure 6.28: North components of the baselines WILL-DRAO, HOLB-DRAO, and UCLU-DRAO.

2.1±0.2 mm for UCLU-DRAO (434 km), and 2.5±0.1 mm for HOLB-DRAO (627 km) (Table 6.3). Thus, the amplitudes seem to have no evident bearing with the baseline length, but maybe with the baseline orientations, particularly the north component.

To investigate whether these variations also have satellite elevation-cutoff-angle-dependence, WILL-DRAO was tested with a 30-degree elevation cutoff angle. The solutions are shown in **Figure 6.29**. The spectral value for the time series with 30-degree cutoff is only reduced to 30% from 42% in Table 6.3, and the amplitude of a forced annual term to 2.9±0.2 mm from 3.4±0.2 mm. Therefore, these variations are not evidently elevation-cutoff-angle-dependent. Moreover, from Figure 6.28 the

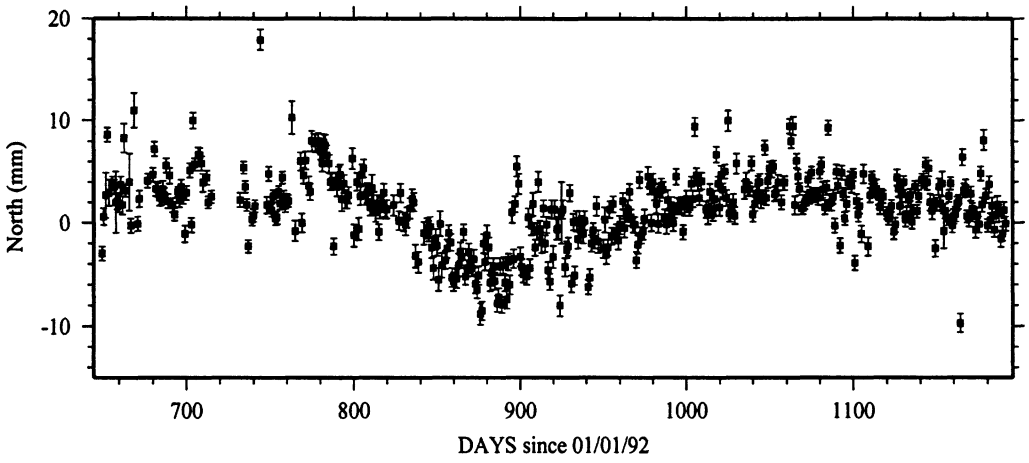

Figure 6.29: North component of the baseline WILL-DRAO with a 30-degree cutoff angle.

variations appear to be insensitive to antenna changes, including the change at the reference station DRAO. Consequently, these variations appear not to be related to errors such as the multipath/scattering effects and antenna phase center variations. In addition, the weak dependence of these variations on elevation cutoff angle may also imply that the atmospheric effects are also not responsible, especially considering that the east and the upward components of the three baselines, which are usually more sensitive to atmospheric errors, have not shown similar periodic constituents.

In summary of the above descriptions, the features of these variations in the north component can be listed as follows:

1. The amplitudes vary from 2.1 to 3.3 mm. There is a suggestion that these amplitudes are correlated with baseline orientation and not baseline length.

2. The variations on different baselines seem to have a similar phase pattern and the same annual period.

3. The variations are insensitive to changes in satellite elevation cutoff angle and antennas (at both the reference and non-reference stations).

4. Variations with these characteristics do not appear in the east or upward baseline components.

The implications of these features can be described as follows. Feature 1, the variation of amplitudes, and especially the apparent absence of the variation in the north component of baseline ALBH-DRAO, tend to rule out local deformations such as the tilting of the antenna pillar at the reference site DRAO as the source of this error. Feature 2 implies that a local, physical phenomenon at the non-reference stations are unlikely to be the cause of these variations. However, factors in regional scale, such as precipitation-incurred seasonal signals, cannot be ruled out. Feature 3 argues against seasonal multipathing variations being the cause while feature 4 suggests that tropospheric mismodelling and tidal mismodelling are unlikely causes since these would affect the upward and the east components more than the north components. In addition, from Figure 6.28, there is no evidence of decrease in magnitude after Febuary 1, 1994, when the DRAO coordinates was set to ITRF93 value at epoch 1995.0, which is accurate to about 2 cm as compared to up to 6 cm before the date. Therefore, error in DRAO coordinates is also unlikely to be the cause of the variations. This process of (not 100% certain) elimination leaves the precise orbit/EOP error and seasonal GPS monument motions as the likeliest candidates for the observed annual variations.

Still, to maintain a wide search range for the cause of the error and also due to lack of some crucial auxiliary data such as precipitation data for the region and GPS monument stability data, we chose to investigate some peripheral targets in this study, which include some "less likely" causes outlined above and possible existence of some small as yet undetected software bugs which may somehow only manifest themselves

over longer periods of solutions. This investigation, thus, may not pinpoint the exact cause of the error, but is intended to narrow down the searching range and help future studies. In summary, five main tests have been carried out, as described below.

Test 1 was a test of the polynomial representation of the precise orbits. The standard precise orbits are tabulated at 15-minute intervals, and normally in CGPS22, the precise orbits are represented by Chebyshev polynomials of order 15 for each satellite pass (roughly 6 hours). We chose to use two arbitrarily chosen days of JPL (Jet Propulsion Laboratory) precise orbits to do the test, since we managed to obtain both 15-minute and 5-minute tabulated precise orbits. By comparing the polynomial interpolation of the 15-minute sampled orbits with the 5-minute sampled orbits, the accuracy of the polynomial representation could be evaluated.

Test 2 involved toggling on/off some of the measurement correction models, specifically the solid Earth tide and the ocean loading plus pole tide. Since tidal effects are predominantly in the vertical component, this test is mainly for identifying software bugs related to these corrections, although it is also interesting to see the impact of these corrections on the solutions.

Test 3 estimated the x, y, z biases in the satellite local coordinate system. It was designed to test if there are any systematic errors with regard to the satellite orbits and the phase center calibration of the satellite transmitting antennas (offset of phase center from center of mass).

Test 4 was a test of the tropospheric propagation delay modelling in CGPS22, which uses Hopfield's model for zenith tropospheric delay, Black's mapping function, and a colored noise stochastic process for the local tropospheric scale factors. Obviously there are three areas to test: the model for the zenith tropospheric delay, the

mapping function, and the stochastic model. Firstly, Saastamoinen's model was used to replace Hopfield's model; secondly, the more up-to-date Herring and Niell mapping functions recommended by Mendes and Langley [1994] were adopted to replace Black's mapping function; and lastly, a random walk noise process and different parameterization schemes for the tropospheric delay were tested. The parameterization schemes included: estimating the residual combined wet and dry (non-hydrostatic and hydrostatic) zenith tropospheric delay (default in the routine WCDA data reduction), estimating the total combined wet and dry delay without any model corrections, and estimating a stochastic wet delay and a constant dry delay with model corrections.

Test 5 involved replacing the NRCan precise orbits with the IGS precise orbits. The IGS precise orbits are claimed to be comparable to, or better than, precise orbits generated by individual IGS analysis centres [Beutler et al., 1995]. Consequently, this test can identify possible biases in the NRCan orbits. However, since the IGS orbits and NRCan orbits are both inherently correlated with each other due to similar fundamental mathematical formulations for orbit modelling, existence of errors common to both orbits is possible and would not be detected in this test.

II. Results of the Tests

The tests described above were carried out using all of the WCDA data collected in 1994. The results are summarized briefly as follows:

Test 1: The comparison between the interpolated orbits using Chebyshev polynomials fit from the standard 15-minute tabulated precise orbits and the 5-minute tabulated precise orbits reveals that with a polynomial order equal to or higher than 15, the root mean square (rms) errors for all satellites are well below 1 cm. Reducing

the polynomial order below 14, results in larger errors (> 1 dm) for some satellites. It thus can be concluded that the polynomial order 15 used for routine WCDA data analyses is more than adequate and this interpolation of orbits procedure does not generate any significant error.

Test 2: A comparison was made among the routinely obtained solutions with regular tidal modelling (solid Earth tide, ocean loading, and pole tide), the solutions without ocean loading and pole tide corrections, and the solutions without any tidal (including solid Earth tide) corrections. The standard deviations for the solutions are listed in **Table 6.5**, as indicators for improvement or degradation of the solutions. The components that are subject to the offsets listed in Table 6.2, i.e., the east component of baseline ALBH-DRAO and the upward component of baseline WILL-DRAO, are omitted in Table 6.5 because they are not the components of our major interests here and the estimation of the offsets may deviate the calculated values of their standard deviations. It is found that the annual variations in the north components are almost completely unaffected by the addition or ommission of the tidal corrections. This is not surprising since tidal effects are confined to mostly the vertical component. However, as shown in Table 6.5, it is somewhat surprising that the solid Earth tide correction does not significantly improve the precision of the vertical component but appears to improve the precision of the horizontal components by 0.1 to 0.3 mm for almost all baselines. On the other hand, the ocean loading correction improves estimates of the vertical components but degrades slightly the estimates of the horizontal components.

Test 3: This test produced unexpected results. An examination of mean residuals for the satellite antenna offsets revealed zero offsets in the y and z axes, but an offset of 0.279 m in the x-axis. Further investigation revealed the software error which

Table 6.5: The standard deviations for solutions with different tidal models (mm).

Baseline	*Regular*			*No-loading*			*No-tides*		
	N	E	U	N	E	U	N	E	U
ALBH-DRAO	2.2	-	7.4	2.1	-	7.2	2.3	-	7.2
HOLB-DRAO	3.0	3.5	7.6	2.9	3.2	8.1	3.2	3.5	7.8
WILL-DRAO	2.9	3.2	-	2.9	3.2	-	3.0	3.1	-
UCLU-DRAO	2.1	2.8	6.6	2.1	2.8	7.2	2.2	3.1	6.7

caused this problem. After correction of this error, all the estimated residual x, y, z satellite antenna offsets became zero. **Table 6.6** lists the precisions of the original solutions and the precisions of the solutions recomputed with the corrected satellite antenna offset. These precisions are calculated as standard deviations about a best fitting line through the daily solutions. The precisions for the east (E) component of the ALBH-DRAO baseline and the upward (U) component of the WILL-DRAO baseline are not listed since they are contaminated by the large offsets and variations discussed in the last subsection. The most marked improvement occurs for the north component of the baselines HOLB-DRAO and WILL-DRAO (0.5 and 0.6 mm respectively), which are "coincidently" also the two most severely affected by the annual variations. Slightly suppressed as they are in the amplitudes, the annual variations remain in the recomputed solutions with the same features except for the somewhat smaller amplitudes. There is a striking similarity between the error caused by this x-axis satellite antenna offset and the annual variations in the north component of WCDA baselines, prompting additional analyses of these results which are discussed in part III of this subsection. It should also be noted that all other tests used the corrected version of the software.

Test 4: This test took the most intensive efforts. Four sub-tests were carried out,

Table 6.6: Precisions in the north, east, and upward components for the original solutions and the recomputed solutions with correct calibration of the x-axis satellite antenna offset. (in mm).

Baseline	*Original*			*Recomputed*		
	N	E	U	N	E	U
ALBH-DRAO	2.1	-	7.3	2.2	-	7.4
UCLU-DRAO	2.2	2.8	6.4	2.1	2.8	6.6
HOLB-DRAO	3.5	3.7	7.3	3.0	3.5	7.6
WILL-DRAO	3.5	3.2	-	2.9	3.2	-

and the results were then compared (in all three baseline components) to those using the original tropospheric estimation strategy (Hopfield's model, Black's mapping functions, and colored noise process with 10 hours correlation time and 5% steady state sigma). In the first sub-test, Herring's mapping functions were used to replace Black's mapping functions. The results indicated that both mapping functions gave almost identical solutions with few differences as large as 0.1 mm. The second sub-test estimated the total combined tropospheric wet and dry delays without any model corrections. This method is described and recommended by Tralli and Lichten [1990]. However, the results of this sub-test turned out to be comparable (within ± 0.1 mm) to those using the original estimation strategy. The third sub-test used Saastamoinen's tropospheric zenith delay model along with Niell's mapping functions and a random walk process for the residual combined wet and dry delay. Again, the results were not significantly different from the results with the original estimation strategy. The last sub-test estimated the wet delay and dry delay separately. The residual wet delay was estimated as a stochastic process, and the residual dry delay as a constant variable. The results of this last test showed comparable or slightly worse precisions than those original solutions. The conclusions that can be drawn from these tests are that the original tropospheric estimation strategy is totally satisfactory for the

routine reduction of WCDA data, and more importantly, the annual variation in the north component persists no matter what tropospheric estimation strategy is used.

Test 5: The precisions obtained using the IGS precise orbits are summarized in **Table 6.7**. Compared with the precisions of the recomputed solutions using the NRCan precise orbits in Table 6.6, it is evident that the solutions with IGS orbits generally show slightly better precisions. This verifies the better quality of the IGS

Table 6.7: Precisions in the north, east, and upward components for solutions using the IGS precise orbits. (in mm).

Baseline	*IGS*		
	N	E	U
ALBH-DRAO	2.1	-	7.4
UCLU-DRAO	2.1	2.8	6.5
HOLB-DRAO	2.8	3.5	8.0
WILL-DRAO	2.8	3.1	-

orbits. More important to this study, the annual variations in the north component remain the same with the IGS precise orbits. Therefore, the NRCan precise orbits are in good agreement with the IGS precise orbits and cannot be singled out as the cause of this annual variation. However, as stressed in part I of this subsection , errors common to both IGS and NRCan precise orbits may exist and cannot be detected by this test. Thus the precise orbits as a whole should not be dismissed from further investigations.

III. Analysis

Least Squares Spectral Analysis (LSSA) was carried out on the results from test 3. First the WCDA solutions were recomputed using the correction for the x-axis

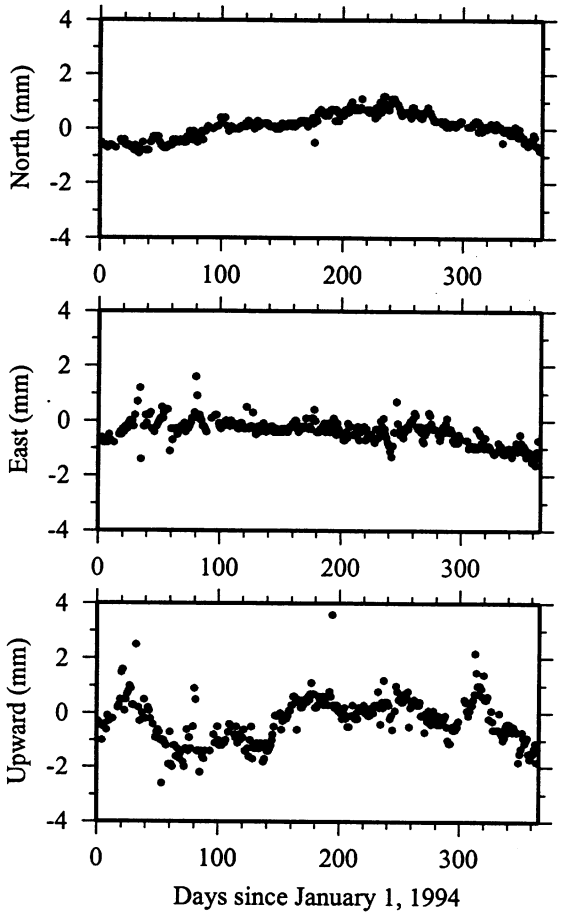

Figure 6.30: The errors induced by the uncalibrated x-axis satellite antenna offset for baseline ALBH-DRAO.

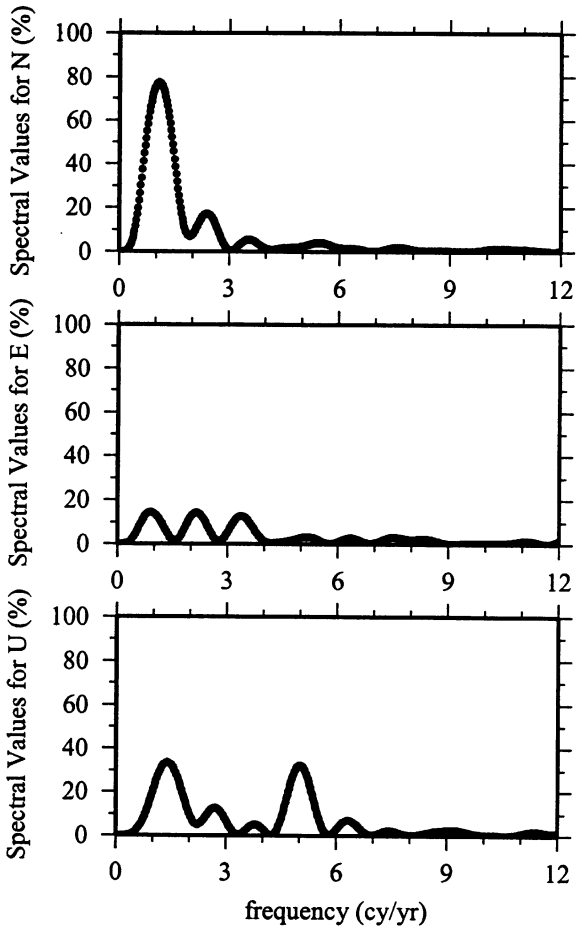

Figure 6.31: The LSSA spectra of the errors in Figure 6.30.

satellite antenna offset. Then the time series formed by differencing the recomputed solutions and the original solutions (without the correction for the x-axis satellite antenna offset) was obtained. This time series should represent the effect caused by the error in the satellite antenna offset. **Figures 6.30** and **6.31** show the differenced time series in north, east, and upward components for baseline ALBH-DRAO and their corresponding LSSA spectra. **Figures 6.32** and **6.33** show the same quantities for baseline WILL-DRAO. It is interesting to see that the north component is affected most strongly in a systematic way with a dominant annual frequency. This statement holds true for the other two baselines, although the magnitude of this error differs

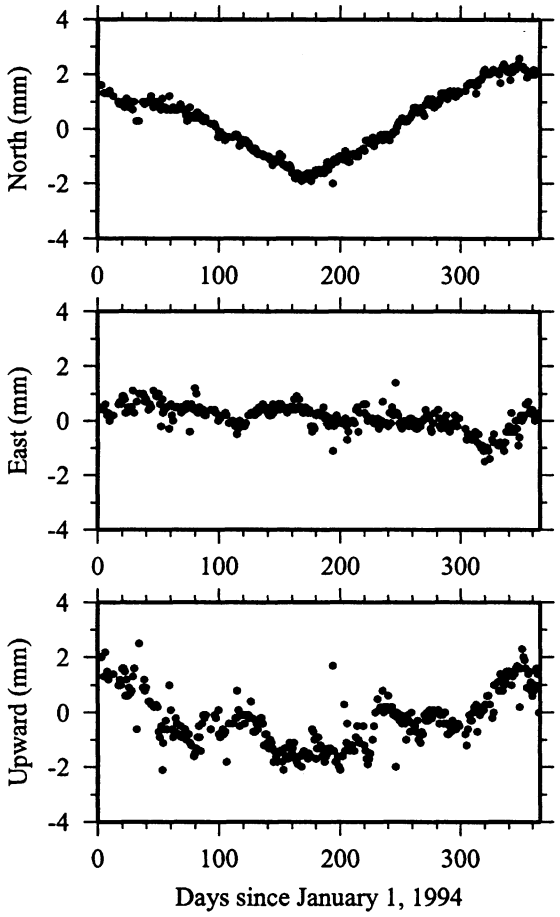

Figure 6.32: The errors induced by the uncalibrated x-axis satellite antenna offset for baseline WILL-DRAO.

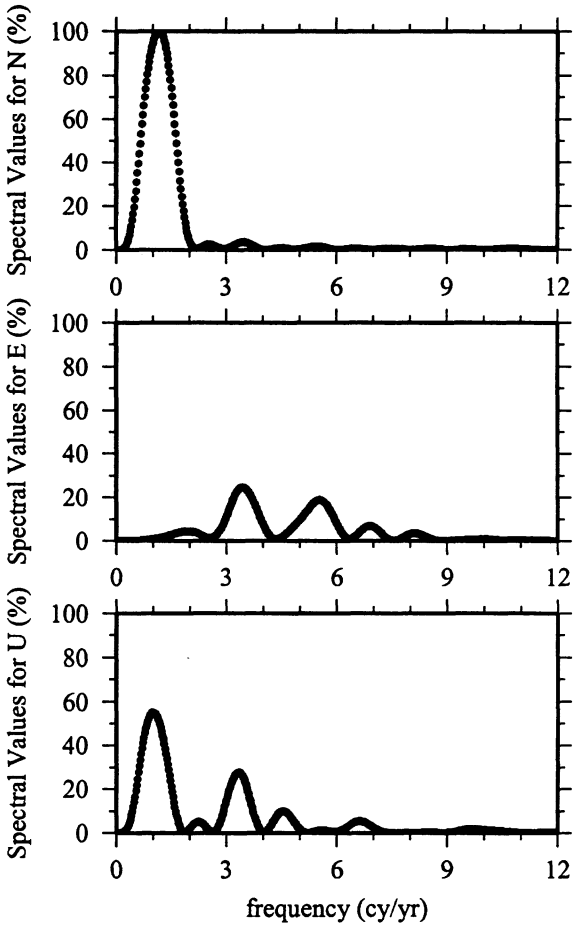

Figure 6.33: The LSSA spectra of the errors in Figure 6.32.

from baseline to baseline.

Figure 6.34 illustrates the north component of this error for all the WCDA baselines. Note that the baselines in Figure 6.34 are arranged in an order according to the orientation of the baselines (decreasing azimuth, see Figure 3.1). **Table 6.8** lists the amplitudes and phases of the dominant annual periodic constituents for the quantities shown in Figure 6.34, along with the corresponding formal errors. Evidently from Figure 6.34 and Table 6.8, the amplitude of this error is strongly dependent on the orientation of the baselines and not the baseline lengths, as one

Table 6.8: The estimated amplitudes and phases of the annual constituent present in the north component of the differenced time series for the WCDA baselines.

Baseline	Amplitude (mm)	Phase (deg)
ALBH-DRAO	0.59 ± 0.03	220.45 ± 2.17
UCLU-DRAO	0.96 ± 0.09	282.92 ± 5.99
HOLB-DRAO	1.38 ± 0.07	306.05 ± 3.37
WILL-DRAO	1.58 ± 0.02	353.17 ± 1.93

Table 6.9: The estimated amplitudes and phases of the annual constituent present in the north component of the recomputed WCDA solutions of the year 1994.

Baseline	Amplitude (mm)	Phase (deg)
ALBH-DRAO	0.89 ± 0.22	329.46 ± 15.07
UCLU-DRAO	1.50 ± 0.86	332.91 ± 18.09
HOLB-DRAO	2.63 ± 0.29	319.72 ± 18.26
WILL-DRAO	2.54 ± 0.28	319.18 ± 16.67

might typically expect for orbital errors! The phase of the error also appears to be increasing systematically as a function of baseline orientation.

To allow direct comparison to the error residuals of Figure 6.34, the daily variations in the north component apparent from the recomputed WCDA solutions have been plotted in the same order for the four baselines in Figure 6.35. **Table 6.9** lists the amplitudes and phases of the dominant annual periodic constituents for the quantities shown in Figure 6.35. (It should be noted that the estimates in Table 6.9 are subject to larger errors than those in Table 6.8). A comparison of the two tables and two figures shows a striking similarity between the two data sets, although Table 6.9 exhibits no clear trends in the phases of the annual variations. For example, in both Figures 6.34 and 6.35, all the baselines have a dominant annual period (even for ALBH-DRAO in Figure 6.35, although its LSSA spectral value is only about 6%),

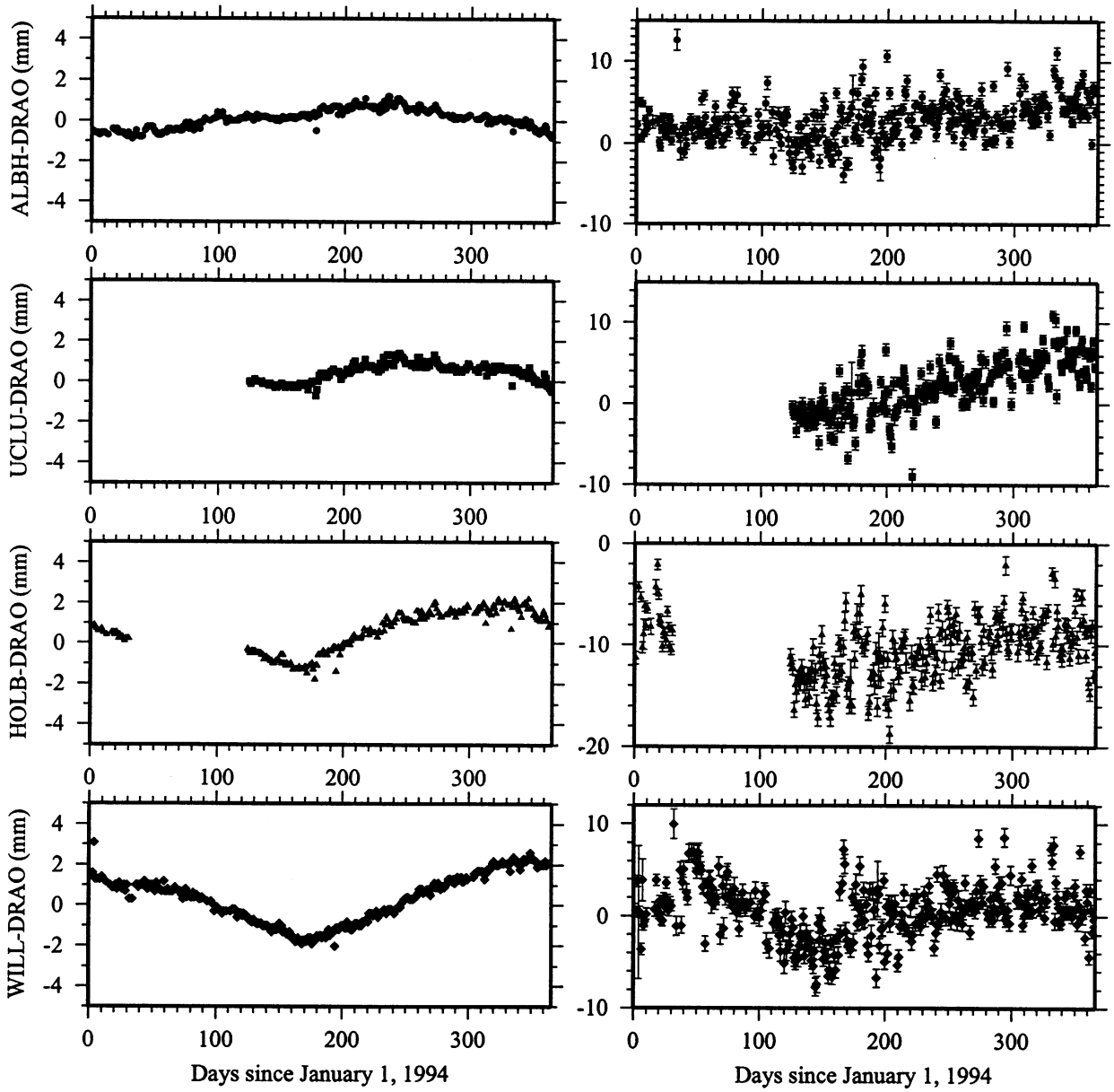

Figure 6.34: North component of the error time series caused by the incorrect x-axis satellite antenna offset in the WCDA solutions.

Figure 6.35: North component of the WCDA baselines after the correct calibration of the x-axis satellite antenna offset (plots are in the same order and with the same units as in Figure 6.34).

and the phases for WILL-DRAO and HOLB-DRAO are very close. Moreover, the two sets of amplitudes in Tables 6.8 and 6.9 are proportionally consistent even though the formal errors for the amplitudes in Table 6.9 are larger. For instance, taking the amplitude of ALBH-DRAO as 1 in both tables, the relative amplitudes in Table 6.8 would be 1.0, 1.6, 2.3, 2.7, and 1.0, 1.7, 3.0, 2.8 in Table 6.9. The amplitudes in Table 6.9 are larger than those in Table 6.8 by a factor of approximately 1.5. The large differences in the phases for ALBH-DRAO and UCLU-DRAO are possibly due to the comparatively smaller amplitudes for the two baselines and contamination by other errors.

It should be pointed out here that the above comparison does not prove that the annual variations in the north component of WCDA baselines are directly related to satellite antenna offsets. Rather, it shows that an orbital error, like the error in the x-axis satellite antenna offset described above, can result in an annual signal similar to the observed variations. Although the 27.9 cm x-axis satellite antenna offset is a systematic error for each individual satellite, the combined effect on the solutions is similar to a random orbital error. If it were a global systematic error for all the orbits, according to equation (5.1), about 5 cm would have the same effect as the 27.9 cm random error has made on the solutions (in Table 6.8). Therefore, a systematic error of about 7.5 cm in the precise orbit/EOP data can cause errors in the solutions of the same magnitude as in Table 6.9. Consequently, it is reasonable to conclude at this point that the precise orbit/EOP error is the primary suspect for the cause of the annual variations in the north component of the WCDA solutions, although GPS monument motions caused by seasonal precipitation cannot be completely ruled out as a possible source. Therefore, the exact cause awaits further data and further analyses.

IV. Summary

Five tests have been carried out in a search for the cause of the small annual variations present in the north component of the WCDA solutions producing some notable results. The errors related to the mismodelling of the tropospheric propagation delay are found to be unlikely causes of these variations. The quality of the polynomial represention of the precise orbits in the CGPS22 software and the quality of the IGS precise orbits are verified, although the improvement with IGS orbits over the NRCan orbits is marginal. Tests involving tidal effects confirm that no errors are introduced through ocean loading and pole tide corrections nor through solid Earth tide corrections. Most interestingly, it was found that an error in the calibration of the phase center offset of the satellite antennas along the satellite local x-axis led to error residuals with features similar to the observed annual variations in the north components. Consequently, systematic errors in the precise orbit/EOP data are strongly suspected as the cause of the annual variations, although the identification of the exact cause awaits further studies. Also other possibilities such as seasonal monument motions and errors in the software are not completely ruled out and further tests are required.

6.3 Precision Assessment

The precisions of the WCDA solutions are assessed using a short-term daily repeatability and a long-term daily repeatability. The short-term repeatability is calculated on a weekly basis (under the assumption of negligible true baseline change) as

$$\sigma_s^2 = \frac{n}{n-1} \sum_{i=1}^{n} \frac{(x_i - \bar{x})^2}{\sigma_i^2} / \sum_{i=1}^{n} \frac{1}{\sigma_i^2} \tag{6.1}$$

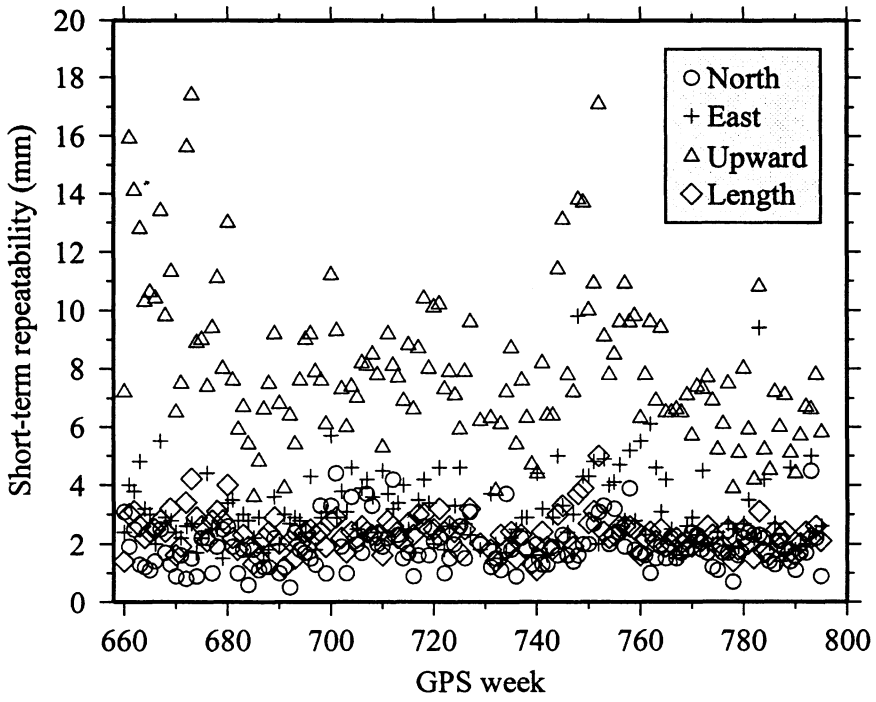

Figure 6.36: Short-term daily repeatability of baseline ALBH-DRAO.

where $\bar{x}$ is the weighted mean of the daily estimates x_i with a formal error σ_i over n days. The long-term daily repeatability is defined here as the overall standard deviation σ_l estimated with the LSSA residuals (Table 6.3), in which the linear trends and significant periodic constituents were removed.

Figures 6.36-6.39 show the short-term daily repeatabilities σ_s for the four WCDA baselines in terms of north, east, upward components and baseline length. The averaged short-term repeatabilities are given in **Table 6.10**, along with the baseline length dependent expression of the precisions which is defined according to Larson and Agnew [1991] by

$$\sigma(mm) = a(mm) + b(ppb) \cdot L(mm) \tag{6.2}$$

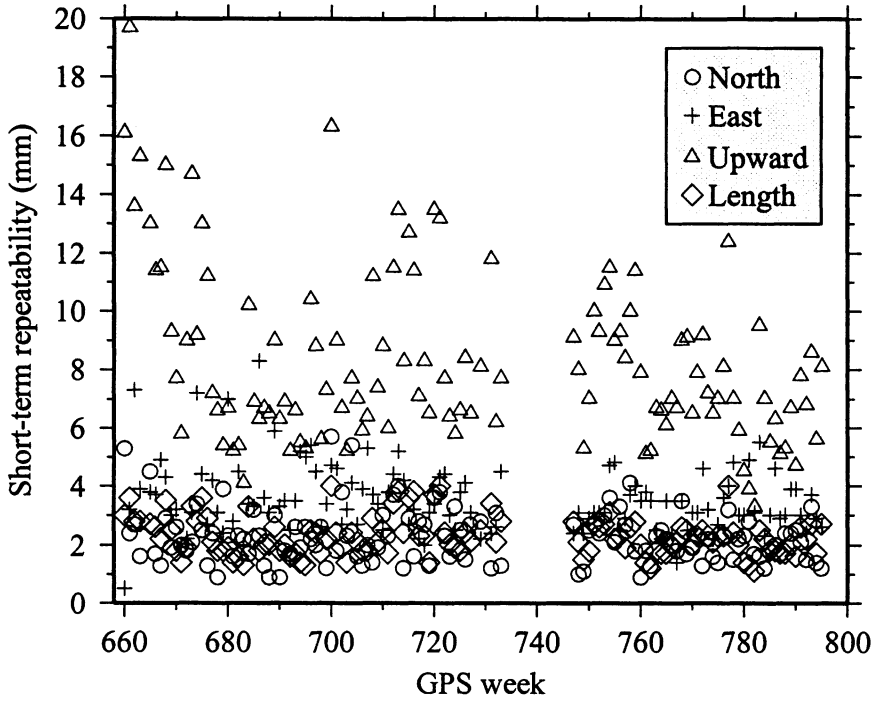

Figure 6.37: Short-term daily repeatability of baseline HOLB-DRAO.

where L is the baseline length in mm, b is the coefficient of the term dependent on the baseline length expressed in part per billion (ppb), and a is the independent term. As the range of baseline lengths for the WCDA is very limited, the length dependent expressions of the precisions are subject to large errors. A negative value of b is an indication of this inaccuracy.

The long-term daily repeatabilities σ_l calculated over entire solution sets with the LSSA algorithm are extracted from Table 6.3 and are summarized in **Table 6.11**. Compared with Table 6.10, it is evident that most of the long-term repeatabilities for the horizontal components and baseline lengths are larger than the short-term repeatabilities. This is because of the systematic errors unmodelled or mismodelled

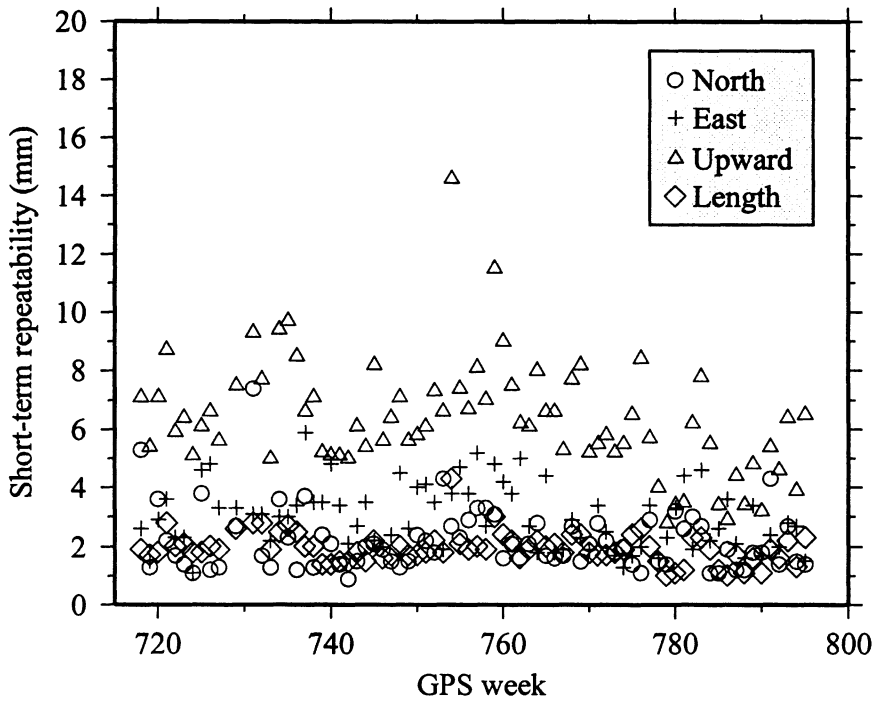

Figure 6.38: Short-term daily repeatability of baseline WILL-DRAO.

in the measurements which usually have a long-term behaviour such as the variations caused by scattering effects in the east component of baseline ALBH-DRAO.

Due to the predominantly north-south ground tracks of GPS satellites and the mainly east-west orientation of the WCDA baselines, the north component of each baseline has the best measurability and indeed it shows the best repeatabilities ranging from 2.3 to 2.9 mm for σ_l and 1.8 to 2.3 mm for σ_s.

The east component also shows very good repeatibilities, ranging from 3.0 to 4.5 mm for σ_l and 2.8 to 3.5 mm for σ_s, degraded by a factor of about 1.5 on average compared to the north component. Since the phase ambiguities are more correlated

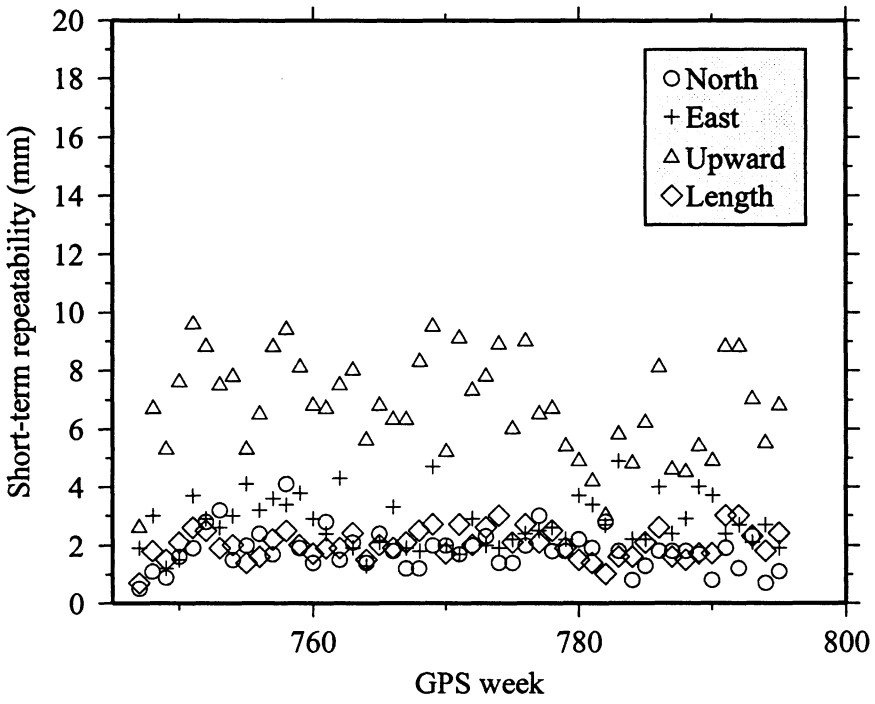

Figure 6.39: Short-term daily repeatability of baseline UCLU-DRAO.

with the east component than with the north, a small degradation like this is acceptable. It is worth mentioning that for a single-pass observation window (e.g., 4 - 6 hr), the factor of degradation is typically 2 to 5 due primarily to the shorter observation period so that the ambiguity resolution is very crucial for strengthening the east component of a baseline. In the WCDA solutions, though, the ambiguity resolution would not improve the east component significantly due to the already low degradation.

The upward component is the least constrained by GPS observations and is also the most sensitive to errors such as tropospheric delay. So it is normally the least precise among the three components. Nevertheless, a few millimetres repeatibility for

Table 6.10: Averaged short-term daily repeatabilities (mm).

Baselines	N	E	U	L
ALBH-DRAO	1.9	3.1	8.0	3.7
HOLB-DRAO	2.3	3.5	8.3	3.7
WILL-DRAO	2.2	3.0	6.3	3.9
UCLU-DRAO	1.8	2.8	6.8	4.0
a (mm)	1.6±0.4	2.5±0.6	6.1±2.0	3.9±0.3
b (ppb)	1.0±1.0	1.4±1.3	2.8±4.4	-0.2±0.7

Table 6.11: Averaged long-term daily repeatabilities (mm).

Baselines	N	E	U	L
ALBH-DRAO	2.5	4.0	8.4	3.8
HOLB-DRAO	2.9	4.5	8.7	4.4
WILL-DRAO	2.7	3.5	5.9	2.8
UCLU-DRAO	2.3	3.0	6.4	3.0
a (mm)	2.1±0.5	2.8±1.3	5.8±3.0	2.2±1.4
b (ppb)	1.1±1.0	2.2±2.9	3.6±6.6	3.0±3.1

this component has been achieved, as indicated in Tables 6.10 and 6.11 (5.9 to 8.3 mm). It should be noted that the long-term repeatabilities for the upward components are closely comparable with the short-term ones. This may be an indication of the success of the estimation strategy in the tropospheric modelling, since the upward component is the most affected component by the tropospheric delay.

In summary, 2 to 5 mm horizontal precision and 6 to 9 mm vertical precision in terms of long-term repeatability have been achieved in the WCDA data analysis. The short-term repeatabilities are slightly better than the long-term ones for horizontal components, which is a sign of the existence of long-term errors.

6.4 Crustal Deformation Signals Inferred from the WCDA Solutions

In order to eliminate biases in the linear rate estimates caused by the sinusoidal variations and offsets, linear rates have been estimated along with other parameters using the LSSA technique. The results are given in Table 6.3. For convenience, the estimated rates together with the formal errors in units of millimetres per year (mm/yr) are extracted from Table 6.3 and tabulated in **Table 6.12**.

Table 6.12: Estimated linear rates from LSSA (mm/yr).

Baseline	N	E	U	L
ALBH-DRAO	3.2±0.1	6.0±0.4	8.3±0.4	-6.4±0.4
HOLB-DRAO	0.0±0.1	-0.4±0.2	3.7±0.4	0.7±0.2
WILL-DRAO	-0.4±0.3	-2.2±0.4	11.5±1.3	1.6±0.3
UCLU-DRAO	7.2±0.9	5.7±0.6	-12.6±1.4	-6.9±0.6

As most of the linear rates in Table 6.12 are in good agreement ($<$ 1 mm/yr) with those directly calculated from a simple linear regression algorithm (with the offsets in Table 6.2 corrected), the **correlation coefficients**, R, are estimated for the linear rate estimates from such a linear regression. Correlation coefficients provide a measure of the significance of a linear trend estimate. The sign of R corresponds to the sign of slope of the linear trend. The closer to one the absolute value of R, the more significant the linear trend. The estimated R for each of the estimated linear rates are summarized in **Table 6.13**, along with $|r|$, the minimum $|R|$ that is required for a significant linear trend for a given degree of freedom and a 99% confidence level.

Table 6.13: Estimated correlation coefficients R.

Baseline	N	E	U	L	$\|r\|$
ALBH-DRAO	0.66	0.61	0.57	-0.65	0.13
HOLB-DRAO	0.03	-0.07	0.29	0.11	0.13
WILL-DRAO	-0.01	-0.23	0.59	0.20	0.13
UCLU-DRAO	0.55	0.45	-0.46	-0.52	0.15

Being more cautious because of the existence of long-term errors in the solutions, we arbitarily take $2|r|$ (instead of $|r|$) as the threshold value for significant R (implicitly for the estimated linear rates as well), it is found from Table 6.13 that the R for all components of baselines ALBH-DRAO and UCLU-DRAO, and U of baselines WILL-DRAO and HOLB-DRAO are above the threshold, thus the corresponding estimated linear trends are statistically significant.

Both ALBH-DRAO and UCLU-DRAO show significant northeastward displacement. The overall displacements for UCLU and ALBH are in the directions of N38°E ±7° and N62°E ±2° respectively, both of which are approximately orthogonal to the deformation front (displayed in Figure 3.1 as the plate boundary between the Juan de Fuca Plate and the North America Plate). This explains a larger northward displacement component for UCLU. The overall horizontal displacement rates for UCLU and ALBH are 9.2 mm/yr and 6.8 mm/yr respectively. The larger value for UCLU is possibly because of its shorter distance to the deformation front. These results are quite consistent with the results from previous geodetic measurements summarized in Chapter 2.

HOLB-DRAO has not shown any significant horizontal trends as the above two baselines on the southern part of Vancouver Island have. This is perhaps evidence of the different tectonic mechanism underlying the northern part of the island. Though,

caution must be taken because HOLB is the only station on the northern part and its representativeness is subject to tests when more stations are available in the area in the future.

WILL-DRAO has not shown any significant horizontal trends either, but this is exactly what one should expect since both WILL and DRAO are sitting on the North America Plate.

Although all the vertical trends for the WCDA baselines are significant based on the $2|r|$ criterion, compared with the horizontal estimates, these vertical trends must be treated with great caution. First is because the vertical component has the weakest geometric strength among the three components in GPS solutions (about three times lower as indicated by formal errors). Secondly is because it is apt to be contaminated by errors such as multipath/scattering effects, orbital errors, and tropospheric delay mismodelling. Having these in mind and looking at Figures 6.5, 6.10, 6.15, and 6.19, we can find that at least the vertical rates for WILL-DRAO and UCLU-DRAO need to be treated with caution. WILL-DRAO is known to have an offset in the vertical component caused by scattering effects (even at a 15-degree elevation cutoff angle). Also, the solutions for both baselines are relatively short (reflected by larger formal errors in Table 6.12), thus some long-term errors may not be averaged out yet. Nonetheless, ALBH-DRAO and HOLB-DRAO show interesting vertical trends, though these estimates may still be subject to significant long-term errors (e.g., in Figure 6.10, the solutions show non-linearity). Therefore, in general, the vertical trends are not sufficiently resolved with the solutions used herein. Future verification of these estimates are needed.

6.5 General Remarks

The results of 811 days of data reduction have been given and analyzed in this chapter. In general, the modelling and estimation strategy presented in Chapter 4 and Chapter 5 have turned out to be satisfactory in the processing of the WCDA data. The goal of the WCDA, i.e., monitoring crustal deformation at the few millimetre level, has been essentially achieved, especially in the horizontal plane. The horizontal precision is 2 to 5 mm and vertical precision 6 to 9 mm.

Some errors have been found in the solutions. These include elevation-cutoff-angle-dependent offsets and large annual variations (with an amplitude of about 7 mm) due to scattering effects, and small annual variations (with amplitudes of 2.1 to 3.3 mm) in the north component of most, if not all, of the WCDA baselines due possibly to errors in the precise orbit/EOP data. Discussions and analyses of these offsets and variations have been given and emphasized in this chapter.

The crustal deformation signals extracted from the solutions have shown consistency in the horizontal components with previous results from other types of measurements and the theoretical displacement model. However, it seems that the vertical trends have not been sufficiently resolved. Strictly speaking, these deformation signals are all subject to further verification because of the very limited number of baselines in the WCDA and the sophistication of the tectonic setting in the region.

Chapter 7

Conclusions and Recommendations

As stated in Chapter 1, the objective of the research reported in this thesis was to carry out high-precision continuous GPS monitoring of the crustal deformation in the northern Cascadia subduction zone and study some of the long-term GPS errors. Accordingly, an estimation strategy has been developed and the measurement models and algorithms in the CGPS22 software package used to process the GPS data have been refined and improved. From the results presented in Chapter 6, it can be concluded that the objective of this research has been achieved.

The following two sections of this chapter give the conclusions drawn from the research and recommendations for future studies.

7.1 Conclusions

It was shown in Chapter 6 that 2.3 to 4.5 mm horizontal precision and 5.9 to 8.7 mm vertical precision in terms of long-term repeatabilities have been routinely achieved in the WCDA data analysis. The short-term (weekly) repeatabilities are 1.8 to 3.5 mm in the horizontal components, better than the long-term ones by a factor of about 1.3, and 6.3 to 8.3 mm in the vertical components. The larger long-term repeatabilities of the horizontal components are due to the non-linear long-term systematic errors present in the WCDA solutions. The two types of repeatabilities for the vertical components are essentially at the same level, which may indicate that the stochastic modelling for the tropospheric parameters is successful.

Several errors were found in the WCDA solutions. First, scattering effects are confirmed as being present at stations DRAO, WILL, and ALBH. The source of the scattering effects is the antenna setup structure itself, which somehow induces signal scattering, diffraction, and even imaging, and thus causes a coupling between the overall antenna setup structure and the antenna phase pattern. Any antenna setup changes in the scattering environment could trigger significant offsets in the vertical component of baseline solutions. These offsets are shown to have a satellite elevation-cutoff-angle-dependence and can be as large as several centimetres.

Second, large offsets and a variation are found in the east component of the baseline ALBH-DRAO. The variation has about 7 mm amplitude and annual period, starting approximately in the fall of 1993. Different elevation cutoff angle tests have been carried out and both the variation and offsets have turned out to be largely dependent on the elevation cutoff angle. When a 30-degree elevation cutoff angle is chosen, the amplitude of the variation is significantly reduced to about 1.7 mm,

and the offsets reduced by 13% and 58% respectively. Considering that ALBH is severely affected by scattering effects, we can conclude that the variation and offsets are mainly due to the scattering at ALBH, though it is believed that there are some special multipath/scattering environmental settings involved such as signal blocking at low elevation angles caused by nearby trees.

Third, the north components of the baselines HOLB-DRAO, WILL-DRAO, and UCLU-DRAO have shown variations with 2.1 to 3.3 mm amplitudes, approximately annual period, and similar phase pattern. Before ALBH became affected by the large scattering effects, the north component of ALBH-DRAO has also shown a similar, but smaller and less significant variation [Chen, 1994]. From elevation cutoff angle tests, it was found that these variations have essentially no bearing with the elevation cutoff angles and they are insensitive to the antenna setup changes. Five additional tests were designed and carried out to identify the source of these variations. From the results, the quality of the orbital interpolation algorithm used in the CGPS22 software and the quality of the IGS precise orbits were verified, and tidal effects and tropospheric delays can probably be spared from the list of the possible error sources. In a test on offsets with regard to satellite orbits and the phase center calibration of the satellite transmitting antennas, it was found that the phase centre offset along the satellite local x-axis (0.279 m) was improperly accounted for in the software. This offset was shown to result in error residuals with features similar to the observed annual variations in the north components. The most interesting feature shared by the error residuals and the variations is their dependency on the baseline orientations rather than the baseline lengths. This gives rise to a strong suspicion that systematic errors of the level of about 7.5 cm in precise orbit/EOP data is the cause of these small annual variations. However, caution should be exercised here as other posibilities such as seasonal monument motions and software errors are not completely ruled out and

further studies are required to identify the exact cause of the variations.

Interesting crustal deformation signals have been resolved from the WCDA solutions. ALBH and UCLU, both located on the southern part of Vancouver Island and subject to deformation due to the convergence of the underlying Juan de Fuca Plate, have shown significant relative displacement with respect to the reference station at DRAO, which is far inland on the North America Plate. The maximum displacement rates are 6.8 mm/yr in direction N62°E±2° for ALBH and 9.2 mm/yr in direction N38°E±7° for UCLU. Both of the directions are approximately orthogonal to the deformation front. The larger displacement rate for UCLU is possibly because of its shorter distance to the deformation front. This result is in general consistent with, and far more precise than, the previous estimates from other types of data.

HOLB, located on the northern part of Vancouver Island and subject to the influence of the Explorer Plate, has not shown any significant relative trend as ALBH and UCLU do. This may be attributed to the different tectonic mechanism of the underlying Explorer plate.

WILL, as a check point located on the North America Plate, has not shown any significant relative horizontal trends with respect to DRAO. This effectively assures that the trends in the horizontal components of the whole network are not significantly biased by systematic errors.

The trends in vertical components, however, are subject to larger uncertainties compared to those in horizontal components. The elevation-cutoff-angle-dependent offsets caused by scattering effects in the vertical components and also possible existence of certain small yet significant long-term errors may largely contaminate the vertical trend estimates as the time spans of the solutions are not considerably long.

For these reasons, although both ALBH and HOLB have shown signs of uplifting at a few mm/yr level, all the vertical trend estimates must be treated with great caution.

7.2 Recommendations

Recommendations for future improvements based on this research are as follows:

- Although the linear rates estimated in Chapter 6 are good approximations to the velocity components, they do not take the covariance information associated with the daily solutions into account. Thus, the current analysis is not rigorous, and the most rigorous method would be to perform an adjustment using the covariance information to obtain the velocity estimates. In addition, as DRAO, ALBH, and HOLB are also ITRF stations, a transformation of the WCDA solutions into the ITRF frame is possible and could give more insight into the systematic errors in the WCDA solutions.

- The effect due to the error in the coordinates of the reference station DRAO needs to be studied. The error can be a few cm because the ITRF velocity was not taken into account in calculating the nominal ITRF coordinates. The WCDA solutions should better be updated with the DRAO coordinates held fixed to the ITRF coordinates of the date.

- The small annual variations in the north components need be further studied. Possible seasonal GPS monument motions should be investigated with the use of precipitation data or monument stability data. Also more examinations are required of the CGPS22 software to rule out any possible software errors in this regard.

- A further correlation and spectral analysis need be carried out to the solution time series. This can help to identify the GPS monument motion noise and give a more realistic evaluation on the uncertainty of the estimated linear rates.

- The scattering environments at DRAO, ALBH, and WILL need be examined closely and, if possible, remedied. Meanwhile, any antenna setup changes, if absolutely necessary, should be treated carefully as they may cause significant offsets in the solutions and contaminate the estimates of the displacement rates.

- The WCDA needs to be densified in order to get a better picture of the deformation in the whole region (three more stations have been added to the WCDA since the analysis reported in this thesis was carried out). The densification will also strengthen the capability to identify false signals and make a more comprehensive geodetic analysis possible.

- The automation level of the detection of cycle slips and outliers needs to be improved or a new algorithm to be developed to fully automate the daily data reduction. The current procedure still requires manual detection of cycle slips and outliers remain through the automatic detection, though visual detection has helped a great deal to ease the difficulty and the number of the remaining cycle slips is usually small.

- The P-code pseudoranges or pseudoranges obtained by cross-correlation need to be included and weighted properly in the least squares adjustment, in spite of their lower precision compared to the carrier phases. A correct inclusion of these pseudoranges should strengthen the solutions to certain degree and it also makes full use of the system.

- Although the carrier phase weighting scheme has been studied in this research and shown encouraging results as briefly discussed in Chapter 4, it has not been

applied to the routine data reduction. The weighting scheme, if selected properly, can partly account for the physical correlation among the measurements, and thus makes the solutions more robust. Further efforts are required to fully test the scheme.

- The spatial correlation of the tropospheric parameters needs to be further studied. At present, since the distances among the tracking sites are mostly greater than 300 km with two exceptions of 163 km between ALBH and UCLU and 267 km between HOLB and UCLU, this correlation should be wellnigh negligible if the assumptions made in section 4.3.8 are correct. However, as the WCDA is densified, the distances among stations will decrease and this correlation may have some noticeable influences on the solutions then.

- A program with the ability to quickly check on the quality of the carrier phases and give an early alarm if things go wrong needs to be developed. This will avoid the recurrence of the unnoticed receiver malfunctioning at HOLB for 3 months in 1994, during which the pseudoranges were normal as usual but the carrier phases were later found totally unusable.

References

Baker, T. F., D. J. Curtis and A. H. Dodson (1995). "Ocean tide loading and GPS." *GPS World*, March, pp. 54-59.

Bassiri, S. and G. A. Hajj (1993). "Higher-order ionospheric effects on the Global Positioning System observables and means of modeling them." *Manuscripta Geodaetica*, Vol. 18, pp. 280-289.

Beutler, G., J. Kouba and T. Springer (1995). "Combining the orbits of the IGS analysis centers." *Bulletin Géodésique*, No. 69, pp. 200-222.

Black, H. D. (1978). "An easily implemented algorithm for the tropospheric range correction." *Journal of Geophysical Research*, Vol. 83, No. B4, pp. 1825-1828.

Blewitt, G. (1992). "Mixing data types from Rogue/Turbo Rogue in code/codeless modes." Jet Propulsion Laboratory Interoffice Memorandum, November 16.

Blewitt, G. (1993). "Advances in Global Positioning System technology for geodynamics investigations: 1978-1992." Contributions of Space Geodesy to Geodynamics, D. E. Smith and D. L. Turcotte, eds., AGU Geodynamics Series, Vol. 25, pp. 195-213, 1993.

Blewitt, G., M. B. Heflin, K. J. Hurst, D. C. Jefferson, F. H. Webb and J. F. Zumberge (1993). "Absolute far-field displacements from the 28 June 1992 Landers earthquake sequence." *Nature*, 361, pp. 340-342.

Bock, Y. (1991). "Continuous monitoring of crustal deformation." *GPS World*, June, pp. 40-47.

Bock, Y., D. C. Agnew, P. Fang, J. F. Genrich, B. H. Hager, T. A. Herring, K. Hudnut, R.W. King, S. Larsen, J.-B. Minster, K. Stark, S. Wdowinski and F. K. Wyatt (1993). "Detection of crustal deformation from the Landers earthquake sequence using continuous geodetic measurements." *Nature*, 361, pp. 337-340.

Chen, D. and R. B. Langley (1990). "A geometrical analysis of the effect of satellite orbit error on GPS relative positioning." *Proceedings of the Second International*

Symposium on Precise Positioning with the Global Positioning System, GPS'90, Ottawa, Canada, September 3-7, pp. 757-771.

Chen, X. and H. Dragert (1992) "Turbo Rogue data tests report." Unpublished document, Pacific Geoscience Centre, Sidney, B.C., January.

Chen, X. (1994). "Analyses of continuous GPS data from the Western Canada Deformation Array." *Proceedings of ION GPS-94*, Salt Lake City, Utah, Sept. 20-23, pp. 1339-1348.

Chen, X., R. B. Langley and H. Dragert (1995). "The Western Canada Deformation Array: an update on GPS solutions and error analysis." *Proceedings of IAG Symposium G1, "GPS Trends in Precise Terrestrial, Airborne, and Spaceborne Applications"*, XXI General Assembly of the International Union of Geodesy and Geophysics, Boulder, CO, July 2-14, pp. 70-74.

Chen, X., R. B. Langley and H. Dragert (1996). "Investigation of annual variations in the WCDA GPS solutions." *Proceedings of ION GPS-96*, Kansas City, Missouri, Sept. 17-20, pp. 1809-1818.

Darby, D. J. and C M. Meertens (1995). "Terrestrial and GPS measurements of deformation across the Taupo Back Arc and Hikurangi Forearc regions in New Zealand." *Journal of Geophysical Research*, Vol. 100, No. B5, pp. 8221-8232.

Delikaraglou, D. (1989). "On principles, methods and recent advances in studies towards a GPS-based control system for Geodesy and Geodynamics." NASA Technical Memorandum 100716, NASA/Goddard Space Flight Center, Greenbelt, Maryland, Feburary.

Dixon, T. H. and S. K. Wolf (1990). "Some tests of wet tropospheric calibration for the CASA UNO Global Positioning System experiment." *Geophysical Research Letters*, Vol. 17, No. 3, pp. 203-206.

Dragert, H. (1987). "The fall (and rise) of central Vancouver Island: 1930-1985." *Canadian Journal of Earth Science*, Vol. 24, pp. 689-697.

Dragert, H. and M. Lisowski (1990). "Crustal deformation measurements on Vancouver Island, British Columbia: 1976 to 1988." *Global and Regional Geodynamics*, Springer-Verlag New York, pp. 241-249.

Dragert, H., R. D. Hyndman, G. C. Rogers and K. Wang (1994a). "Current deformation and the width of the seismogenic zone of the northern Cascadia subduction thrust." *Journal of Geophysical Research*, Vol. 99, No. B1, pp. 653-668.

Dragert, H., M. Schmidt and X. Chen (1994b). "The use of continuous GPS tracking for deformation studies in southwestern British Columbia." *Proceedings of ION GPS-94*, Salt Lake City, Utah, September 20-23, pp. 97-103.

Dragert, H., X. Chen, and J. Kouba, "GPS Monitoring of Crustal Strain in Southwest British Columbia with the Western Canada Deformation Array." Geomatica, Vol. 49, No.3, pp. 301-313, 1995.

Dragert, H. and R. D. Hyndman (1995). "Continuous GPS monitoring of elastic strain in the northern Cascadia subduction zone." *Geophysical Research Letters*, Vol. 22, pp. 755-758.

Elósegui, P., J. L. Davis, R. T. K. Jaldehag, J. M. Johansson, A. E. Niell and I. I. Shapiro (1995). "Geodesy using the Global Positioning System: the effects of signal scattering on estimates of site position." *Journal of Geophysical Research*, Vol. 100, No. B1, pp. 9921-9934.

Euler, H. and C. C. Goad (1991). "On optimal filtering of GPS dual frequency observations without orbit information." *Bulletin Géodésique*, Vol. 65, No. 2, pp. 130-143.

"Federal Radionavigation Plan." Prepared jointly by Department of Defense and Department of Transportation, 1994.

Georgiadou, Y. and A. Kleusberg (1988). "On carrier signal multipath effects in relative GPS positioning." *Manuscripta Geodaetica*, Vol. 13, pp. 172-179.

Grant, D. B. (1990). "Combination of terrestrial and GPS data for earth deformation studies." *UNISURV Report*, S-32, The University of New South Wales, Australia.

Herring, T. A. (1992). "Modeling atmospheric delays in the analysis of space geodetic data." Publications on Geodesy, Vol. 36, *Proceedings of Refraction of Transatmospheric Signals in Geodesy*, edited by J. C. DeMunck and T. A. Th. Spoelstra, Netherlands Geodetic Commission Publications in Geodesy, The Hague, Netherlands, pp. 157-164.

Hopfield, H. S. (1969). "Two-quartic tropospheric refractivity profile for correcting satellite data." *Journal of Geophysical Research*, Vol. 74, No. 18, pp. 4487-4499.

Hopfield, H. S. (1971). "Tropospheric effect on electromagnetically measured range: prediction from surface weather data." *Radio Science*, Vol. 6, No. 3, pp. 357-367.

Hudnut, K. W., Z. Shen, M. Murray, S. McClusky, R. King, T. Herring, B. Hager, Y. Feng, P. Fang, A. Donnellan and Y. Bock (1996). "Co-seismic displacements of the 1994 Northridge, California, earthquake." *Bulletin of the Seismological Society of America*, Vol. 86, No. 1B, pp. S19-S36.

Hyndman, R. D. and K. Wang (1993). "Thermal constrains on the zone of major thrust earthquake failure: the Cascadia subduction zone." *Journal of Geophysical Research*, Vol. 98, No. B2, pp. 2039-2060.

James, T. S. and W. J. Morgan (1990). "Horizontal motions due to post-glacial rebound." *Geophysical Research Letters*, Vol. 17, No. 7, pp. 957-960.

Kaniuth, K., H. Tremel and M. Suarez (1989). "On the estimability of residual tropospheric path delays in the GPS network adjustment." *GPS for Geodesy and Geodynamics*, Walferdange, Luxemberg, November 20-22, pp. 49-59.

King, N. E., J. L. Svarc, E. B. Fogelman, W. K. Gross, K. W. Clark, G. D. Hamilton, C. H. Stiffler and J. M. Sutton (1995). "Continuous GPS observations across the Hayward Fault, California, 1991-1994." *Journal of Geophysical Research*, Vol. 100, pp. 20,271-20,283.

Kleusberg, A., Y. Georgiadou and H. Dragert (1988). "Establishment of crustal deformation networks using GPS: a case study." *CISM Journal ACSGC*, Vol. 42, No. 4, pp. 341-351.

Kouba, J., A. Lambert, J. Popelar, R.R. Steeves and W.C. Cannon (1986). "Plans for VLBI and GPS monitoring network for Geodesy and Geodynamics in Canada." *Advances in Space Research*, Vol. 6, No. 9, pp. 75-78.

Kouba, J. and J. Popelar (1990). "GPS satellite monitoring and data analysis." *Proceedings of the 2nd International Symposium on Precise Positioning with GPS*, Ottawa, Canada, September 3-7, pp. 656-662.

Kouba, J., J. Popelar and D. Delikaraglou (1991). "GPS orbit monitoring and data analysis in Canada." *Advances in Space Research*, Vol. 11, No. 6, pp. 193-196.

Kouba, J. and X. Chen (1992). "Near real time GPS data analysis and quality control." *Proceedings of the 6th International Geodetic Symposium on Satellite Positioning*, Columbus, Ohio, March, 17-20, Vol. II, pp. 628-637.

Kouba, J., R. Tetreault, R. Ferland and F. Lahaye (1993). "IGS data processing at the EMR Master Active Control System Centre." *Proceedings of the 1993 IGS Workshop*, University of Bern, Bern, Switzerland, March 25-26, pp. 123-132.

Lahaye, F., M. Caissy, P. Heroux, K. MacLeod and J. Popelar (1997). "Canadian Active Control System real-time GPS correction service performance review." Presented at the 1997 National Technical Meeting of the Institute of Navigation, Santa Monica, CA., January 14-16.

Lambeck, K. (1988). "Geophysical Geodesy - the Slow Deformations of the Earth." Oxford Science Publications, New York.

Langbein, J., F. Wyatt, H. Johnson, D. Hamann and P. Zimmer (1995). "Improved stability of a deeply anchored geodetic monument for deformation monitoring." *Geophysical Research Letters*, Vol. 22, No. 24, pp. 3533-3536.

Langbein, J. and H. Johnson (1997). "Correlated errors in geodetic time series: implications for time-dependent deformation." *Journal of Geophysical Research*, Vol. 102, No. B1, pp. 591-603.

Larson, K. M. and D. C. Agnew (1991). "Application of the Global Positioning System to crustal deformation measurement: 1. precision and accuracy." *Journal of Geophysics Research*, Vol. 96, No. B10, pp. 16,547 - 16,565.

Larson, K. M., F. H. Webb and D. C. Agnew (1991). "Application of the Global Positioning System to crustal deformation measurement: 2. the influence of errors in orbit determination networks." *Journal of Geophysics Research*, Vol. 96, No. B10, pp. 16,567 - 16,584.

Leick, A. (1995). "GPS Satellite Surveying (second edition)." John Wiley & Sons, Inc., New York.

Levy, L. J. (1997). "The Kalman filter: navigation's integration workhorse." *GPS World*, September, pp. 65-71.

Lichten, S. M., and J. S. Border (1987). "Strategies for high-precision Global Positioning System orbit determination." *Journal of Geophysical Research*, Vol. 92, No. B12, pp. 12751-12762.

Lieske, J. H., T. Lederle, W. Fricke and B. Morando (1977). "Expressions for the precession quantities based upon the IAU (1976) system of Astronomical constants." *Astro. Astrophys.*, Vol. 58, pp. 1-16.

Lisowski, M., S. Owen and P. Segall (1996). "The Kilauea volcano, Hawaii, continuous GPS network: recent results." *EOS Trans. AGU*, Vol. 77, Fall Meeting Suppl., F808.

Lindqwister, U. J., J. F. Zumberge, F. H. Webb and G. Blewitt (1991). "Few millimeter precision for baselines in the California Permanent GPS Geodetic Array." *Geophysical Research Letters*, Vol. 18, No. 6, pp. 1135-1138.

Mandelbrot, B. B. (1982). "The Fractal Geometry of Nature." W. H. Freeman and Co., San Francisco, CA.

Mendes, V. B. and R. Langley (1994). "A comprehensive analysis of mapping functions used in modeling tropospheric propagation delay in space Geodetic data." *Proceedings of KIS94*, International Symposium on Kinematic Systems in Geodesy, Geomatics and Navigation, Banff, Canada, August 30 - September 2, pp. 87-89.

Miyazaki, S., H. Tsuji, Y. Hatanaka, Y. Abe, A. Yoshimura, K. Kamada, K. Kobayashi, H. Morishita and Y. Iimura (1996). "Establishment of the nationwide GPS array (GRAPES) and its initial results on the crustal deformation of Japan." *Bulletin of Geographic Surveying Institute*, Japan, Vol. 42, pp. 27-41.

Niell, A. E. (1996). "Global mapping functions for the atmosphere delay at radio wavelengths." *Journal of Geophysical Research*, Vol. 101, pp. 3227-3246.

Pagiatakis, S. D. (1982). "Ocean tide loading, body tide and polar motion effects on Very Long Baseline Interferometry." Technical Report No. 92, Department of Surveying Engineering, University of New Brunswick, Fredericton, N.B., Canada.

Rogers, G. C. (1988). "An assessment of the megathrust earthquake potential of the Cascadia subduction zone." *Canadian Journal of Earth Science*, Vol. 25, pp. 844-852.

Saastamoinen, J. (1973). "Contributions to the theory of atmospheric refraction." (in three parts), *Bulletin Géodésique*, No. 105, pp. 279-298; No. 106, pp. 383-397; No. 107, pp. 13-34.

Savage, J. C., M. Lisowski, and J. L. Svarc (1994). "Postseismic deformation following the 1989 (M = 7.1) Loma Prieta, California, earthquake." *Journal of Geophysical Research*, Vol. 99, No. B7, pp. 13757-13765.

Seeber, G. (1993). "Satellite Geodesy - Foundations, Methods, and Applications." Walter de Gruyter, New York.

Shen, Z., D. D. Jackson, Y. Feng, M. Cline, M. Kim, P. Fang and Y. Bock (1994). "Postseismic deformation following the 1992 Landers earthquake." *Seismological Society of America Bulletin*, Vol. 84, pp. 780-791.

Sovers, O. J. and J. S. Border (1987). "Observation model and parameter partials for the JPL geodetic GPS modelling software "GPSOMC"." *JPL Publication* 87-21, Jet Propulsion Laboratory, Pasadena, California.

Tatarskii, V. I. (1961). "Wave Propagation in a Turbulent Medium." Dover, New York.

Thompson, A. R., J. M. Moran and G. W. Swenson Jr. (1986). "Interferometry and Synthesis in Radio Astronomy." John Wiley & Sons, Inc., New York.

Tralli, D. M. and S. M. Lichten (1990). "Stochastic estimation of tropospheric path delays in Global Positioning System geodetic measurements." *Bulletin Géodésique*, No. 64, pp. 127-159.

Treuhaft, R. N. and G. E. Lanyi (1987). "The effect of the dynamic wet troposphere on radio interferometric measurements." *Radio Science*, Vol. 22, No. 2, pp. 251-265.

Tushingham, A. M. (1991). "Potential effects of ongoing postglacial adjustment on Very Long Baseline Interferometry measurements." *Geophysical Research Letters*, Vol. 18, No. 7, pp. 1281-1284.

Vaníček, P. and E. Krakiwsky (1982). "Geodesy: The Concepts (second edition)." Elsevier Science Publishers B. V., Amsterdam, The Netherland.

Wang, K., H. Dragert and H. J. Melosh (1994). "Finite element study of uplift and strain across Vancouver Island." *Canadian Journal of Earth Science*, Vol. 31, pp. 1510-1522.

Wei, Z. (1986). "Positioning with NAVSTAR, the Global Positioning System." Report No. 370, Department of Geodetic Science and Surveying, The Ohio State University, Columbus, Ohio.

Wells, D. E., P. Vaníček and S. Pagiatakis (1985). "Least squares spectral analysis revisited." Technical Report No. 84, Dept. of Geodesy and Geomatics Engineering, University of New Brunswick, Fredericton, N.B., Canada.

Wells, D. E., N. Beck, D. Delikaraglou, A. Kleusberg, E. J. Krakiwsky, G. Lachapelle, R. B. Langley, M. Nakiboglu, K. Schwarz, J. M. Tranquilla and P. Vaníček (1986). "Guide to GPS Positioning." Canadian GPS Associates, Fredericton, New Brunswick, Canada.

Wu, J. T., S. C. Wu, G. A. Hajj, W. I. Bertiger and S. M. Lichten (1993). "Effects of antenna orientation on GPS carrier phase." *Manuscripta Geodaetica*, Vol. 18, pp. 91-98.

Yaglom, A. M. (1987). "Correlation Theory of Stationary and Related Random Functions - Volume I: Basic Results." Springer-Verlag New York Inc., New York.

Young, L. (1995). Personal Communication with Dr. H. Dragert.

Yunck, T. P. (1993). "Coping with the atmosphere and ionosphere in precise satellite and ground positioning." *Geophysical Monograph* 73, IUGG Volume 13, pp. 1-16.

Zielinski, J. B. (1989). "GPS baseline error caused by the orbit uncertainty." *Manuscripta Geodaetica*, Vol. 14, pp. 117-124.

VITA

Full Name: Xin Chen

Place and Date of Birth: Beijing, P. R. China
May 22, 1964

Permanent Address: 200 de Gaspé, Apt. 807,
Verdun, Quebec, Canada H3E 1E6

Schools Attended: Beijing 93rd High-school, Haidian District,
Beijing, P. R. China

Universities Attended: B.Sc., 1984
Department of Geodesy
Wuhan Technical University of Surveying and Mapping
Wuhan, Hubei Province, P. R. China

Publications:

Chen, X. (1987). "Evaluation of various methods for GPS satellite selection." *Scientific and Technological Developments in Surveying and Mapping* (in Chinese), January, pp. 12-17.

Chen, X. (1988). "GPS satellite visibility computation in space." *Scientific and Technological Developments in Surveying and Mapping* (in Chinese), March, pp. 14-20.

Kouba, J. and X. Chen (1992). "Near real time GPS data analysis and quality control." *Proceedings of the 6th International Geodetic Symposium on Satellite Positioning*, Columbus, Ohio, March 17-20, Vol. II, pp. 628-637.

Chen, X. (1994). "Analyses of continuous GPS data from the Western Canada Deformation Array." *Proceedings of ION GPS-94*, Salt Lake City, Utah, September 20-23, Vol. II, pp. 1339-1348.

Dragert, H., M. Schmidt and X. Chen (1994). "The use of continuous GPS tracking for deformation studies in southwestern British Columbia." *Proceedings of ION GPS-94*, Salt Lake City, Utah, September 20-23, Vol. I, pp. 97-103.

Dragert, H., X. Chen and J. Kouba (1995). "GPS monitoring of crustal strain in southwestern British Columbia with the Western Canada Deformation Array." *Geomatica*, Vol. 49, No.3, pp. 301-313.

Chen, X., R. B. Langley and H. Dragert (1995). "The Western Canada Deformation Array: an update on GPS solutions and error analysis." *Proceedings of IAG Symposium G1: GPS Trends in Precise Terrestrial, Airborne, and Spaceborne Applications*, XXI General Assembly of the International Union of Geodesy and Geophysics (IUGG), Boulder, Colorado, July 2-14, pp. 70-74.

Chen, X., R. B. Langley and H. Dragert (1996). "Investigation of annual variations in the WCDA GPS solutions." *Proceedings of ION GPS-96*, Kansas City, Missouri, September 17-20, Vol. II, pp. 1809-1818.

Chen, X., R. Bindschadler and P. Vornberger (1996). "Preliminary determination of ice flow velocity in the west Antarctica using high precision GPS measurements." *Proceedings of ION GPS-96*, Kansas City, Missouri, September 17-20, Vol. II, pp. 1853-1861.

Chen, X., R. Bindschadler and P. Vornberger (1997). "Determination of velocity field and strain-rate field in the west Antarctica using high precision GPS measurements." Submitted to *Surveying and Land Information Systems*, American Congress on Surveying and Mapping (ACSM), September.